Experimental study and numerical modelling of squeeze flow in laminate viscous discontinuous composites

Grégoire Sorba

UNIVERSITE BRETAGNE LOIRE

CENTRALE NANTES

Thèse de Doctorat

Grégoire SORBA

Mémoire présenté en vue de l'obtention
du grade de Docteur de l'Ecole Centrale de Nantes
Sous le label de l'UNIVERSITÉ BRETAGNE LOIRE

École doctorale : Sciences pour l'Ingénieur (SPI)

Discipline : **Mécanique des solides, des matériaux, des structures et des surfaces**
Unité de recherche : **UMR 6183 – Institut de recherche et génie civil et mécanique**

Soutenue le 4 décembre 2017

Etude expérimentale et modélisation numérique des écoulements de compression dans les composites stratifiés visqueux à plis discontinus

JURY

Président du jury :	**ALLIX Olivier**, Professeur des Universités, ENS Paris-Saclay
Rapporteurs :	**ADVANI Suresh,** Professeur, Université de Delaware, États-Unis **VIDAL-SALLE Emmanuelle,** Professeur des Universités, INSA de Lyon
Examinateurs :	**HALLETT Stephen**, Professeur, Université de Bristol, Royaume-Uni **LAMERS Edwin**, Docteur, Reden, Pays-Bas
Directeur de thèse :	**BINETRUY Christophe,** Professeur des Universités, Ecole Centrale de Nantes
Co-directeur de thèse :	**COMAS-CARDONA Sébastien,** Professeur des Universités, Ecole Centrale de Nantes
Co-encadrant de thèse :	**LEYGUE Adrien**, Chargé de Recherche CNRS, Ecole Centrale de Nantes

UNIVERSITE BRETAGNE LOIRE

CENTRALE NANTES

Thèse de Doctorat

Grégoire SORBA

Etude expérimentale et modélisation numérique des écoulements de compression dans les composites stratifiés visqueux à plis discontinus

Experimental study and numerical modelling of squeeze flow in laminate viscous discontinuous composites

Résumé

La liberté de conception des composites peut être améliorée par la combinaison de préimprégnés continus et discontinus. Le formage d'un empilement préchauffé constitué de plis discontinus distribués et orientés de manière optimale peut mener à des défauts inacceptables tels que des plissements dans le plan et hors-plan, glissement de plis, rotation de plis adjacents, flexion de fibres induite par un écoulement de compression transverse et finalement une distribution des fibres inappropriée et inefficace. Ces phénomènes naissent de la liberté individuelle de déplacement et de déformation des plis discontinus à l'intérieur du moule pendant la phase de formage. Premièrement ce travail présente des expériences conduites afin d'identifier le comportement sous compression d'un empilement de préimprégnés visqueux discontinus unidirectionnels et tissés. Un modèle basé sur une approche fluide hétérogène visqueux isotrope transverse est ensuite développé en accord avec les observations expérimentales. Il est notamment montré que les différents phénomènes observés sont retrouvés numériquement pour les unidirectionnels et partiellement pour les tissés et que les valeurs prédites sont globalement en bon accord avec les mesures expérimentales. L'obtention de résultats réalistes nécessite une résolution en 3D avec un maillage relativement fin dans l'épaisseur. Finalement des méthodes numériques avancées sont mises en place afin de tenter de réduire le coût des simulations.

Mots clés
Préimprégnés UD, préimprégnés tissés, propriétés rhéologiques, simulation de procédé, écoulement de compression, fluide isotrope transverse (TIF), complément de Schur, décomposition en modes propres généralisée (PGD)

Abstract

The design freedom of composites can be improved by combining continuous and discontinuous prepregs. The forming of a pre-heated blank made of optimally oriented and distributed discontinuous prepreg plies may lead to unacceptable defects such as in-plane and out-of-plane wrinkles, sliding of plies, rotation of adjacent plies, bending of fibres induced by transverse squeeze flow and finally to inappropriate and inefficient fibre distribution. This arises because the individual discontinuous plies are free to move and deform in the mould during the forming step. First, this work presents some experiments conducted to identify the behaviour of a stack of unidirectional and woven discontinuous viscous prepregs subjected to through-thickness compression. Then a model based on a heterogeneous transverse isotropic fluid approach is gradually developped in agreement with the experimental findings. It is shown that the various observed phenomena are retrieved for the unidirectional and partly for the woven prepreg by the numerical model. The predicted values are in good agreement with measurements, when the problem is solved in 3D with a relatively fine mesh in the thickness. Finally an attempt is made to reduce the computational cost by the use of advanced numerical simulation techniques.

Key Words
UD prepreg, woven prepreg, rheological properties, process simulation, squeeze flow, Transversely Isotropic Fluid (TIF), Schur complement, Proper Generalized Decomposition (PGD)

Remerciements

Je souhaite avant toute chose remercier du fond du cœur ma femme Nimeüe pour son soutien continu toutes ces années, sans la patience de qui cette thèse, et tout ce qui a précédé, n'aurait probablement jamais abouti. Ceci est vrai également pour mes deux enfants, Myfanwy et Taliesin, à qui j'adresse aussi mes remerciements, bien qu'ils ne s'en rendront compte que dans quelques années.

Je souhaite également remercier ma famille, et particulièrement mes grand-parents et mon père, pour tout l'amour et le soutien qu'ils m'ont apporté depuis le tout début. Je leur dois toute une partie mémorable et très agréable de ma vie. Je remercie bien sûr spécialement ma sœur et mes frères.

Je remercie vivement Alexis et Quentin pour leur bonne humeur permanente et leurs visites "Tchaka-poum" régulières.

Je tiens à remercier Christophe, Adrien et Sébastien pour l'encadrement scientifique et humain de cette thèse, leur disponibilité, leur aide ainsi que leurs précieux conseils tout du long (et quelques très bonnes blagues). Cette thèse fut pleine de rebondissements mais je ne pouvais l'imaginer plus enrichissante ou plus intéressante. Je remercie aussi Jean-Michel pour toute l'aide logistique pour la partie expérimentale, et les stagiaires qui ont réalisé lesdites expériences.

Je n'oublie bien sûr pas tout les autres membres de l'équipe, les échanges lors des pauses café et les pâtisseries partagées. J'adresse un remerciement spécifique à Nicolas pour avoir accepté d'échanger son écran pour un (légèrement) plus petit.

Je tiens également à remercier Michel, Laurent et Anthony pour m'avoir fait suffisamment confiance pour me laisser enseigner dans leur cours. Cette expérience d'enseignement a été particulièrement intéressante, instructive et formatrice.

Je remercie le Ministère de l'Enseignement Supérieur et de la Recherche pour m'avoir accordé une allocation pour faire ma thèse en me laissant complètement libre du sujet et du contenu, c'est une opportunité incroyable que j'ai grandement appréciée.

Contents

List of Figures

List of Tables

General introduction

Introduction

One of the key advantages in designing fibre reinforced polymer composites is design flexibility. Polymer composites can be shaped in very complex forms to meet design requirements. An important distinctive property of continuous fibre reinforced polymer (CFRP) is its high stiffness to weight ratio, making it suitable for structural components. Glass and carbon fibres are primarily used for structural applications; however only carbon fibres can fulfil the highest specifications. There is a choice between two classes of polymers, thermoset or thermoplastic polymers. The latter, re-moulded multiple times as long as properties are kept at an acceptable level, makes components more suitable for recycling and assembling by welding technologies. The ability of thermoplastics to melt allows for fast and cost-effective manufacturing processes, which is a crucial property for the automotive industry. A key question concerns the processing technology able to manufacture the part as designed, to meet very short cycle times.

Although some processes like pultrusion and filament winding can process individual yarns to produce parts, fibres are usually arranged in the form of sheets, either in the form of dry textile products or in the form of prepregs. A prepreg is a flat sheet that combines fibres and thermoplastic or an uncured thermoset matrix. To get a structural 3D part at a production rate suitable for the automotive industry, one of the available processes is to form the initially planar prepreg into a final 3D shape during forming. As far as automotive applications are concerned, low cycle time processes are sought. Good candidates are thermo-stamping processes where a pre-consolidated flat thermoplastic laminate is heated up above the melting temperature of the polymer matrix, and when the matrix material has melted, it is formed into the final 3D shape. Typical examples of technologies are autoclave-forming, diaphragm-forming and press-forming. Autoclave-forming and to a certain extent diaphragm-forming are too labour-intensive and not fast enough for mass-production. On the contrary, in press-forming the flat laminate, produced automatically by press-forming production method, are cut to obtain a preform, heated up, consolidated and cooled down in the mould, and finally demoulded once it is stable enough. These operations can be automated, resulting in a cycle lasting a few minutes, which is the target for mass production in the automotive industry. This technology, suitable for mass-production, is very attractive for the automotive industry because it can produce large numbers of composite products with very good mechanical properties in a cost efficient way. In order to keep the design flexibility, the main concern is to control the fibre orientation and reduce the remaining defects to under an acceptable level, while maintaining rapid production.

Currently, new promising methods like automated fibre placement (also called automated tape laying) are under development as well. Though it is a costly process, it increases the design flexibility even further by allowing full control of the fibre deposition. However current technologies are not fast enough to be used for the mass production of composites. An alternative is to further develop the thermo-forming of thermoplastic materials combining continuous and discontinuous prepregs. Discontinuous prepregs are patches used to locally strengthen the part. They can be viewed as an intermediate material solution between the large continuous sheets and individual yarn. The structural analysis helps to identify locations where a part needs to be particularly reinforced with continuous fibre reinforced composites and where the part is less mechanically loaded, allowing cheaper composites to be used. Based on that information, parts can be optimally designed to improve the design with respect to cost.

Forming of discontinuous prepregs

A good example of technology that can offer a good trade-off between flexibility in design and a high production rate is the new technology QSP® (Quilted Stratum Process) developed by CETIM and its partners. This technology is based on a new design and manufacturing concept applied to structural thermoplastic composite parts initiated by Cetim and École Centrale de Nantes in 2012. It aims at providing a solution to a major challenge: produce high quality composite parts at a cost equivalent to that of a steel part in a context of middle to high rate production, especially for the automotive market. The QSP® relies on the manufacturing of a multi-thickness / multi-material blank made of pultruded unidirectional patches and discontinuous woven thermoplastic prepregs. This blank is then preheated, formed under press and overmoulded, leading to a net shaped part in one operation. The main advantages of this technology are:

- The us of noble (and costly) materials only where necessary (traditional technology uses noble organo-sheets with the same thickness throughout).
- Greatly reduced wasteage (with traditional technology, 30% to 40% of noble materials can be scrapped).
- Significant reduction in the weight of the final part.
- The making of composite parts with very short tact time (about 1 minute),
- The avoidance of costly reworking after forming (machining, assembly for example).

Besides these many advantages, there are still some difficulties to overcome. Removing the pre-heated blank from the tool under the press without holding the material leaves the patches free to move in the mould during the forming step. Figure 1b shows the blank designed to be formed to obtain a curved hat-shaped framing component. A discontinuous woven prepreg placed on the right-hand side of the blank is initially aligned with the component axis. After forming to obtain the hat shape, this patch experienced a rotation as shown in Figure 1c. No in-plane shearing is observed because the forming of the component in this region consists of squeezing and folding the discontinuous prepreg. On the left-hand side of the tailored blank, a discontinuous unidirectional prepreg underwent a large transformation as seen in Figure 1a. Fibres are no longer straight and the ply dimensions are not controlled due to the large squeeze flow. Pure sliding of discontinuous prepregs are also observed in vertical zones as a consequence of the mould closing.

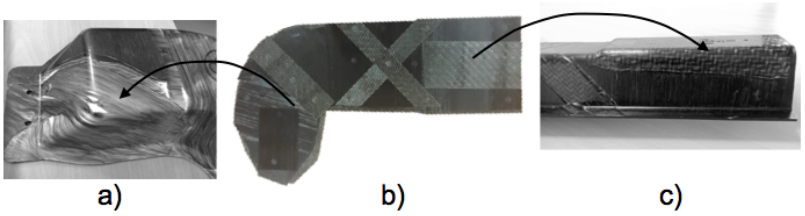

Figure 1 – a) UD prepreg deformation and sliding, b) flat multi-material blank before forming, c) woven prepreg rotation [44].

As thermoplastic composites become a more popular material for use in automotive applications, quality part production without extensive experimental investigations into the processing regime is needed. Part quality is degraded by a variety of defects which develop during processing. The occurrence of resulting defects has to be studied and understood in order to take them into account in the design step of the composite part. Table 1 reports the most frequent defects observed during the thermo-stamping of melted thermoplastic prepregs, including those processed with the Quilted Stratum Process (QSP®) presented by [44]. They are listed in decreasing levels of severity. These defects were also presented in [45].

Unlike plastic sheets, metal or Glass Mat Thermoplastics (GMT), the formability of regular composite prepregs does not depend on the plasticity of the prepreg material itself but on the draping characteristics of the prepreg and the off-plane relative displacement between laminated layers. It is difficult to decide whether a part can be formed without any defects. The problem to solve is the position of the prepreg during the forming process to prevent wrinkles or folds in the part. It is important to know in advance where issues during forming may occur and can be solved. The thermo-stamping of complex laminates made of discontinuous prepregs of finite dimensions raises new questions about their formability. The forming processes can lead to unacceptable defects like wrinkles, the sliding of patches and the bending of fibre induced by squeeze flow or inefficient fibre distribution. By inefficient fibre distribution we mean fibres not oriented in the main loading directions in critical regions after forming. These defects depend on several parameters, like the geometry of the part, material properties, lay-up, process parameters and friction between prepregs and between the top and bottom prepregs and mould. The individual discontinuous plies in the material can slide with respect to each other and deform individually. Patches are not maintained by a blankholder or any device used to apply in-plane tensile loadings to the plies to control their motion. In this case the interlaminar shear effects can play a significant role in the forming of multi-layered composite parts, especially when patches are introduced in the lay-up. Due to its important lubrication function, the thermoplastic matrix decreases interply friction and therefore facilitates slip deformation. It can lead to restriction of the motion of fibres in the prepreg. A resin rich layer exists in between prepreg plies, where the two resin rich layers on either side can represent about 5% of the total thickness [46]. It affects the outcome of forming processes [47] [1]. Viscoelastic effects can occur when fabric deformations occur too quickly.

Designing both the part and process through a trial and error procedure may lead to an increase of labour costs, machine time, tooling costs and scrap products. Current practice to determine the so-called defect tolerance is based on heavy experimental investigations, which is unsuitable to the development of cost-efficient composites. The production of

Defects	Most frequent origin	Mechanical influence on composites
In-plane fibre waviness	• Friction on tooling • Inter-ply friction • In-plane compression of prepregs • Transverse squeeze flow	• Local stiffness weakening • Reduction of tensile and compression strength • Higher risk of local buckling
Off-plane fibre waviness	• Buckling of fibres in part radii • Ply washing due to high injection pressure during overloading	• Local stiffness weakening • Reduction of tensile and compression strength • Higher risk of local buckling
Wrinkles	• High shearing in 3D shape • Lack of room in the mould cavity	• Equivalent to a broken ply
Delamination	• Inappropriate thermal management of the process	• Bending strength weakening
Incomplete impregnation	• Pre-existing defect in prepregs	• Early transverse cracking
Porosities	• Too much moisture in polymer	• Weak effect due to the high toughness of thermoplastics
Residual stresses	• Thermal mismatch between fibre and matrix • High chemical shrinkage of polymer	• Overloading conditions in some areas of the part

Table 1 – Most frequent defects observed in the thermo-stamping of thermoplastic viscous prepregs, including those obtained with the Quilted Stratum Process (QSP®).

quality parts without extensive experimental investigations is needed. Due to the complexity of the problem, the need for simulations is obvious. Numerical tools can simulate the production processes and provide to the subsequent FEA a material-scale description of the "as-manufactured" part. They can help the designer to optimize the product in the design phase and lead to a first-time-right production cycle. These optimizations require a robust, accurate and fast enough numerical procedure. They also need to create a direct link between the process simulation and the structural analysis. The state-of-the-art procedure is to chain software packages so that the outcome of the process simulation can be interpreted as the income of the structural analysis. When forming a flat fabric composite laminate into a 3D shape, the original arrangement of the fibres is strongly modified. The product shape and the forming process kinematics affect the extent of the fibre reorientation. The outcome of the first numerical tool is not only the new orientations of fibre but also potential defects created during the process. The outcome of the second computation is the assessment of whether a defect is acceptable or not, with regards to its consequence on the part strength.

Forming modelling and simulation

In continuous fibre reinforced polymer deformation is constrained by the array of continuous fibres. The inextensibility of very stiff fibres means that tensile deformations along the fibre axis are prevented. In a material where extension is prevented by the inextensible fibres, deformation must rely on shear mechanism, bending and transverse squeeze flow. Understanding how to form a complex shape part from inextensible material is a difficult task and requires knowing which of those deformations processes are admissible. The main deformation mechanisms are bending, axial and transverse intraply shear, interply slip where the lubricant polymer will play a crucial rule, flow of polymer through and along the fibre bed when the polymer is squeezed out through the fibres and squeeze flow.

While most deformations involve relatively small overall strains, some of them may be much more pronounced. That is the case when plies slide past each other in opposite directions, or move in the same direction but at different velocities. During the deformation into a 3D shape of a multilayered composite, interply slip must occur. If interply slip is hindered by lack of slippage between plies, out-of-plane buckling of one or more layers may happen, especially in the interior of the part. This viscous deformation, also called interply slip, is limited to the resin rich layer in between plies and in between the mould wall and the top and bottom layers. Such deformations are of the order of 10 mm or even more, especially in discontinuous layers which is the focus of this work. For most thermoplastic polymers with shear-thinning behaviour, it means that the non-Newtonian behaviour of the fluid can be revealed in the process. If the process time scale is long and the resin viscosity is low, then forming may cause polymer to be squeezed out or there may be excessive transverse flow. On the contrary, too high a viscosity and too short a time scale means that the reinforcing fibres are unable to adjust to the flow and may buckle, particularly on the inside of bends. Correct control of process parameters with respect to the prepreg properties allows interply slip to occur and the UD microstructure to be conserved.

There are two main approaches in composite forming simulations: the geometrical / kinematic approach and the mechanical/Finite Element (FE) approach. The first one is very fast and sufficient for very simple geometries where only fibre reorientation is looked at for preliminary design purposes. However that approach cannot be used here since the effects of inter-ply sliding or squeeze flow cannot be included, to name but two. Fibre reorientation can be generated by the transverse squeeze flow in multi-axial discontinuous

laminates [48]. It is also observed that fibres can deform so that the initial rectangular sample becomes barrel-shaped [49]. These mechanisms cannot be taken into account in a pure kinematic approach. FE simulations are based on solving equilibrium for the complete structure. They can include complex material models and boundary conditions. Finite element forming simulations of multi-layer composites have become common in commercial FE packages now [50].

However forming simulations of multi-layer composites including lubrication, squeeze flow and large slippage phenomena is still in a research stage [51], [52]. Stacking several plies with contact laws between each layer is the most common method to model forming. The forming behaviour of multi-layered composites is often modelled by stacking multiple element layers through the thickness of the sheet and connecting them by friction laws. However, as previously mentioned, within the range of allowable deformations, there are some situations where the discontinuous viscous prepregs slide past each other. Modelling that mechanism requires a viscous model where the matrix plays an important role. Also suitable constitutive relations are required in this mechanical approach. They can be generally classified under the assumption that the prepreg material is modelled either as a fluid or a solid. Originally, owing to some similarities between the thermoforming of thermoplastic composites and metal sheet forming, a first approach is to view the composite sheet as a deformable anisotropic solid and to use the displacements as the primary variables. This solid mechanics approach is based on the use of elasto-plastic models. When finite and permanent deformations occur, a visco-plastic model is preferred to describe the behaviour of the deforming material, supposing elastic effects can be neglected [53]. This second approach is usually referred to as the flow formulation for forming processes [54]. In this technique, the material is viewed as a viscous medium and the velocities are the primary variables. Since the behaviour of the discontinuous viscous laminate at its forming temperature involve large transformation and deformation, sliding over long distance and squeeze flow, the flow formulation along with a constitutive equation for viscous anisotropic medium seems appropriate. The kinematical constraints, anisotropic behaviour, sliding and finite deformations create special situations which must be taken into account in order to successfully investigate the formability of discontinuous viscous composite laminates and to optimize the processing parameters in the forming process.

To do so, Chapter 1 presents dedicated experiments on instrumented viscous laminates to measure large-deformation including changes in fibre orientation and inter-ply rotation. Experimental findings are used to build a multi-layer heterogeneous 3D model. Chapter 2 presents a 2D Transversely Isotropic Fluid (TIF) model, solved by FE and validated through various numerical test cases. Then a more realistic 3D model is proposed in chapter 3 and validated against experimental measurements. Chapter 4 discusses the advanced numerical simulation of the 3D problem with the aim of reducing the CPU and memory requirements.

Chapter 1

Experimental part

This Chapter focuses on the through-thickness compression of unidirectional, cross-ply and woven discontinuous viscous prepreg laminates. A series of experiments and characterisation are presented to better understand the flow kinematics induced by the compaction tests. To do so, new experiments are designed to distinguish between solid rotation of a patch and in-plane bending of yarns within the patch. Patch size effects are also investigated.

Contents

1.1 Experimental setup

1.1.1 Kinematic tracers

A 80x80 mm^2 grid of thin copper threads of 0.1mm in diameter was added at some interfaces between plies to probe the interface flow. One array of parallel threads aligned with adjacent plies is inserted at the interface. To form a grid, a second array of parallel threads can be placed at another interface between adjacent plies aligned in the second stacking direction. The two arrays of tracers are not inserted at the same interface as they would significantly increase the interface thickness and possibly interact with each other, leading to inaccurate results. A visual description of the configuration is presented in Figure 1.1.

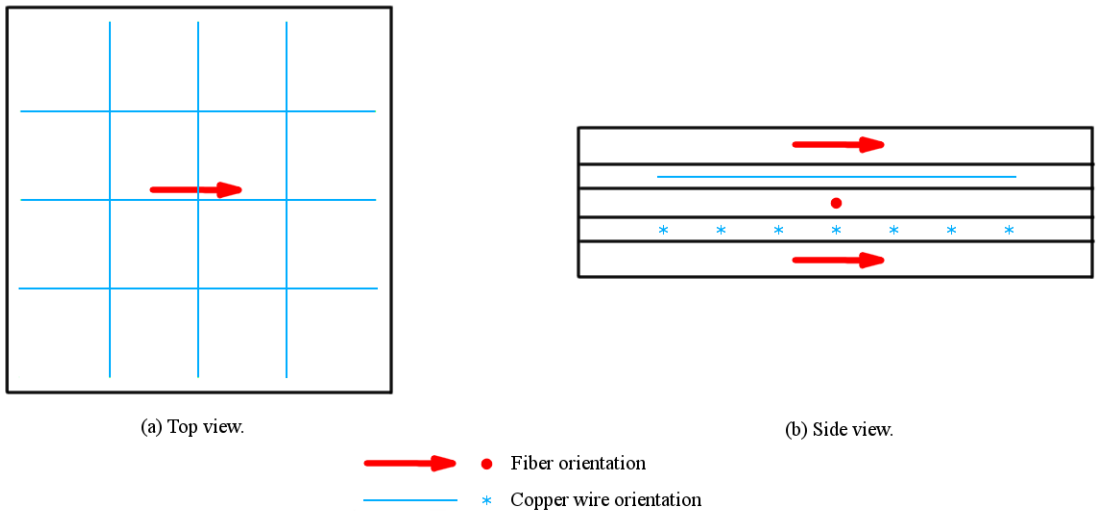

Figure 1.1 – Configuration of the copper threads.

The dimension of the tracers is higher than the average thickness of the resin interface, however it does not have an impact on the flow as their reaction force due to their stiffness is very low compared to the drag forces due to the viscosity of the matrix. Futhermore they will be convected by the resin in the same fashion as the fibres are, considering that the flow is induced by the through-thickness compression. While their exact position in the thickness cannot be controlled, they will penetrate the sheet of fibres with which they are aligned. They therefore remain an interesting solution to inspect the configuration of the fibres.

As these tracers are dragged by the viscous polymer at the interface between two plies they provide useful experimental data to be compared to model predictions. Both the initial and final 2D geometry of the grid are obtained from a high-resolution X-ray computed tomography (CT) scanner (X-Radia Carl Zeiss). The high contrast between the copper threads and the carbon or glass fibre polymer composite allows fast scanning with a very high accuracy. This is done to investigate the fibre rotation as the pressure due to the normal compressive load makes the molten polymer squeeze and flow, which makes the fibre rotate and/or bend. The angles between the copper threads are measured before and after the compaction to measure the rotation of the fibres.

1.1.2 Unidirectional specimens

The material used in the experiments is a unidirectional carbon fibre-reinforced epoxy prepreg (Hexply M21/35.5M%/268/T700GC from Hexcel) of 56.9% nominal fibre volume fraction. As it is a material of industrial grade, the given properties are subjected to statistical variations. The experiments are conducted on uncured thermoset unidirectionnal prepregs because the principal desired characteristic being the material to be a linear viscous fluid. As a monomer is very likely to stay in its linear domain regardless of the rate of shear, this assumption is considered reasonable. Futhermore, considering that the charge added in the material is of small dimension compared to the ply, the resin rich layer can be considered an homogenized fluid which viscosity is the one provided by the manufacturer. Individual plies have a nominal cured thickness of 0.262 mm. 150x150 mm^2 samples with 3 stacking sequences (UD, cross-ply and angle-ply) were considered. The ply edges are left unconstrained which allows them to expand and rotate freely. Specimens were squeezed in the thickness direction with a slow monotonic loading applied by a press in the range of 250kN to 400kN. The final thickness of the specimen is controlled through the use of spacers, limiting the reduction of the thickness. Compaction experiments are run on uncured unidirectional prepregs.

The application of a compaction force produces a pressure gradient within the material that induces transverse flow. This transverse flow allows fibres to spread sideways under normal compressive load. Because the fibres are inextensible, the sample ply cannot expand along their axis but resin can be squeezed out in that direction if the resin viscosity is low enough. The viscosity evolves with the temperature and the degree of cure, but as the thermo-stamping is a fast process there is no evolution of these properties. In order to perform experiments at a constant viscosity, preliminary tests are carried out to determine the range of temperatures and time scales where the degree of cure does not evolve and the viscosity is high enough to generate pure squeeze flow without resin bleeding in the fibre direction. The results of these tests are a maximum temperature of 80°C and a maximum processing time of 30 minutes at that temperature. Higher temperatures are close to the transition from squeezing to bleeding flow as observed in [55]. During the actual tests the time limit is never reached as thermo-stamping is a very fast process, lasting only a few seconds.

1.1.3 Woven prepreg specimens

The materials used are the Dupont™ Vizilon™ SU75G1, the Dupont™ Vizilon™ SB75G1, the Dupont™ Vizilon™ SU63G1 and the Dupont™ Vizilon™ SB63G1. The SU75G1 and the SU63G1 are 4-1 biased plain weave glass fabrics (they have 80% of fibres in the warp direction and 20% of fibres in the weft direction) reinforced polyamide 66-6 prepreg material with a fibre mass fraction of respectively 75% and 63%. Based on the respective fibre content in the warp and the weft directions, these materials are intermediate between the woven and the unidirectional prepregs. The SB75G1 and the SB63G1 are balanced twill weave glass fabrics with otherwise the same characteristic as the Dupont™ Vizilon™ SU75G1 and SU63G1. Material properties are presented in Table 1.1.

The test specimen are made by stacking three plies of preconsolidated prepreg of size 150x150 mm^2 with three stacking sequences (0° ply, angle ply, 0° ply) where 20° , 45° and 80° angles were considered. The plies are cut accordingly to their respective angle 0°, 20°, 45° or 80°. The copper tracers grid can be seen in Figure 1.2a. The final thickness of the specimen including the grid is 5mm. The ply edges are left unconstrained to let the fibres expand and rotate/bend. An example of the final specimen is shown in Figure 1.2b.

Vizilon™	SU75G1	SU63G1	SB75G1	SB63G1
Fabric	4/1 biased plain weave		2-2 twill weave	
Warp / weft ratio (%)	80 / 20		50 / 50	
Thickness (mm)	1.6			
Fibre mass fraction (%)	75	63	75	63
Fibre volumic fraction (%)	57	43	57	43
Density (g.cm^{-3})	1.98	1.78	1.98	1.78
Melting temperature (°C)	260			

Table 1.1 – Properties of the Vizilon™ prepreg sheets.

(a) Laying of copper threads along the fibre direction. (b) Specimen before compression

Figure 1.2 – Illustration of the test specimen made with the Vizilon™ prepreg sheets.

A compaction force of 100 kN was applied on the specimen where the mould plates are pre-heated to 260°C. The square specimen is placed inside the press with spacers of thickness 4.9 mm to control the thickness of the compressed specimen. It is maintained at the melting temperature for 5 min and finally cooled down gradually.

1.2 Experimental observations on unidirectional prepregs

1.2.1 Compression of a $[0]_6$ stack of Hexcel Hexply M21 prepreg

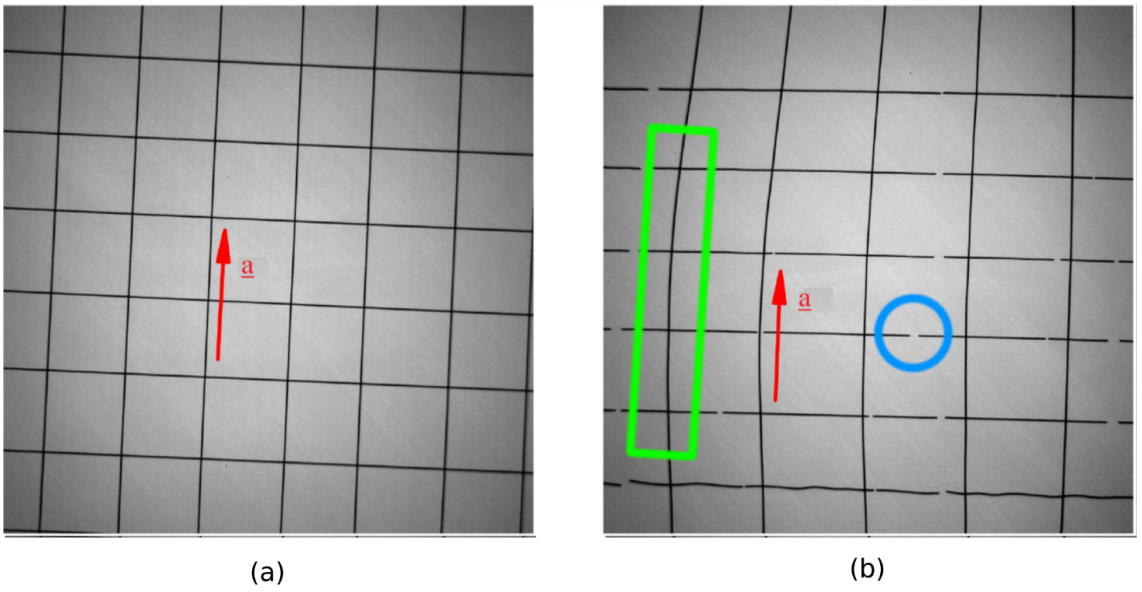

Figure 1.3 – CT-scan of the $[0]_6$ stack of Hexcel Hexply M21 prepreg, 400 kN compressive load. Red arrows represent the initial fibre orientation vector. (a) Before squeeze flow. Initial thickness: 1.85 mm. Initial grid space: 10 mm. (b) After squeeze flow. Final thickness: 1.30 mm.

Figure 1.3 shows the initial and final geometry of the grid for the $[0]_6$ stack. Initial fibre orientation is represented by the red arrow. The array of tracers orthogonal to the fibre direction was in the mid-plane, the parallel one on both sides of the fourth ply, counted from the bottom side of the stack. 60x60 mm^2 scans are taken in the center of the sample. The high transverse squeeze flow perpendicular to the fibres induced the breakage of copper threads aligned in that direction as can be seen in the blue circle, while the parallel ones remain intact (Figure 1.3b). This provides the evidence that a reaction stress develops in fibres to prevent the flow along their direction. The vertical tracers experienced in-plane bending, as can be seen in the green rectangle, that is more pronounced close to the lateral edges resulting from the squeeze flow kinematics.

1.2.2 Compression of a $[0/90]_6$ stack of Hexcel Hexply M21 prepreg

Figure 1.4 presents the initial and final geometry of the grid placed in the mid-plane of a $[0/90]_6$ cross-ply stack. Initial fibre orientations are represented by the red arrows. The horizontal array of tracers was inserted between the fourth and the fifth plies, the second array oriented in the vertical direction was inserted between the eight and the ninth plies. As revealed by these images, the orthogonality of the grid is kept as shown by the blue wedges, but unlike the UD stack, all tracers underwent some bending as can be seen in the green rectangle. The bending and spreading of the composite layers are clearly visible on the composite layers as indicated in Figure 1.5. The grid dilated of 15% on average as highlighted by the yellow double-headed arrows in Figure 1.4, which proves there is actually a viscous flow between the plies. While orthogonally oriented plies impede flow

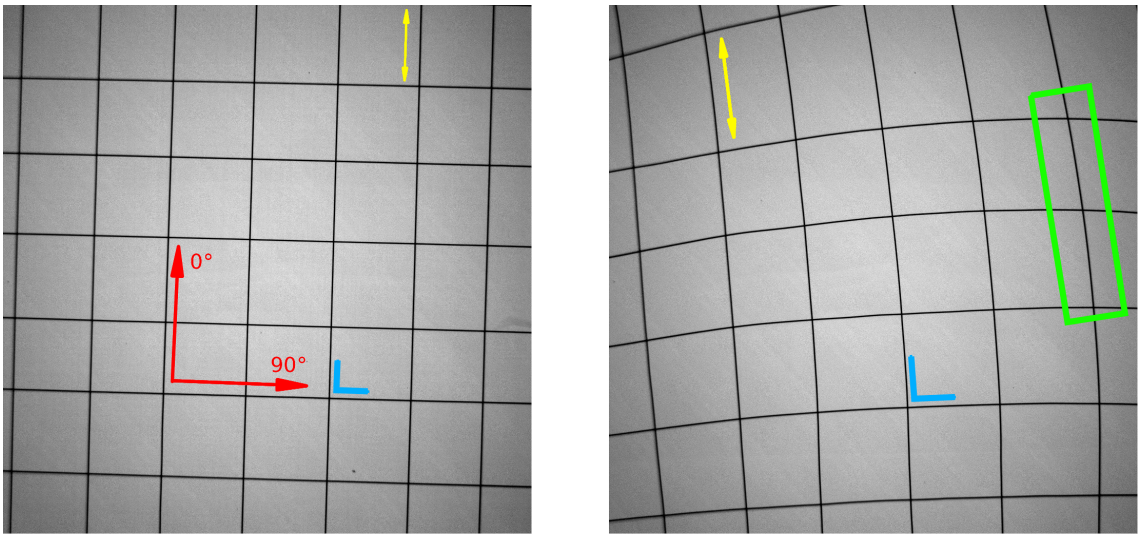

(a) (b)

Figure 1.4 – CT-scan of the $[0/90]_6$ stack of Hexcel Hexply M21 prepreg, 400kN compressive loading. Average expansion of the grid of 15%. (a) Before squeeze flow. Initial thickness: 3.15 mm. Initial grid space: 10 mm. (b) After squeeze flow. Final thickness: 2.38 mm.

in each direction within composite plies, they do not prevent the flow at their interface. This important observation is consistent with the existence of pure viscous resin layers in prepregs, as mentioned in Section . Even for prepregs with high fibre volume fraction, there is flow at ply interfaces.

Figure 1.5 – Photograph of the $[0/90]_6$ sample after compression.

1.2.3 Compression of a $[+30/\text{-}30]_3$ stack of Hexcel Hexply M21 prepreg

Figure 1.6 shows results obtained for a stack of plies with $[+30/-30]_3$ lay-up. The first array of tracers was in the mid-plane, the second one on both sides of the fourth ply, counted from the bottom side of the stack. The initial grid has a shape of a rhombus with a 60°angle corresponding to the total inclination of adjacent plies. A marker crossing one copper thread, highlighted in the blue square, is added to the grid for a more accurate comparison between the undeformed and deformed grids. Measurements made on three repeats indicate that the thin copper threads rotated 8° to 10° towards $[+45/-45]$ and kept their straightness in the center of the sample. This experimental finding confirms real composites observations reported in [48] for a composite substitute made of carbon fibre reinforced syrup. The grid dilated of 13% to 16% of its original spacing for the three repeats. The $[0/45]_3$ stack of 1.7mm initial thickness, squeezed under 350kN up to 1.2mm in thickness exhibited the highest rotation, typically 14°, for the same squeeze rate than the one applied to the $[+30/-30]_3$ lay-up.

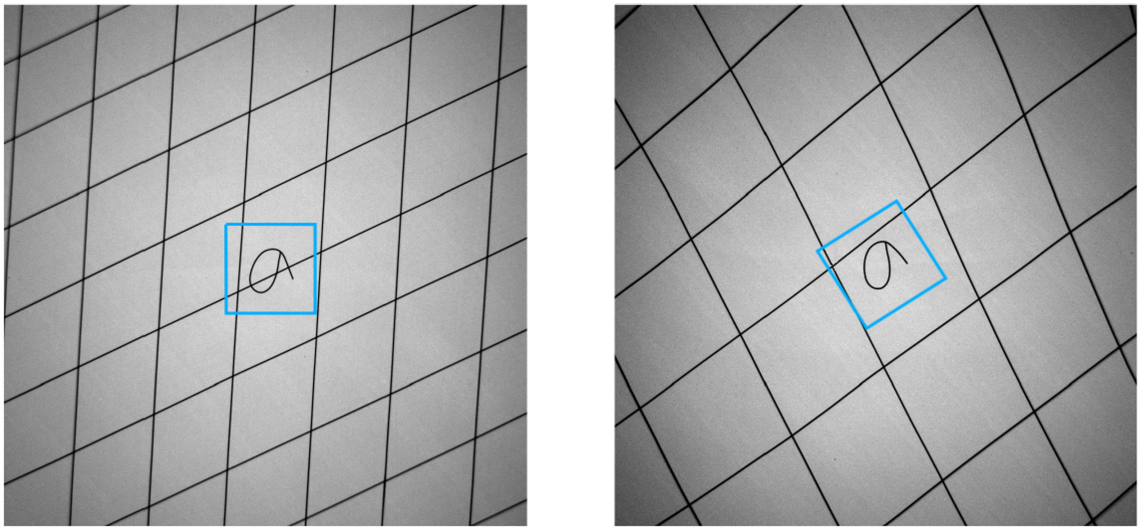

(a) (b)

Figure 1.6 – CT-scan of the $[+30/-30]_3$ stack of Hexcel Hexply M21 prepreg, 350kN compressive loading. Tracers in the mid-plane. Average expansion of the grid between 13% to 16% on 3 repeats. (a) Before squeeze flow. Initial thickness: 1.75 mm. Initial grid space: 10 mm. (b) After squeeze flow. Final thickness: 1.25 mm.

1.2.4 Copper threads kinematics

Figure 1.3 presents the CT-scans of the $[0]_6$ stack before and after compression. The vertical threads barrel, as can be expected from a stack of UD under compression, whereas the horizontal threads break, confirming that the copper threads are mostly at the interface as no carbon fibers were broken during the compression test.

Figure 1.4 presents the CT-scans of the $[0/90]_6$ stack before and after compression, and Figure 1.5 presents the photograph of the stack after compression. The Figures show that all threads barrel and spread in the same fashion as the fibers.

It can therefore be concluded that while the copper threads can be thicker than the interface layer they are mostly located in the inter-layer zone, and their kinematics are representative of the kinematics of the fibers.

1.3 Experimental observations on woven prepregs

1.3.1 Compression of a [0/20/0] stack of Vizilon™ SU75G1 prepreg

For the first compression tests the Dupont™ Vizilon™ SU75G1 prepreg is considered. A 150x150 mm^2 stack of one 20° orientation ply in between two 0° plies was subjected to compression. Measured rotation values are presented in Table 1.2.

Measurements give the evidence that the middle layer rotates with respect to the two outer plies. This is a phenomenon that was previously seen in angle-ply laminated made of unidirectional prepregs. It can be seen that fibres bent at the edges of the composite due to the resin flow towards the edges which modifies the orientation near the edges. The copper threads after compression show a certain degree of waviness, likely due to the crimp in the woven fabric. An average of 7.21° rotation in anti-clockwise direction of fibres is observed.

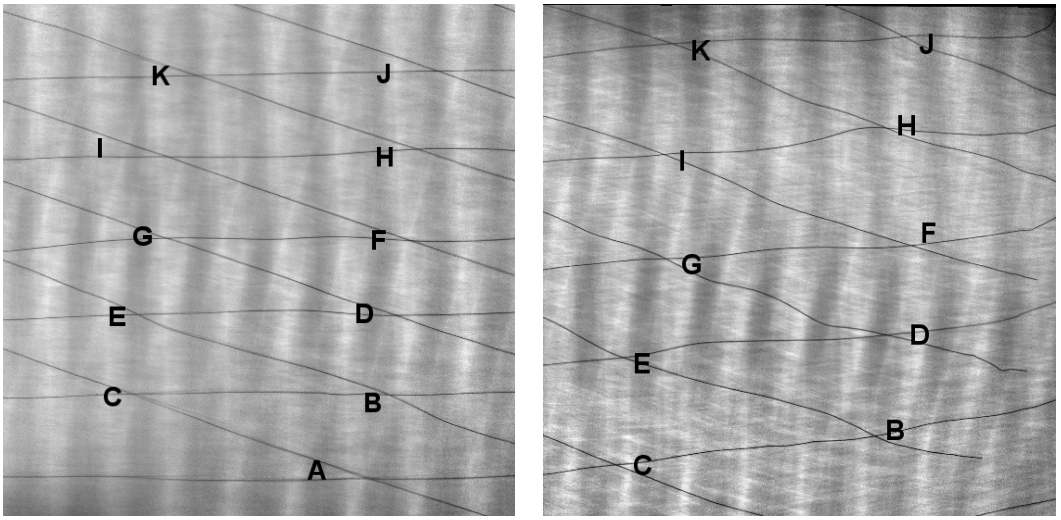

(a) Orientation of threads before compression. (b) Orientation of threads after compression.

Figure 1.7 – CT-scan of the [0/20/0] stack of Vizilon™ SU75G1 prepreg.

Label	Before	After	Difference	Label	Before	After	Difference
A	19.9	18.1	-1.8	G	22.6	31.3	8.7
B	17.0	34.6	17.6	H	20.4	22.2	1.8
C	18.7	36.4	17.7	I	18.3	24.7	6.4
D	17.0	38.5	21.5	J	20.6	20.29	-0.31
E	25.9	27.4	1.5	K	20.8	24.6	3.8
F	15.4	17.9	2.5				

Table 1.2 – Angles for the [0/20/0] stack of Vizilon™ SU75G1 prepreg.

1.3.2 Compression of a [0/80/0] stack of Vizilon™ SU75G1 prepreg

A 150x150 mm^2 stack of one 80° orientation ply in between two 0° plies was subjected to compression. The Dupont™ Vizilon™ SU75G1 prepreg is also used here. Measured rotation values are presented in Table 1.3.

Label	Before	After	Difference	Label	Before	After	Difference
A	80.3	77.9	-2.4	G	79.6	67.5	-12.1
B	78.2	76.0	-2.2	H	78.1	67.9	-10.2
C	80.6	76.5	-4.1	I	82.5	91.1	8.6
D	80.3	76.7	-3.6	J	78.6	81.2	2.6
E	79.7	76.3	-3.4	K	80.0	74.7	-5.3
F	79.0	94.4	15.4	L	79.2	79.6	0.4

Table 1.3 – Angles for the [0/80/0] stack of Vizilon™ SU75G1 prepreg.

The same phenomenon of fibres bending can be seen near the edges. As it can be seen from Table 1.3, there is closing of the fibres when subjected to compression.

The above CT-images in Figures 1.7a to 1.8b and the measured angles show that the fibres have opened i.e. rotated in the anti-clockwise direction in the [0/20/0] stack, while in the [0/80/0] stack most of the fibres have closed. An average of 1.35° rotation in clockwise direction of fibres is observed. No intra-ply shear was observed.

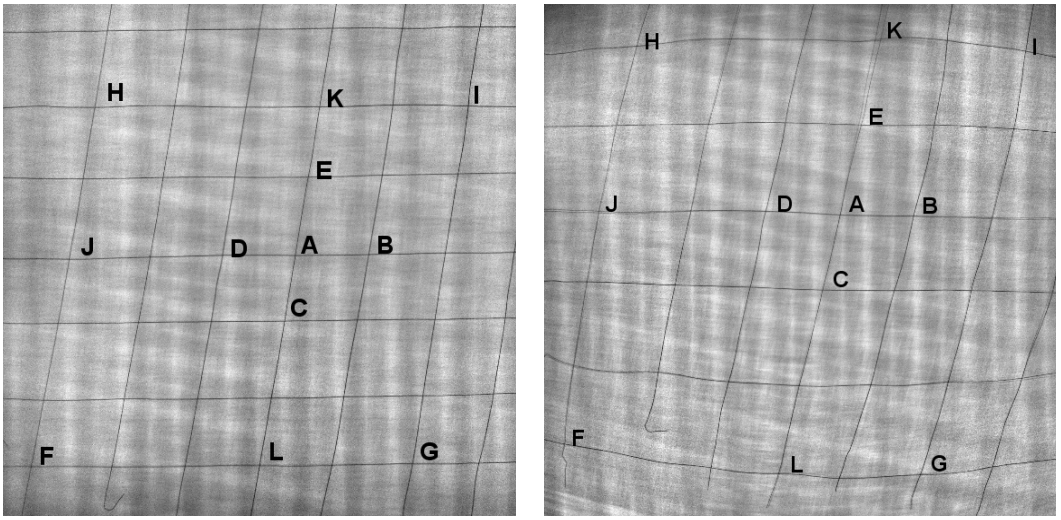

(a) Orientation of threads before compression. (b) Orientation of threads after compression.

Figure 1.8 – CT-scan of the [0/80/0] stack of Vizilon™ SU75G1 prepreg.

1.3.3 Influence of the specimen size

In the previous experiments specimens of size 150x150 mm^2 are examined for the assessment of fibre rotation under compaction of 100kN with no edges being constrained. Due to the fibre rotation in the edges as a result of transverse polymer flow, the fibre orientation is disturbed to some extent. Assuming that the size effect has an influence on the rotation of the fibres, further examination was conducted on larger specimens of size 300x300 mm^2. In order to observe the influence of the size the same Dupont™ Vizilon™ SU75G1 prepreg was considered. A stack of one 20° orientation ply in between two 0° plies was subjected to compression. The same test procedure as explained in Section 1.1.3 is followed. Figure 1.9 shows the grids installed between the prepreg plies.

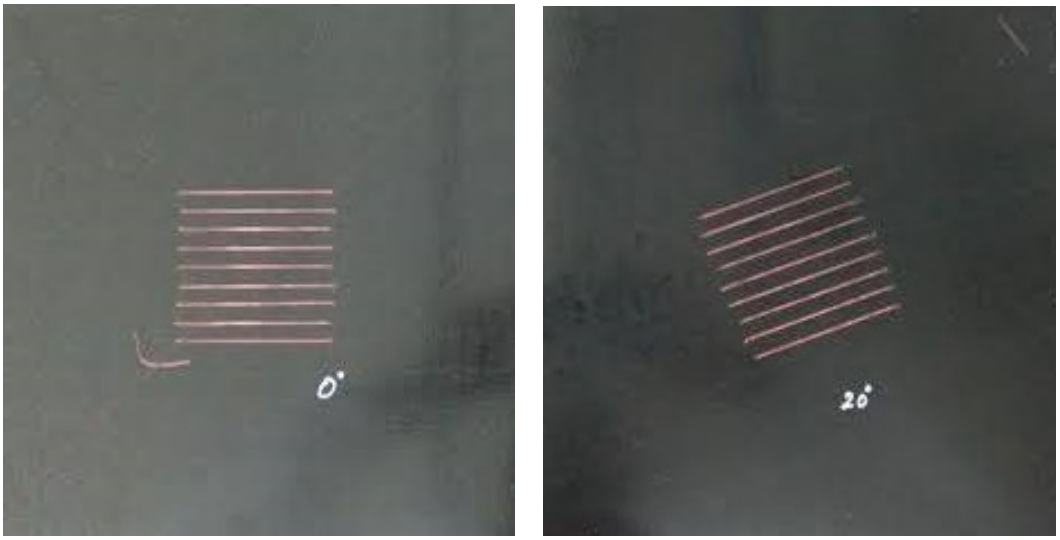

(a) 0° grid (b) 20° grid

Figure 1.9 – Illustration of the different grid lay ups to study the influence of the specimen size.

1.3.3.1 Compression of a [0/20/0] stack of Vizilon™ SU75G1 prepreg

An assembly of 20° orientation ply in between two 0° plies of the prepreg Vizilon™ SU75G1 was compressed under a pressure of 0.5 MPa at the melting temperature. Measured rotation values are presented in Table 1.4. The angles measured here are the obtuse angles at the points labelled in Figure 1.10.

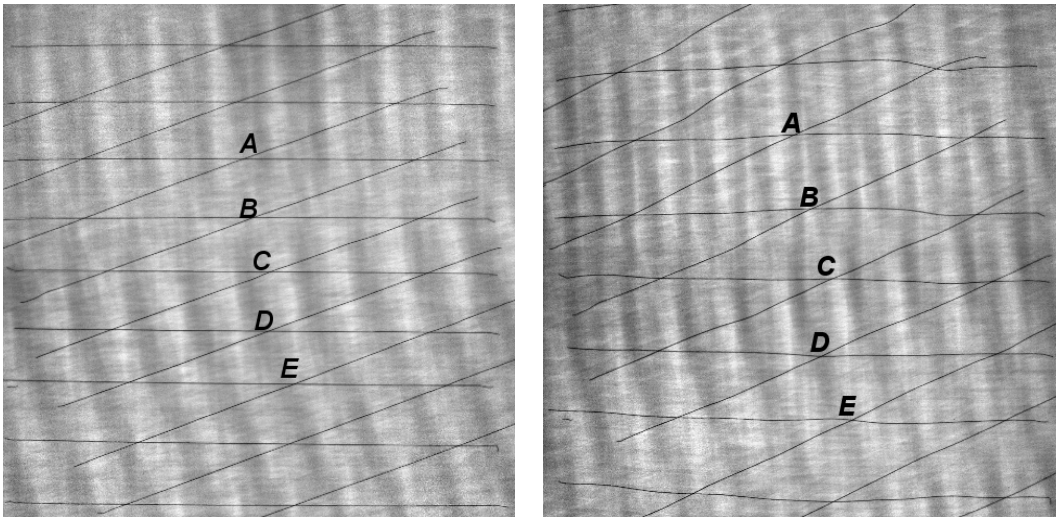

(a) Before compression. (b) After compression.

Figure 1.10 – CT-scan of [0/20/0] stack of Vizilon™ SU75G1 prepreg.

Label	Initial	Final
A	159	152.3
B	159.6	153.7
C	159.7	156.6
D	159.7	157.5
E	159	154.6

Table 1.4 – Initial and after compression at 0.5 MPa angles for the [0/20/0] stack of Vizilon™ SU75G1 prepreg.

It can be seen in Table 1.4 that the fibres have rotated and that there is an overall 4.46° rotation of fibres on average. However at point C in the center of the grid and the composite, a minimum rotation of 3.1° is observed. A slight bending at the edges of the grid confirms that the polymer flows towards the sample edges when subjected to compression.

Figure 1.10b reveals that there is no bending of the copper tracers in the grid directed towards the edges of the sample, which means that the rotation of the fibres is influenced by the size of the specimen.

1.3.4 Influence of the structure

The Dupont™ Vizilon™ SU75G1 and SB75G1 prepregs are considered in order to investigate the fibre rotation in both unbalanced and balanced woven prepregs. A first compression on a [0/45/0] stack will be conducted on the Dupont™- Vizilon™ SU75G1 prepreg to complete the data for the comparison, then on a [0/20/0] and a [0/45/0] stacks on the Dupont™ Vizilon™ SB75G1 prepreg. The same test procedure as explained in Section 1.1.3 is followed.

Figure 1.11 presents the 45° used and a picture of the final specimen before compression.

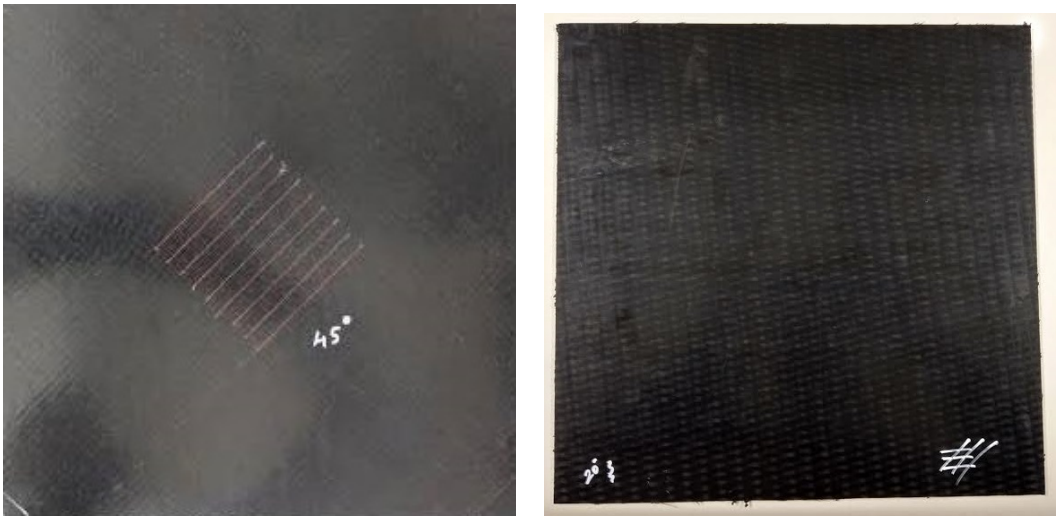

(a) 45° grid. (b) Final specimen before compression.

Figure 1.11 – Illustration of the 45° grid lay up and the final specimen to study the influence of the structure.

The overall fibre content and resin content is the same for both prepregs, they differ by the way the two constituents are distributed. This experiment with the above two prepeg materials will also helps us to investigate the influence of the polymer/fibre distribution on the fibre rotation.

1.3.4.1 Compression of a [0/45/0] stack of Vizilon™ SU75G1 prepreg

An assembly of 45° ply in between two 0° plies of the Vizilon™ SU75G1 was compressed at a pressure of 0.5 MPa at the melting temperature. Measured rotation values are presented in Table 1.5.

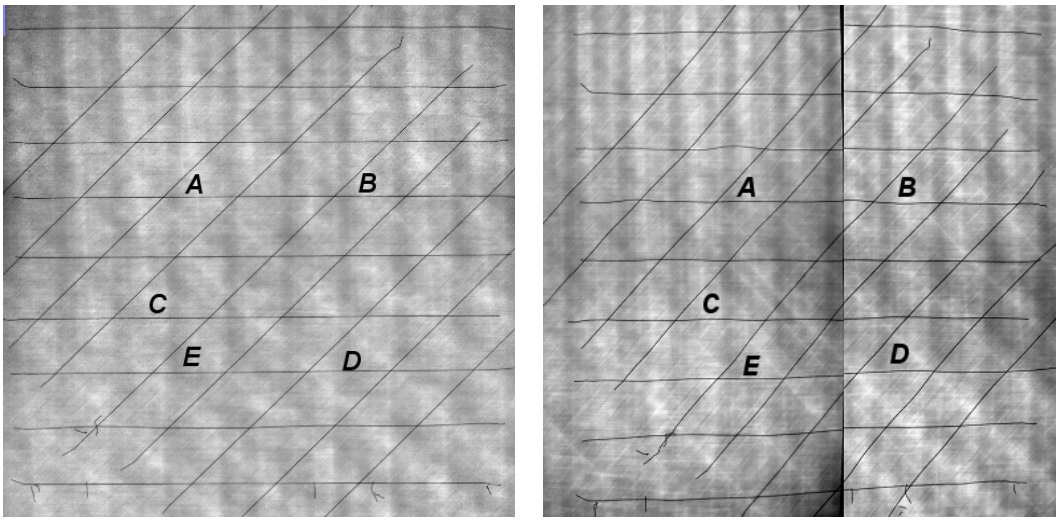

(a) Before compression. (b) After compression.

Figure 1.12 – CT-scan of [0/45/0] stack of Vizilon™ SU75G1 prepreg.

Label	Initial	Final
A	43.6	48
B	43.4	47.2
C	43.2	47.7
D	43.4	47.5
E	43.5	50.7

Table 1.5 – Initial and after compression at 0.5 MPa angles for the [0/45/0] stack of Vizilon™ SU75G1 prepreg.

It can be seen from Table 1.5 and Figure 1.12 that the fibres have rotated, and that there is an overall 4.8° rotation of fibres on average. It can be seen that the copper threads remained comparatively straight as of the initial orientation.

1.3.4.2 Compression of a [0/20/0] stack of Vizilon™ SB75G1 prepreg

An assembly of 20° oriented ply in between two 0° plies of the Vizilon™ SB75G1 was compressed at a pressure of 0.5 MPa at the melting temperature. Measured rotation values are presented in Table 1.6. The angles measured here are the obtuse angles at the points labelled in Figure 1.13.

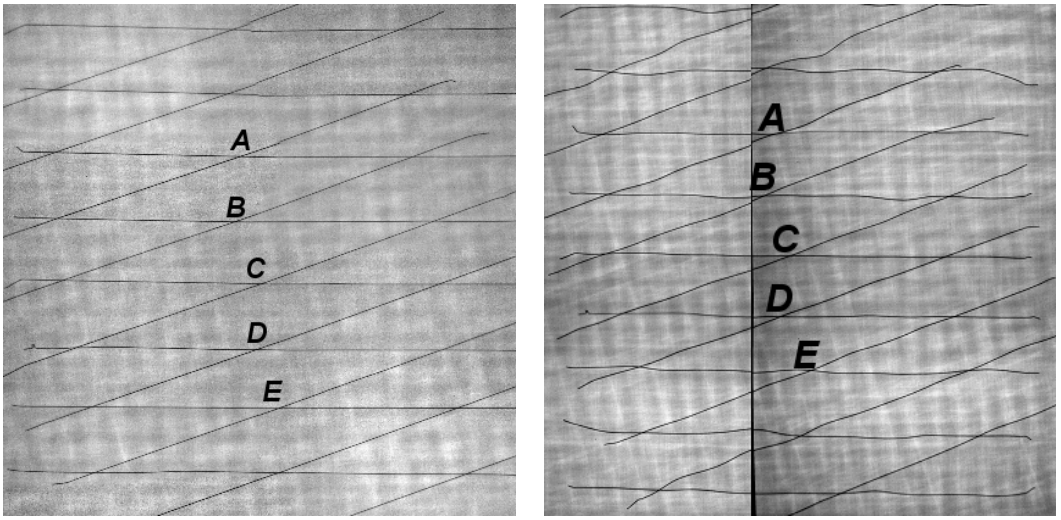

(a) Before compression. (b) After compression.

Figure 1.13 – CT-scan of [0/20/0] stack of Vizilon™ SB75G1 prepreg.

Label	Initial	Final
A	160	159.7
B	160.2	159.3
C	160.7	160.4
D	160.5	160
E	160.6	160

Table 1.6 – Initial and after compression at 0.5 MPa angles for the [0/20/0] stack of Vizilon™ SB75G1 prepreg.

It can be seen from Table 1.6 that there is almost no rotation of the fibres, which indicates that the balanced/unbalanced nature of the prepreg has an influence on the solid body rotation.

1.3.4.3 Compression of a [0/45/0] stack of Vizilon™ SB75G1 prepreg

An assembly of 45° oriented ply in between two 0° plies of the Vizilon™ SB75G1 was compressed at a pressure of 0.5 MPa at the melting temperature. Measured rotation values are presented in Table 1.7.

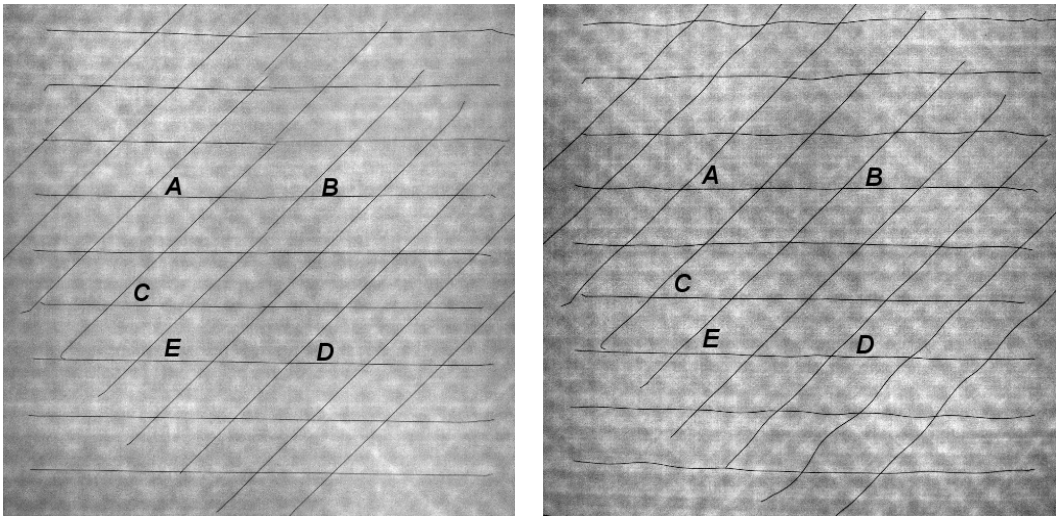

(a) Before compression. (b) After compression.

Figure 1.14 – CT-scan of [0/45/0] stack of Vizilon™ SB75G1 prepreg.

Label	Initial	Final
A	45	45.3
B	45	45.8
C	45	45.2
D	45.4	46.5
E	45	45.4

Table 1.7 – Initial and after compression at 0.5 MPa angles for the [0/45/0] stack of Vizilon™ SB75G1 prepreg.

It can be seen from Table 1.7 that there is almost no rotation of fibres.

It can be seen that the rotation of the fibres in the balanced prepregs (Figures 1.13b and 1.14b) is much lower than in the unbalanced prepregs (Figures 1.10b and 1.12b). Average rotations are recalled in Table 1.8. It is believed that the asymmetric flow of polymer in the unbalanced prepreg is the origin of this solid body rotation.

Stack	Average rotation [°]
Vizilon™ SU75G1 - [0/20/0]	7.21
Vizilon™ SU75G1 - [0/45/0]	4.8
Vizilon™ SB75G1 - [0/20/0]	0.52
Vizilon™ SB75G1 - [0/45/0]	0.56

Table 1.8 – Average rotation of the Vizilon™ SU75G1 and SB75G1 prepregs for different stacking sequences.

1.3.5 Influence of the fibre fraction

In the previous experiments specimens with a fibre mass fraction of 75% were considered. As the lubricative layer plays a very important role in the kinematics of a stack of prepreg plies during compression, experiments on specimens with a different viscosity were considered. One way to achieve different viscosity is to consider prepregs with a different fibre mass fraction. Compression tests were therefore conducted on a [0/20/0] and a [0/45/0] stacks of Vizilon™ SU63G1 and SB63G1 prepregs. The size of the specimens is 150x150 mm^2.

1.3.5.1 Compression of a left[0/20/0] stack of Vizilon™ SU63G1 prepreg

An assembly of 20° oriented ply in between two 0° plies of Vizilon™ SU63G1 was subjected to compression at a pressure of 0.5, 1 and 1.5 MPa at the melting temperature. Measured rotation values are presented in Table 1.9. The angles measured here are the obtuse angles at the points labelled in Figure 1.15.

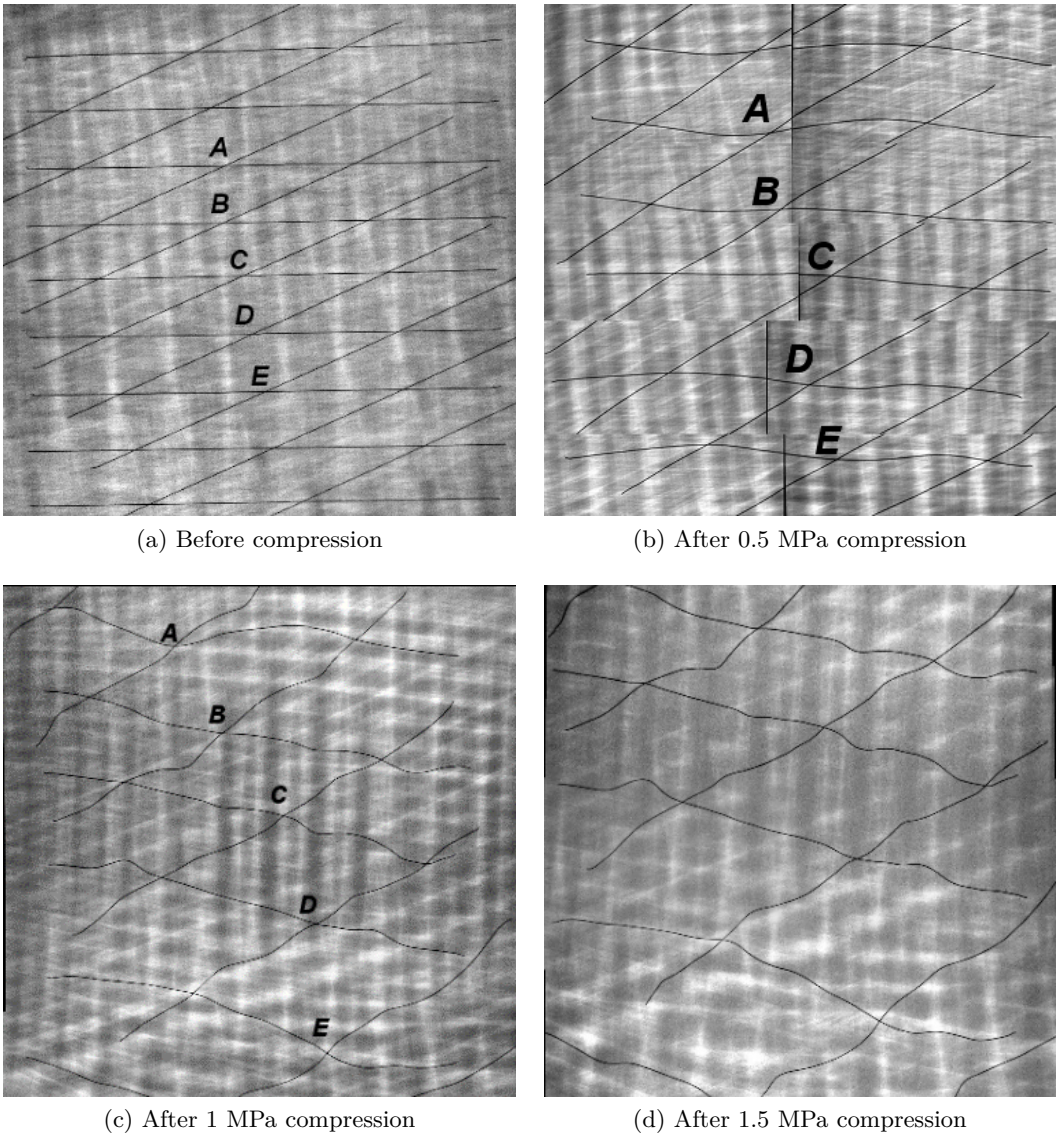

(a) Before compression

(b) After 0.5 MPa compression

(c) After 1 MPa compression

(d) After 1.5 MPa compression

Figure 1.15 – CT-scan of [0/20/0] stack of Vizilon™ SU63G1 prepreg.

	Angle [°]			
Label	Initial	0.5 MPa	1 MPa	1.5 MPa
A	156.7	151.8	150.4	-
B	156.6	146.9	143.5	-
C	156.4	143.9	133.7	-
D	156.7	147.6	137.1	-
E	156.5	151	147.1	-

Table 1.9 – Initial and after compression angles for the [0/20/0] stack of Vizilon™ SU63G1 prepreg.

It can be seen from Table 1.9 that the fibres have rotated and there is an overall 8.34° rotation of fibres on average in the anti-clockwise direction. However in the center of the ply (point C) a maximum of rotation of 12.5° is observed as the resin fraction in this case is high, and as the resin flow influences the fibre orientation in the fabric. Slight displacement of the fibres can be noticed under a compression of 0.5 MPa (Figure 1.15b) as the fibres are washed away by the resin flow when subjected to compression. Under 1 and 1.5 MPa compression (respectively Figures 1.15c and 1.15d) it can be noticed that the displacement of the fibres is dominent compared to the rotation of the fibres due to the resin flow, thus confirming the resin flow towards the edges of the sample. The orientation of fibres under 1.5 MPa compression is not measured as the orientation of the fibres is more influenced by the displacement of the fibres due to the flow induced by the pressure rather than the rotation of the plies. Section 3.2.1.4 will present the compression of a single UD ply with thickness variation of the interfacial resin layer, which generates a directional flow. The large displacements seen in Figure 1.15d can probably be explained by such a flow as the woven prepreg will present a thickness variation due to its structure.

1.3.5.2 Compression of a [0/45/0] stack of Vizilon™ SU63G1 prepreg

An assembly of 45° oriented ply in between two 0° plies of Vizilon™ SU63G1 was subjected to compression at a pressure of 0.5, 1 and 1.5 MPa at the melting temperature. Measured rotation values are presented in Table 1.10. CT-scans are presented in Figure 1.16.

	Angle [°]			
Label	Initial	0.5 MPa	1 MPa	1.5 MPa
A	45.8	50.2	53.6	57.4
B	45	42	47	49
C	45	47	51.7	58.9
D	45	51	58.8	68.4
E	45	51.2	59.3	68.3

Table 1.10 – Initial and after compression angles for the [0/45/0] stack of Vizilon™ SU63G1 prepreg.

It can be seen from Table 1.10 that most of the fibres have rotated and that there is an overall 4.32° rotation of fibres on average in the anti-clockwise direction, although in a few areas fibres have rotated in the clockwise direction. This phenomenon is more present at the edges of the sample where the bending of the fibres is more important due to the resin

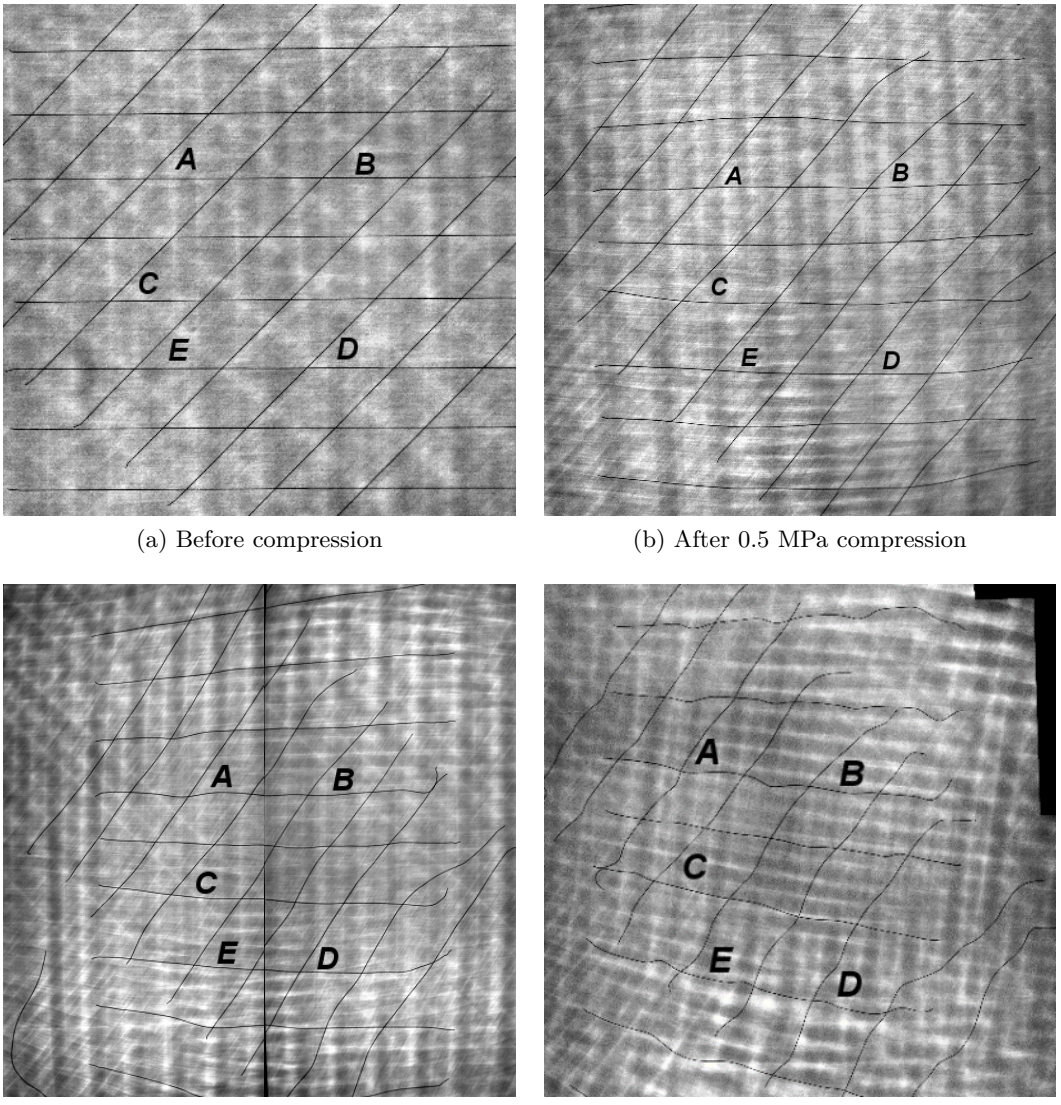

(a) Before compression

(b) After 0.5 MPa compression

(c) After 1 MPa compression

(d) After 1.5 MPa compression

Figure 1.16 – CT-scan of [0/45/0] stack of Vizilon™ SU63G1 prepreg.

flow towards the edges. Under 1 and 1.5 MPa compression (respectively Figures 1.16c and 1.16d) displacement of the copper tracers can be noticed due to more important drag forces. Displacement of the fibres are observed clearly under 1.5 MPa compression (Figure 1.16d).

1.3.5.3 Compression of a [0/20/0] stack of Vizilon™ SB63G1 prepreg

An assembly of 20° oriented ply in between two 0° plies of Vizilon™ SB63G1 was subjected to compression at a pressure of 0.5, 1 and 1.5 MPa at the melting temperature. Measured rotation values are presented in Table 1.11. The angles measured here are the obtuse angles at the points labelled in Figure 1.17.

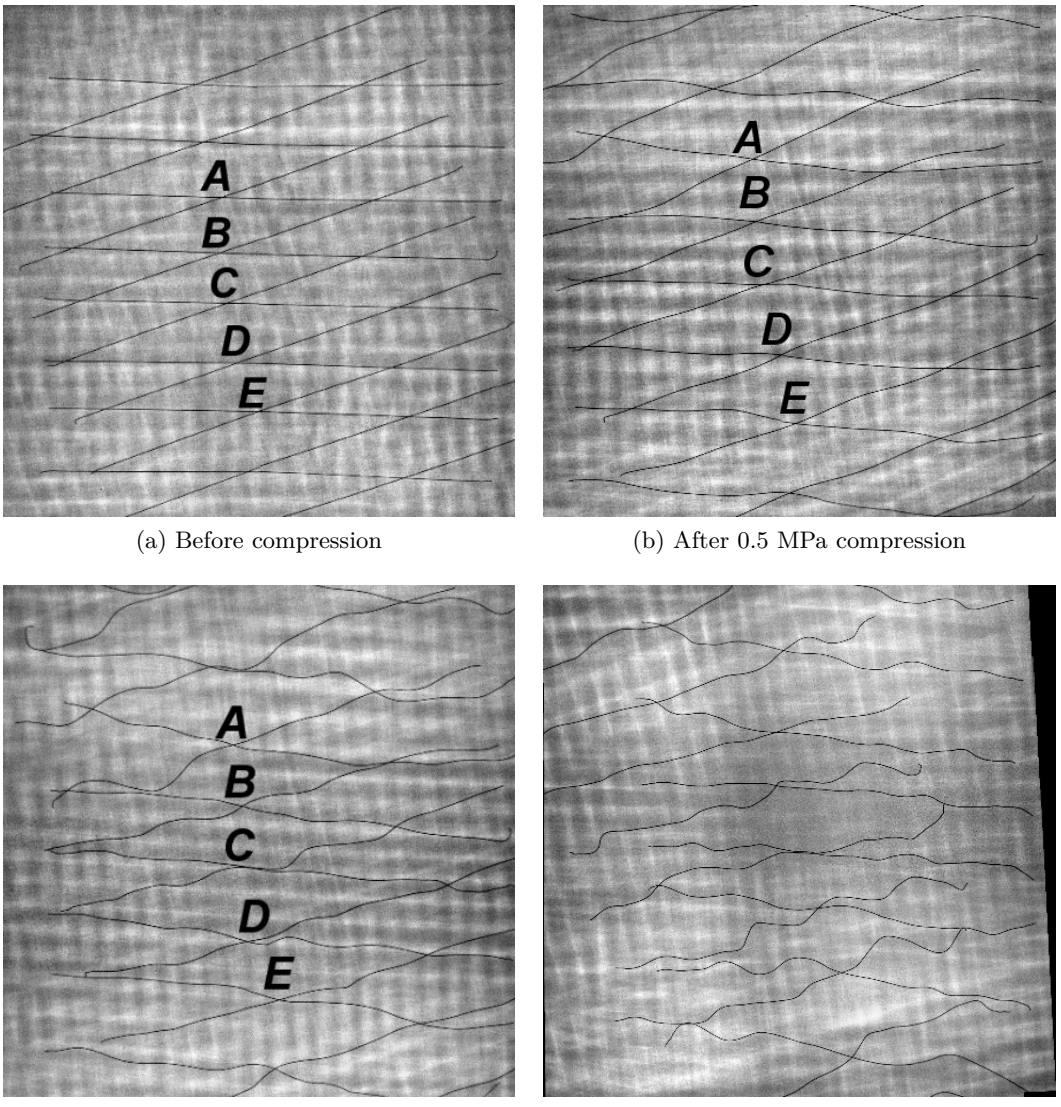

(a) Before compression

(b) After 0.5 MPa compression

(c) After 1 MPa compression

(d) After 1.5 MPa compression

Figure 1.17 – CT-scan of [0/20/0] stack of Vizilon™ SB63G1 prepreg.

It can be seen from Table 1.11 that the fibres have rotated and there is a overall rotation of 4.56° on average in the clockwise direction under a 0.5 MPa compression. The bending of the fibres due to the flow of resin towards the edges of the sample under 0.5 MPa compression can be seen in Figure 1.17b. It can be noticed in Figure 1.17c that the fibres have been displaced particularly at the edges of the sample. Wrinkles of the copper tracers can be seen due to crimp of the woven fabric. The orientation of fibres under 1.5 MPa compression (Figure 1.17d) is not measured due to the state of the specimen after compression.

	Angle [°]			
Label	Initial	0.5 MPa	1 MPa	1.5 MPa
A	160	151.7	157.8	-
B	160	156.2	160.5	-
C	158.6	156.6	160.8	-
D	159.5	155.5	161.7	-
E	158.4	153.7	157.5	-

Table 1.11 – Initial and after compression angles for the [0/20/0] stack of Vizilon™ SB63G1 prepreg.

1.3.5.4 Compression of a [0/45/0] stack of Vizilon™ SB63G1 prepreg

An assembly of 45° oriented ply in between two 0° plies of Vizilon™ SB63G1 was subjected to compression at a pressure of 0.5, 1 and 1.5 MPa at the melting temperature. Measured rotation values are presented in Table 1.12.CT-scans are presented in Figure 1.18.

	Angle [°]			
Label	Initial	0.5 MPa	1 MPa	1.5 MPa
A	45	44.1	49.9	48.1
B	45	41.8	37.6	39.6
C	45	41.5	45.7	44.7
D	45	47.9	49.9	49.1
E	45	41.2	41.2	42.3

Table 1.12 – Initial and after compression angles for the [0/45/0] stack of Vizilon™ SB63G1 prepreg.

It can be noticed from Table 1.12 that the fibres have rotated and that there is an overall 2.86° rotation of fibres on average in the clock-wise direction. Figures 1.18b, 1.18c and 1.18d shows the displacement of the fibres, which affected the orientation of the fibres due to the resin flow towards the edges of the sample when subjected to compression.

Displacement of the fibres can be seen in Figures 1.15, 1.16, 1.17 and 1.18, which is more important than in a prepreg with higher fibre fraction, as considered in previous experiments. This illustrates that the resin content plays a vital role in maintaining the orientation of the fibres.

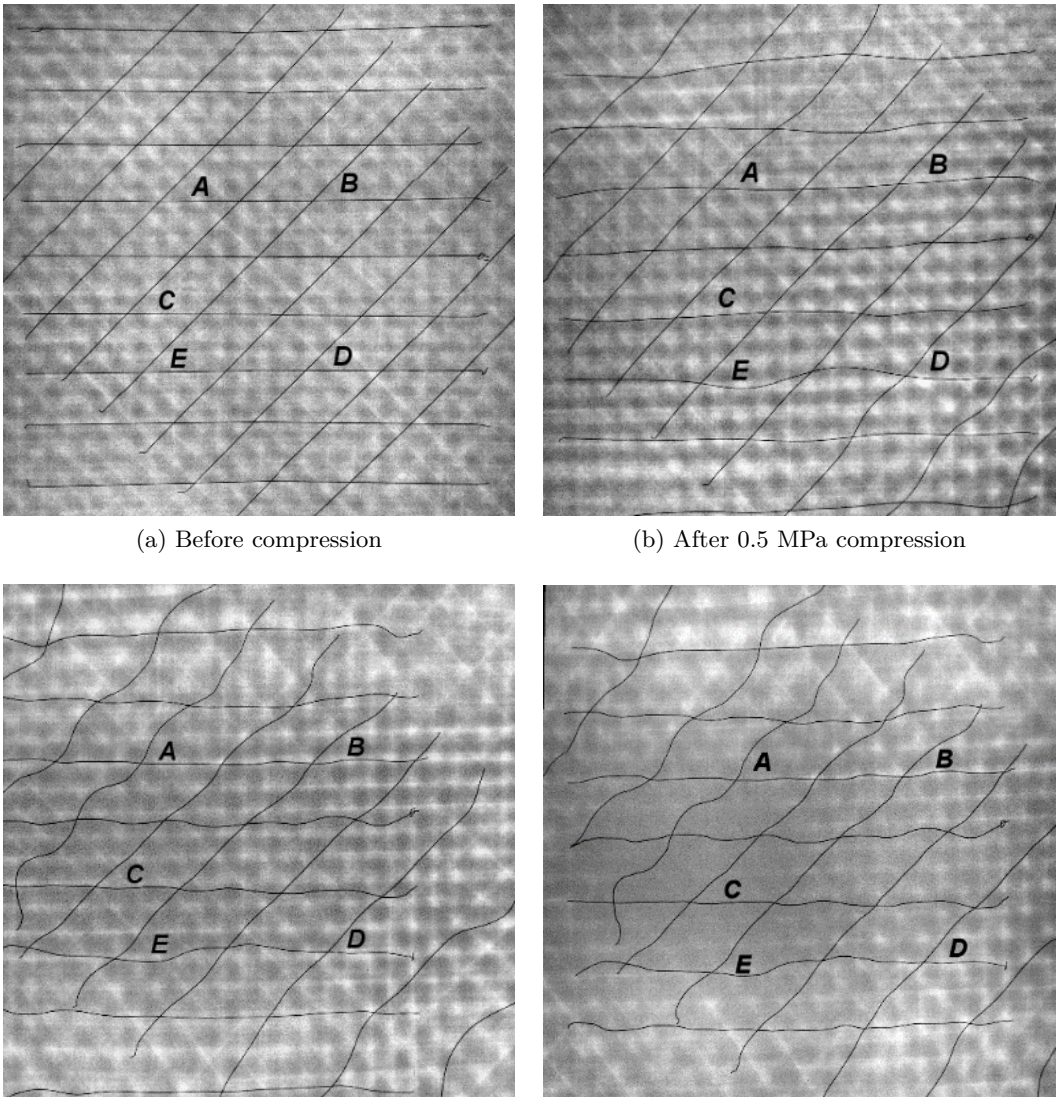

(a) Before compression

(b) After 0.5 MPa compression

(c) After 1 MPa compression

(d) After 1.5 MPa compression

Figure 1.18 – CT-scan of [0/45/0] stack of Vizilon™ SB63G1 prepreg.

1.3.6 Conclusion

In this chapter experiments were carried out of UD and woven prepregs. The phenomenon were observed with the use of copper wires that acted as kinematic tracers in the CT scanner.

The following important conclusions are drawn from the experimental campaign on the unidirectional prepregs:

- There is always a pure resin layer between the plies in prepreg laminates.
- A reaction stress develops in fibres to prevent the flow along their direction.
- There is a complex flow at the plies interface.
- The kinematics of the copper tracers differs from the kinematics of the plies, although the tracers are a good indicator of the movement of the plies.

- The observed phenomena that the unidirectional model should be able to retrieve are:
  - Squeeze flow kinematics perpendicular to the fibre direction.
  - Inextensibility in the fibre direction.
  - No bleeding of resin.
  - Rotation and in-plane bending of the plies.

The following important conclusions are drawn from the experimental campaign on the woven prepregs:

- Initial orientation has an influence on the amplitude and the direction of the solid body rotation induced by the flow towards the edges of the sample under compression.
- Specimen size has an influence as larger plies will be subjected to greater viscous forces.
- Structure of the woven fabric has an influence, probably due to the asymmetric flow of polymer in the unbalanced prepreg being the origin of the solid body rotation.
- Fibre fraction has an influence as the excess resin content is responsible for higher displacement of the fibres due to a less constrained fluid.

Chapter 2

2D Transversely Isotropic Fluid model

This Chapter presents the formulation of the 2D Transversely Isotropic Fluid (TIF) model, the numerical simulation and the results.

Section 2.1 focuses on the general presentation of the model, the equations to solve, the added kinematic constraints, the constitutive law and the explicit update scheme.

Section 2.2 focuses on the computation of the weak form, the choice of shape functions and the elements used.

Section 2.3 presents the results of the simulation conducted to verify that the model give the expected result and is stable.

Contents

2.1 Presentation of the model

Different levels of analysis are possible, including the fibre and tow levels, ply-by-ply analysis in which the prepreg plies are modelled as distinct bodies or composite models that use effective properties. Here the ply-by-ply analysis is chosen because of the occurrence of large relative displacement of plies allowed by the resin interply. In addition, one focus of the thesis is on fibre-aligned prepreg where tows are undistinguishable. To model the behaviour of the thermoplastic laminates reinforced with continuous fibres in the thermoforming process, the resin and fibre are macroscopically regarded as a single homogenized anisotropic material. According to the occurence of the special situations in the forming for discontinuous viscous prepregs observed and discussed in Chapter 1, a viscous flow modelling approach is chosen here.

The very first viscous model was proposed by Rogers who modelled the behaviour of one continuous layer of impregnated UD array of fibre as a viscous incompressible fluid and named that model as "ideal fibre reinforced fluid" [2]. It has been developed on the basis of the elastic ideal fibre reinforced model proposed by Pipkin [3] and Spencer [4]. The melted resin is considered a viscous incompressible fluid, and the presence of the fibres is taken into account by adding an inextensibility constraint in the fibre direction, leading to an homogenized viscous fluid, transversely isotropic, incompressible and inextensible. It is a model based on physical properties such as fibre volume fraction and resin viscosity. It is attractive because it reduces the need for extensive characterization campaign. Based on that theory, Ó. Brádaigh et al [5] modelled the drape behaviour of a multi-layered thermoplastic. 2D elements were stacked through the thickness of the sheet, each ply represented by a row of elements. The constitutive relation in each ply was based on the "ideal fibre reinforced fluid" proposed earlier by Rogers [2]. A layer of contact elements was placed between the ply elements because experiments demonstrated the presence of a resin rich layer between the individual plies during forming, justifying a viscous contact behaviour [1], [6]. Fibres were assumed inextensible, preventing the deformation of the fluid in the fibre directions. The fluid was also assumed incompressible. In the plane stress situation, the model simplifies to a single parameter model and is able to simulate the draping behaviour of the material. Inextensibility of fibres means that the multi-layered thermoplastic composite deform entirely by shearing. In addition perfect interply slip relieves the bending stresses. The elastic behaviour of the fabric itself was not incorporated into the material models. Therefore, process-induced fibre stresses are unaccounted for in these models.

Spencer and co-workers extended later that model to the case of a bidirectional fabric "Fabric Reinforced Fluid" (FRF) [7]. He modelled the behaviour of one layer of impregnated woven fabrics as a viscous fluid. Similarly, Spencer extended that model to a visco-plasticity model for draping fabric-reinforced composites [8] and non-Newtonian transversely isotropic fluids [9].

Later, Lamers and co-workers extended the FRF model with elastic components that allows the model to incorporate fibre stresses and an elastic fabric shear response in drape predictions [10], [11]. A finite stiffness was assigned to the fibres, that way it was not necessary to use Lagrange multipliers in the FE calculations. The total stress is the sum of the elastic stress contribution and the extra viscous stress contribution. The elastic and viscous contributions to the stress are solved separately, allowing a description of the complex fabric behaviour such as the phenomenon of locking. The material model was developed, based on a continuum description of motion and implemented into an implicit updated Lagrangian FE package DIEKA. The material model was implemented for linear triangular membrane elements with one integration point. The incremental

strains are obtained from the nodal displacements at each step using the shape functions of the element. Contact between both sides of the composite and the mould walls was modelled using six node wedge contact elements. The forming simulation is displacement controlled by moving the top mould towards the bottom mould in small steps, using a fixed time increment per step. For each displacement step, the system is solved implicitly using a predictor-corrector scheme. Later a multi-layer model that incorporates interlaminar shear behaviour was developed. The model was also extended to address the multi-layered composites. As individual plies in the material must slide with respect to each other and deform individually, a simple viscous slip law expressed in terms of the velocity differences between adjacent plies was incorporated. The results of the developed multi-layer FE model and the FE model with multiple membrane elements through the thickness of the sheet were compared and found to be similar. However, the multi-layer model was less CPU intensive, by a factor of seven for the double dome geometry. Unrealistically high fibre stresses were predicted. The authors recommended further research on the effects of fibre straightening, fibre slip and interlaminar shear behaviour of these composites. Later, a new multi-layer element has been developed by Ten Thije et al to address the forming of woven prepregs [12]. The out-of-plane deformations are linear, while the in-plane deformations are of a quadratic form. This results in an element that remains planar during forming. A higher order in-plane displacement field was introduced to avoid intra-ply shear locking. Intra-ply shear locking occurs at shear angles far below the fabrics locking angle and leads to overestimation of fibre stress, force and stiffness and often leads to spurious wrinkles in 3D simulations. The FE package Aniform was developed on the basis of the Lamers and Ten Thije works [13].

The previous works were dedicated to the forming of continuous prepregs where they show that the forming of the multi-layered composites depend on the lubrication of the prepreg plies. Friction transfers the external loads into the prepreg plies and can cause wrinkling or fibre buckling in internal plies or in the laminate as a whole [14]. However this model cannot reflect the complex lubrication in the inter-ply areas in the case of discontinuous viscous prepregs where additional mechanics occur. A thinner description of the plies interface is mandatory to really capture phenomena the complex rheology revealed in Chapter 1.

The following general assumptions are used in the modified TIF model presented in the sequel:

- Acceleration effects are neglected, i.e. $Re = 0$.
- In the plies:
  - No distinction is made between fibres and matrix in any other way in the continuum model.
  - Fibres introduce an inextensible direction in the composite plies.
  - Fibres convect with the melted polymer during the flow.
  - As a result, the composite ply is modelled as a homogenized linear viscous fluid reinforced by inextensible fibres.
  - The strain-rate dependency is not included.
- A linear viscous fluid is inserted to model the interface when considering a stack of plies.

As the rate of deformation during the process is supposed slow enough, non-linear dynamical effects are not taken into account. Based on that hypothesis, the homogenized fluid is considered in a succession of quasi-static states. Therefore the simulation consists in computing the instantaneous velocity, then updating the geometry of the stack of plies and the fibre orientation before going on to the next time step.

2.1.1 Equilibrium of the fluid

As in any mechanical problem the first equation to be solved is equilibrium:

$$\underline{\mathrm{div}}\left(\underline{\underline{\sigma}}\right) + \underline{f}_b = \underline{0}, \tag{2.1}$$

with $\underline{\underline{\sigma}}$ the stress tensor and $\underline{f}_b$ the body forces. As the problem is quasi-static this equation will be solved at each time step to compute the instantaneous velocity, pressure and fibre tension.

2.1.2 2D constitutive model of viscous uniaxial composite

Rogers [2] proposed the following constitutive model for unidirectional viscous composite:

$$\underline{\underline{\sigma}} = \underline{\underline{\underline{D}}} : \underline{\underline{\dot{\varepsilon}}} - P\underline{\underline{1}} + T\underline{\underline{A}}, \tag{2.2}$$

with $\underline{\underline{\dot{\varepsilon}}}$ the rate of strain tensor:

$$\underline{\underline{\dot{\varepsilon}}} = \frac{1}{2}\left(\frac{\partial \underline{V}}{\partial \underline{x}}^T + \frac{\partial \underline{V}}{\partial \underline{x}^T}\right), \tag{2.3}$$

$\underline{V}$ the velocity, P the pressure, T the tension in the fibres, $\underline{a}$ the unitary fibre orientation:

$$\underline{a} = \begin{bmatrix} \cos(\theta) \\ \sin(\theta) \\ 0 \end{bmatrix}, \tag{2.4}$$

with θ the angle between the fibres and the horizontal axis and $\underline{\underline{\underline{D}}}$ the transversely isotropic viscosity tensor:

$$\underline{\underline{\underline{D}}} = 2\eta_T \underline{\underline{\underline{1}}} + 2\left(\eta_L - \eta_T\right)\underline{\underline{A}} \otimes \underline{\underline{A}}, \tag{2.5}$$

with η_L the longitudinal viscosity, η_T the transverse viscosity and $\underline{\underline{A}}$ the fibre orientation tensor:

$$\underline{\underline{A}} = \underline{a} \otimes \underline{a}. \tag{2.6}$$

Equation (2.5) introduces a fluid of viscosity η_L along the fibre direction and η_T in the other principal directions, corresponding to the desired behaviour for the TIF model.

The constitutive equation (2.2) is particularized for 2D with plane stress hypothesis in 2.1.2.1, with plane strain hypothesis in 2.1.2.2. It will be modified for the 3D model in Chapter 3.

2.1.2.1 2D plane stress

A single composite ply has usually a small thickness compared to its in-plane dimensions, meaning that its off-plane stiffness is very small compared to the stiffness in the plane direction. This particularity is consistent with the plane stress hypothesis. The 2D plane stress behaviour law of a reinforced Newtonian fluid was developed by Rogers in [2]. The material is as presented in 2.1.2 with in addition the plane stress hypothesis. This leads to the following constitutive law:

$$\begin{bmatrix} \sigma_{xx} \\ \sigma_{yy} \\ \sqrt{2}\,\sigma_{xy} \end{bmatrix} = \begin{bmatrix} D_{11} & D_{12} & D_{13} \\ D_{12} & D_{22} & D_{23} \\ D_{13} & D_{23} & D_{33} \end{bmatrix} \begin{bmatrix} \dot{\varepsilon}_{xx} \\ \dot{\varepsilon}_{yy} \\ \sqrt{2}\,\dot{\varepsilon}_{xy} \end{bmatrix} + \begin{bmatrix} T\cos^2(\theta) \\ T\sin^2(\theta) \\ T\cos(\theta)\,\sin(\theta) \end{bmatrix} - \begin{bmatrix} P \\ P \\ 0 \end{bmatrix} \tag{2.7}$$

Voigt notation is used in order to simplify the expressions. The terms appearing in the constitutive viscous matrix are:

$$\begin{cases} D_{11} &= 4\left[\eta_T\left(1-\cos^2(\theta)\right)+\eta_L\cos^2(\theta)\right] \\ D_{22} &= 4\left[\eta_T\left(1-\sin^2(\theta)\right)+\eta_L\sin^2(\theta)\right] \\ D_{33} &= \eta_L \\ D_{12} &= 2\,\eta_T \\ D_{23} &= 2\sqrt{2}\,(\eta_L-\eta_T)\,\cos(\theta)\,\sin(\theta) \\ D_{13} &= 2\sqrt{2}\,(\eta_L-\eta_T)\,\cos(\theta)\,\sin(\theta) \end{cases} \tag{2.8}$$

with η_L the longitudinal viscosity, η_T the transverse viscosity and θ the fibre orientation.

In this case the problem is solved only in the plane, the out-of-plane velocity being calculated on the in-plane velocity through the rate of strain components:

$$\dot{\varepsilon}_{zz} = -\left(\dot{\varepsilon}_{xx}+\dot{\varepsilon}_{yy}\right). \tag{2.9}$$

2.1.2.2 2D plane strain

A single composite ply can be modelled using the plane stress hypothesis as explained in 2.1.2.1. However stacking several composite plies greatly increases the out-of-plane stiffness therefore violating the plane stress hypothesis. In this condition the plane strain hypothesis is better suited to describe the behaviour of a stack of plies. The material law is as presented in 2.1.2, where the plane strain hypothesis must be taken into consideration. This leads to the constitutive law (2.10).

$$\begin{bmatrix} \sigma_{xx} \\ \sigma_{yy} \\ \sqrt{2}\,\sigma_{xy} \end{bmatrix} = \begin{bmatrix} D_{11} & 0 & D_{13} \\ 0 & D_{22} & D_{23} \\ D_{13} & D_{23} & D_{33} \end{bmatrix} \begin{bmatrix} \dot{\varepsilon}_{xx} \\ \dot{\varepsilon}_{yy} \\ \sqrt{2}\,\dot{\varepsilon}_{xy} \end{bmatrix} + \begin{bmatrix} T\cos^2(\theta) \\ T\sin^2(\theta) \\ T\cos(\theta)\,.\sin(\theta) \end{bmatrix} - \begin{bmatrix} P \\ P \\ 0 \end{bmatrix} \tag{2.10}$$

Voigt notation is also used here in order to simplify the expressions. The terms in the constitutive viscous matrix changed from equation (2.8) and are detailed in equation (2.11).

$$\begin{cases} D_{11} &= 2\left[\eta_T\left(1-\cos^2(\theta)\right)+\eta_L\cos^2(\theta)\right] \\ D_{22} &= 2\left[\eta_T\left(1-\sin^2(\theta)\right)+\eta_L\sin^2(\theta)\right] \\ D_{33} &= \eta_T \\ D_{23} &= 2\sqrt{2}\,(\eta_L-\eta_T)\,\cos(\theta)\,\sin(\theta) \\ D_{13} &= 2\sqrt{2}\,(\eta_L-\eta_T)\,\cos(\theta)\,\sin(\theta) \end{cases} \tag{2.11}$$

with η_L the longitudinal viscosity, η_T the transverse viscosity and θ the fibre orientation.

In this case the problem is solved only in the plane, the out-of-plane velocity being equal to zero, the velocity verifies $V_z = 0$.

2.1.3 Kinematic constraints

The modelled fibre-aligned prepreg material has a viscous behaviour coupled with an incompressibility and an inextensibility in the fibre direction, as discussed by Rogers [2]. The incompressibility and the inextensibility in the fibre direction are respectively modelled as:

$$\underline{\underline{\dot{\varepsilon}}} : \underline{\underline{1}} = 0, \tag{2.12}$$

with $\underline{\underline{1}}$ the identity matrix, and

$$\underline{\underline{\dot{\varepsilon}}} : \underline{\underline{A}} = 0. \tag{2.13}$$

2.1.4 Explicit update

The resolution algorithm consists of considering the fluid in a succession of quasi-static states, and to update the geometry and the material properties before proceeding to the next timestep.

2.1.4.1 Mesh position

Once the velocity is known, the position of the mesh can be updated using an explicit scheme:

$$\underline{x}_{i+1} = \underline{x}_i + \Delta t \, \underline{v}_i, \tag{2.14}$$

with $\underline{x}$ the nodes' position and Δt the timestep.

The inextensibility constraint being enforced on the instantaneous velocity, it is not satisfied anymore as soon as the mesh is modified. Therefore, a special attention is paid on the quality of the computation due to the use of an explicit scheme instead of an implicit one, and the stability of the method must be verified. It also constraints the number of time steps in order to keep numerical stability.

2.1.4.2 Fibre reorientation

As the fibres move with the fluid, their orientation is convected by the flow in the ply. Considering the inextensibility of the fibres, the evolution equation of $\underline{a}$ is:

$$\frac{D\underline{a}}{Dt} = (\underline{\nabla} \, \underline{V}) \, \underline{a}, \tag{2.15}$$

with $\underline{\nabla} \, \underline{V}$ the velocity gradient, as discussed by Rogers [2].

Injecting (2.4) into (2.15) and expressing $\underline{\dot{a}}$ and $\underline{a}$ in terms of $\dot{\theta}$ and θ leads to

$$\begin{cases} -\dot{\theta} \sin\theta = \dfrac{\partial v_x}{\partial x} \cos\theta + \dfrac{\partial v_x}{\partial y} \sin\theta, & \text{(2.16a)} \\ \dot{\theta} \cos\theta = \dfrac{\partial v_y}{\partial x} \cos\theta + \dfrac{\partial v_y}{\partial y} \sin\theta, & \text{(2.16b)} \end{cases}$$

and combining equations (2.16a) and (2.16b) leads to the evolution equation of θ:

$$\begin{aligned} \dot{\theta} = \Bigg(\cos^2\theta \left[\left(\frac{\partial v_x}{\partial x} \right)^2 + \left(\frac{\partial v_y}{\partial x} \right)^2 \right] + \sin^2\theta \left[\left(\frac{\partial v_x}{\partial y} \right)^2 + \left(\frac{\partial v_y}{\partial y} \right)^2 \right] \\ + 2 \cos\theta \sin\theta \frac{\partial v_x}{\partial x} \frac{\partial v_x}{\partial y} \frac{\partial v_y}{\partial x} \frac{\partial v_y}{\partial y} \Bigg). \end{aligned} \tag{2.17}$$

Equation (2.15) can be injected into an explicit update scheme in order to obtain the evolution equation of the fibre orientation:

$$\theta_{n+1} = \theta_n + \Delta t \left[\left(\frac{\partial v_y}{\partial y} - \frac{\partial v_x}{\partial x} \right) \cos\theta \sin\theta + \frac{\partial v_x}{\partial y} \cos^2\theta + \frac{\partial v_y}{\partial x} \sin^2\theta \right] \tag{2.18}$$

2.2 Numerical simulation

The Finite Element Method (FEM) is used to compute an approximate solution to the equilibrium under constraints presented in section 2.1. Ó'. Brádaigh [15] used a mixed penalty method to compute the velocity and then reconstruct the tension in the fibres when needed. In this thesis, an accurate prediction of the tension field is required as it is a quantity of interest, a Lagrangian multiplier method is used to obtain the velocity and the tension in a single step and to avoid the dependency of the solution on the value of a penalty parameter.

2.2.1 Weak form

The calculation of the weak formulation of the governing equations is similar to the one developed by Ó. Brádaigh in [15]. The dissipated power is expressed as

$$E_k = \frac{1}{2}\int_\Omega \underline{\underline{\dot{\varepsilon}}} : \underline{\underline{\underline{\underline{D}}}} : \underline{\underline{\dot{\varepsilon}}} \mathrm{d}\Omega \tag{2.19}$$

and the power of the external forces is expressed as

$$W = \int_\Omega \underline{V}\,\underline{f}_b \mathrm{d}\Omega + \int_\Gamma \underline{V}\,\underline{f}_s \mathrm{d}\Gamma, \tag{2.20}$$

with $\underline{f}_b$ the body forces and $\underline{f}_s$ the surface forces.

To enforce the constraints Lagrange multipliers are used. A Lagrange multiplier P is associated with the incompressibility:

$$P\left(\underline{\underline{\dot{\varepsilon}}} : \underline{\underline{1}}\right) = 0, \tag{2.21}$$

with p the pressure and a Lagrange multiplier T is associated with the inextensibility:

$$T\left(\underline{\underline{\dot{\varepsilon}}} : \underline{\underline{\underline{A}}}\right) = 0, \tag{2.22}$$

with t the fibre tension.

The principle of stationarity gives:

$$\begin{aligned}\delta E_k = \delta\Bigg\{\frac{1}{2}\int_\Omega \underline{\underline{\dot{\varepsilon}}} : \underline{\underline{\underline{\underline{D}}}} : \underline{\underline{\dot{\varepsilon}}} \mathrm{d}\Omega + \int_\Omega P\left(\underline{\underline{\dot{\varepsilon}}} : \underline{\underline{1}}\right)\mathrm{d}\Omega + \int_\Omega T\left(\underline{\underline{\dot{\varepsilon}}} : \underline{\underline{\underline{A}}}\right)\mathrm{d}\Omega \\ - \int_\Omega \underline{V}\,\underline{f}_b \mathrm{d}\Omega - \int_\Gamma \underline{V}\,\underline{f}_s \mathrm{d}\Gamma\Bigg\} = 0.\end{aligned} \tag{2.23}$$

Taking all possible variations of Equation (2.23) yields:

$$\begin{cases} \delta\underline{V}^T \to \displaystyle\int_\Omega \delta\underline{V}^T\left[\underline{\nabla}^{sT}\left(\underline{\underline{\underline{\underline{D}}}} : \underline{\underline{\dot{\varepsilon}}}\right) + \underline{\underline{A}}\,\underline{\nabla} T + \underline{\nabla} P - \underline{f}_b\right]\mathrm{d}\Omega - \int_\Gamma \delta\underline{V}^T\underline{f}_s \mathrm{d}\Gamma = 0 & \text{(2.24a)} \\ \delta P \to \displaystyle\int_\Omega \delta P\left(\underline{\underline{\dot{\varepsilon}}} : \underline{\underline{1}}\right)\mathrm{d}\Omega = 0 & \text{(2.24b)} \\ \delta T \to \displaystyle\int_\Omega \delta T\left(\underline{\underline{\dot{\varepsilon}}} : \underline{\underline{\underline{A}}}\right)\mathrm{d}\Omega = 0 & \text{(2.24c)} \end{cases}$$

2.2.2 Discretisation

The velocity, the fibre tension and the pressure are discretized using different interpolation functions. This allows to use a higher order of interpolation functions for the velocity than for the fibre tension and the pressure, avoiding numerical issues during the solving of the system. This matter is addressed by Hughes in [16] and will be discussed in Section 2.2.3. This leads to the forms of the unknown presented in (2.25).

$$\begin{cases} \underline{V}(\underline{x}) \approx \tilde{\underline{V}}(\underline{x}) = \underline{\underline{N}}^V(\underline{x}) \ \hat{\underline{V}} & \delta\underline{V}(\underline{x}) \approx \delta\tilde{\underline{V}}(\underline{x}) = \underline{\underline{N}}^V(\underline{x}) \ \delta\hat{\underline{V}} \\ P(\underline{x}) \approx \tilde{P}(\underline{x}) = \underline{N}^P(\underline{x}) \cdot \hat{\underline{P}} & \delta P(\underline{x}) \approx \delta\tilde{P}(\underline{x}) = \underline{N}^P(\underline{x}) \cdot \delta\hat{\underline{P}} \\ T(\underline{x}) \approx \tilde{T}(\underline{x}) = \underline{N}^T(\underline{x}) \cdot \underline{\hat{T}} & \delta T(\underline{x}) \approx \delta\tilde{T}(\underline{x}) = \underline{N}^T(\underline{x}) \cdot \delta\underline{\hat{T}} \end{cases} \tag{2.25}$$

where $\underline{\underline{N}}^V$, $\underline{N}^P$ and $\underline{N}^T$ are the interpolation functions for the velocity, the pressure and the fibre tension respectively, $\tilde{\underline{V}}$, $\tilde{P}$ and $\tilde{T}$ the numerically approximated fields for the velocity, the pressure and the fibre tension respectively and $\hat{\underline{V}}$, $\hat{\underline{P}}$ and $\underline{\hat{T}}$ the nodal values of the velocity, the pressure and the fibre tension respectively.

Introducing these interpolations into equations (2.24a), (2.24b) and (2.24c), and noting that these equations must be verified for all $\delta\hat{\underline{V}}$, $\delta\hat{\underline{P}}$ and $\delta\underline{\hat{T}}$, the complete equations system is obtained as in (2.26). It is important to notice that the system (2.26) is typical of a saddle-point problem, a particular category much discussed in the literature, and will therefore require a special attention when solving with an iterative solver.

$$\begin{bmatrix} \underline{\underline{K}}^V & \underline{\underline{K}}^P & \underline{\underline{K}}^T \\ \left(\underline{\underline{K}}^P\right)^T & \underline{\underline{0}} & \underline{\underline{0}} \\ \left(\underline{\underline{K}}^T\right)^T & \underline{\underline{0}} & \underline{\underline{0}} \end{bmatrix} \begin{bmatrix} \hat{\underline{V}} \\ \hat{\underline{P}} \\ \underline{\hat{T}} \end{bmatrix} = \begin{bmatrix} \underline{f} \\ \underline{0} \\ \underline{0} \end{bmatrix} \tag{2.26}$$

$\underline{\underline{K}}^V$, $\underline{\underline{K}}^P$, $\underline{\underline{K}}^T$ and $\underline{f}$ are defined as:

$$\begin{cases} K_{ij}^V &= \int_\Omega \left(\underline{\underline{B}}_i^V\right)^T \underline{\underline{D}} \, \underline{\underline{B}}_j^V \mathrm{d}\Omega \\ K_{ij}^P &= \int_\Omega \left(\underline{\underline{B}}_i^V\right)^T \underline{N}_j^P \mathrm{d}\Omega \\ K_{ij}^T &= \int_\Omega \left(\underline{\underline{B}}_i^V\right)^T \underline{a} \, \underline{N}_i^T \mathrm{d}\Omega \\ f_i &= -\int_\Omega \left(\underline{N}_i^V\right)^T \underline{f}_b \mathrm{d}\Omega - \int_\Gamma \left(\underline{N}_i^V\right)^T \underline{f}_s \mathrm{d}\Gamma \end{cases}, \tag{2.27}$$

with $\underline{f}_b$ the body forces and $\underline{f}_s$ the surface forces.

2.2.3 Choice of shape functions

It is shown in [16] that the shape functions for velocity should be of a higher order than the shape functions for the lagrangian multiplier associated with the incompressibility constraint in order to avoid locking. This rule also applies to the inextensibility constraint. Quadratic or biquadratic shape functions are therefore used for interpolating the velocity whereas linear or bilinear shape functions are used for interpolating both the pressure and fibre tension.

It will be highlighted in Section 2.3 that the fibre tension should be sometimes discontinuous over elements and sometimes continuous. In the discontinuous fibre tension case a Q9-3 element is used while a Q9-4 element is used in the continuous fibre tension case. These elements are discussed in Section 2.2.3.1 for the Q9-3 element and in Section 2.2.3.2 for the Q9-4 element. More details about these elements and on their implementation can be found in [17], [18] and [19].

The stability of elements for problems of incompressible fluid has been discussed, and a mathematical stability criterion known as the Ladyzhenskaya-Babuška-Brezzi (LBB) condition was presented in [20], [21] and [22]. Although it was suggested that the tests used for the stability of elements in an incompressible problem may not suffice for the inextensible problem in [23], it is assumed that an element that verifies the LBB condition for a problem with incompressibility also verifies it when inextensibility is added.

2.2.3.1 Q9-3 element

The Q9-3 element contains 9 velocity nodes and 3 pressure/tension nodes as can be seen on Figure 2.1. It was demonstrated in [24] that this element verifies the LBB conditions for the incompressible problem.

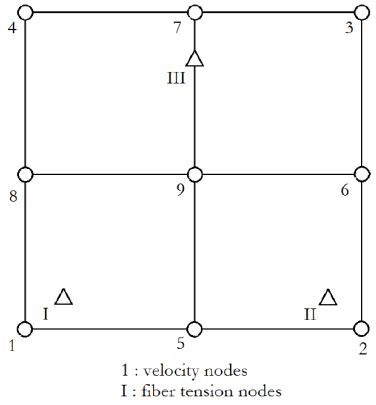

Figure 2.1 – Q9-3 element.

Velocity shape functions

Using a Q9 element the shape functions for the velocity are biquadratic. Using the node numeration shown in Figure 2.1 the shape functions and their derivatives detailed in Table 2.1 are obtained.

Node	N	$\partial N/\partial\xi$	$\partial N/\partial\eta$
1	$\xi\eta\left(\xi-1\right)\left(\eta-1\right)/4$	$\left(2\xi-1\right)\eta\left(\eta-1\right)/4$	$\xi\left(\xi-1\right)\left(2\eta-1\right)/4$
2	$\xi\eta\left(\xi+1\right)\left(\eta-1\right)/4$	$\left(2\xi+1\right)\eta\left(\eta-1\right)/4$	$\xi\left(\xi+1\right)\left(2\eta-1\right)/4$
3	$\xi\eta\left(\xi+1\right)\left(\eta+1\right)/4$	$\left(2\xi+1\right)\eta\left(\eta+1\right)/4$	$\xi\left(\xi+1\right)\left(2\eta+1\right)/4$
4	$\xi\eta\left(\xi-1\right)\left(\eta+1\right)/4$	$\left(2\xi-1\right)\eta\left(\eta+1\right)/4$	$\xi\left(\xi-1\right)\left(2\eta+1\right)/4$
5	$\left(1-\xi^2\right)\eta\left(\eta-1\right)/2$	$-\xi\eta\left(\eta-1\right)$	$\left(1-\xi^2\right)\left(2\eta-1\right)/2$
6	$\xi\left(\xi+1\right)\left(1-\eta^2\right)/2$	$\left(2\xi+1\right)\left(1-\eta^2\right)/2$	$-\xi\eta\left(\xi+1\right)$
7	$\left(1-\xi^2\right)\eta\left(\eta+1\right)/2$	$-\xi\eta\left(\eta+1\right)$	$\left(1-\xi^2\right)\left(2\eta+1\right)/2$
8	$\xi\left(\xi-1\right)\left(1-\eta^2\right)/2$	$\left(2\xi-1\right)\left(1-\eta^2\right)/2$	$-\xi\eta\left(\xi-1\right)$
9	$\left(1-\xi^2\right)\left(1-\eta^2\right)$	$-2\xi\left(1-\eta^2\right)$	$-2\eta\left(1-\xi^2\right)$

Table 2.1 – Shape functions and their derivatives for the Q9 element.

Pressure/tension shape functions

Using a Q9-3 element the shape functions for the pressure/tension are linear. The shape functions are not explicitly implemented, they are computed using a Vandermonde matrix detailed in (2.28). The values of the shape functions are then evaluated as presented in (2.29). The invertibility of the Vandermonde matrix is assured when $(\xi_i, \eta_i) \underset{i \neq j}{\neq} (\xi_j, \eta_j)$, therefore it will always be invertible considering that all Gauss points are distinct.

$$\underline{\underline{M}} = \begin{bmatrix} 1 & \xi_I & \eta_I \\ 1 & \xi_{II} & \eta_{II} \\ 1 & \xi_{III} & \eta_{III} \end{bmatrix} \tag{2.28}$$

with (ξ_I, η_I), (ξ_{II}, η_{II}) and (ξ_{III}, η_{III}) the coordinates of the pressure/tension nodes.

$$\underline{N} = \underline{\underline{M}}^{-1} \begin{bmatrix} 1 \\ \xi_{gauss} \\ \eta_{gauss} \end{bmatrix} \tag{2.29}$$

with $\underline{N} = [N_I \quad N_{II} \quad N_{III}]$ the vector containing the values of the pressure/tension shape functions at a given point, and $(\xi_{gauss}, \eta_{gauss})$ the coordinates of the point where the shape functions are sought, in most cases the Gauss points during the computation of the operators.

Gauss points

The Gauss points coordinates and weights are detailed in Table 2.2 for complete integration and in Table 2.3 for reduced integration.

Point	ξ	η	w
1	$-\sqrt{3/5}$	$-\sqrt{3/5}$	$25/81$
2	$\sqrt{3/5}$	$-\sqrt{3/5}$	$25/81$
3	$\sqrt{3/5}$	$\sqrt{3/5}$	$25/81$
4	$-\sqrt{3/5}$	$\sqrt{3/5}$	$25/81$
5	0	$-\sqrt{3/5}$	$40/81$
6	$\sqrt{3/5}$	0	$40/81$
7	0	$\sqrt{3/5}$	$40/81$
8	$-\sqrt{3/5}$	0	$40/81$
9	0	0	$64/81$

Table 2.2 – Gauss points coordinates and weights for complete integration.

Point	ξ	η	w
1	$-1/\sqrt{3}$	$-1/\sqrt{3}$	1
2	$1/\sqrt{3}$	$-1/\sqrt{3}$	1
3	$1/\sqrt{3}$	$1/\sqrt{3}$	1
4	$-1/\sqrt{3}$	$1/\sqrt{3}$	1

Table 2.3 – Gauss points coordinates and weights for reduced integration.

2.2.3.2 Q9-4 element

The Q9-4 element contains 9 velocity nodes and 4 pressure/tension nodes as can be seen on Figure 2.2. It was discussed in [25] that this element does not verify the LBB condition for the incompressible problem when a single element is used, but it verifies the LBB condition when at least four elements are used. It is therefore assumed that the use of at least four elements ensures the verification of the LBB condition for the incompressible and inextensible problem.

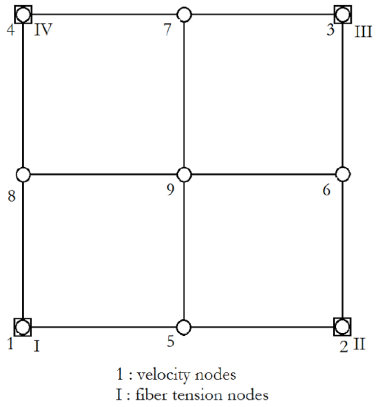

Figure 2.2 – Q9-4 element.

Velocity shape functions

Using the same shape functions than the Q9-3 element, the shape functions and their derivatives are the same as in Table 2.1.

Pressure/tension shape functions

The shape functions for the pressure/tension for a Q9-4 element are bilinear. Using the node numeration shown in Figure 2.2 the shape functions and their derivatives are detailed in Table 2.4

Node	N	$\partial N/\partial\xi$	$\partial N/\partial\eta$
1	$(1-\xi)(1-\eta)/4$	$-(1-\eta)/4$	$-(1-\xi)/4$
2	$(1+\xi)(1-\eta)/4$	$(1-\eta)/4$	$-(1+\xi)/4$
3	$(1+\xi)(1+\eta)/4$	$(1+\eta)/4$	$(1+\xi)/4$
4	$(1-\xi)(1+\eta)/4$	$-(1+\eta)/4$	$(1-\xi)/4$

Table 2.4 – Shape functions and their derivatives for the Q4 element.

2.3 Results

This section presents the results obtained with the 2D plane stress model. As the model considered is 2D, a single ply of composite was simulated in the plane or a stack of plies in the thickness. All computations were run with the longitudinal viscosity of the composite $\eta_L = 379\,\text{Pa.s}$ and transverse viscosity of the composite $\eta_T = 602\,\text{Pa.s}$, and if not stated otherwise results presented are instantaneous results for the first timestep. Those values were obtained considering the resin viscosity $\eta = 100\,\text{Pa.s}$ and a fibre volume fraction of 56.9%, using a semi-empirical model developed by Christensen in [26] that gives the homogenized transverse viscosity:

$$\eta_T = \left\{ \frac{1 + \alpha\left(v_f/F\right)}{\sqrt{\left[1 - \beta\left(v_f/F\right)\right]\left[1 - \left(v_f/F\right)\right]}} \right\}^3 \eta, \tag{2.30}$$

with η the resin viscosity, $\alpha = -0.1930$, $\beta = 0.5952$ and $F = \frac{\pi}{2\sqrt{3}}$, and the homogenized longitudinal viscosity:

$$\eta_L = \left\{ \frac{1 + \alpha\left(v_f/F\right)}{\sqrt{\left[1 - \beta\left(v_f/F\right)\right]\left[1 - \left(v_f/F\right)\right]}} \right\} \eta, \tag{2.31}$$

with $\alpha = 0.8730$ and $\beta = 0.8815$.

The transverse viscosity is higher than the longitudinal one as given by Christensen's model, contrary to what was seen in the bibliography. This means that making the fibres slide along them is easier than making them slide cross-wise, which is true when considering the sliding of one ply with respect to the other due to the fibres of one layer falling into the gaps of the other layer.

2.3.1 Traction along the fibre direction

In order to check that the kinematic constraints are correctly taken into account, the case of a traction along the fibre direction of a unidirectional composite was computed. The problem is represented in Figure 2.3. The size of the domain is 16 mm length and 10 mm wide. The expected results are a null velocity and pressure fields, a fibre tension equal to the applied force to prevent any displacement and no fibre reorientation.

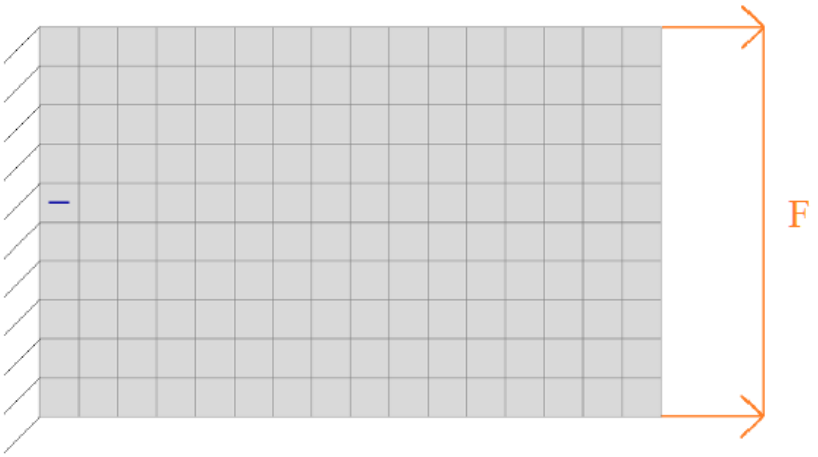

Figure 2.3 – Representation of the traction along the fibre direction problem. Velocity is imposed null on the left edge and a horizontal Neumann condition is imposed on the right edge, equal to 1N. The elements are represented, fibres are horizontally oriented.

2.3.1.1 Discontinuous fibre tension

The results obtained using a discontinuous interpolation for the fibre tension are presented in Figure 2.4.

As expected, there is no velocity, no fibre reorientation and the fibre tension is equal to the applied force in order to prevent any displacement, meaning that the model behaves well. It is interesting to notice that the profile of the fibre tension presents a very small instability (around 0.1%). This point will be discussed in Section 2.3.2.

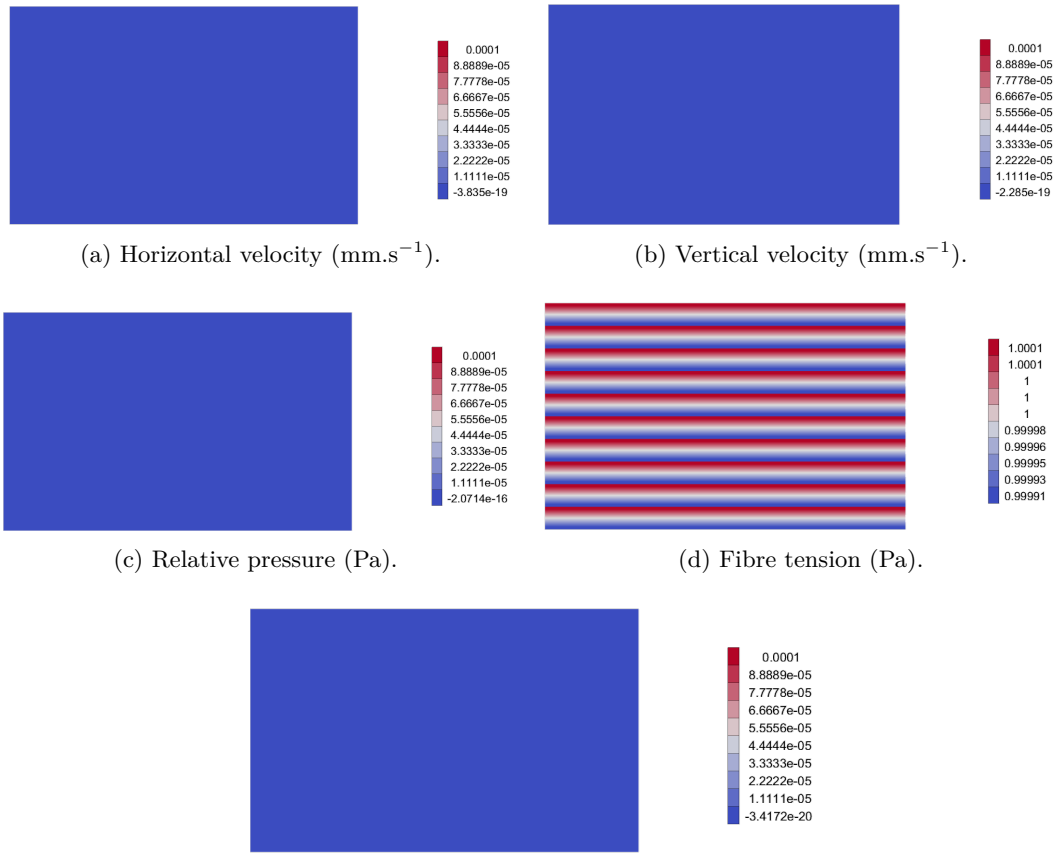

(a) Horizontal velocity ($mm.s^{-1}$).

(b) Vertical velocity ($mm.s^{-1}$).

(c) Relative pressure (Pa).

(d) Fibre tension (Pa).

(e) Fibre orientation (°).

Figure 2.4 – Results of the traction along the fibre direction using a discontinuous interpolation for the fibre tension.

2.3.1.2 Continuous fibre tension

The results obtained using a continuous interpolation for the fibre tension are presented in Figure 2.5.

The results obtained are very similar to those obtained using a discontinuous fibre tension, excepted the fibre tension, presented in Figure 2.5d, which is more stable and more accurate.

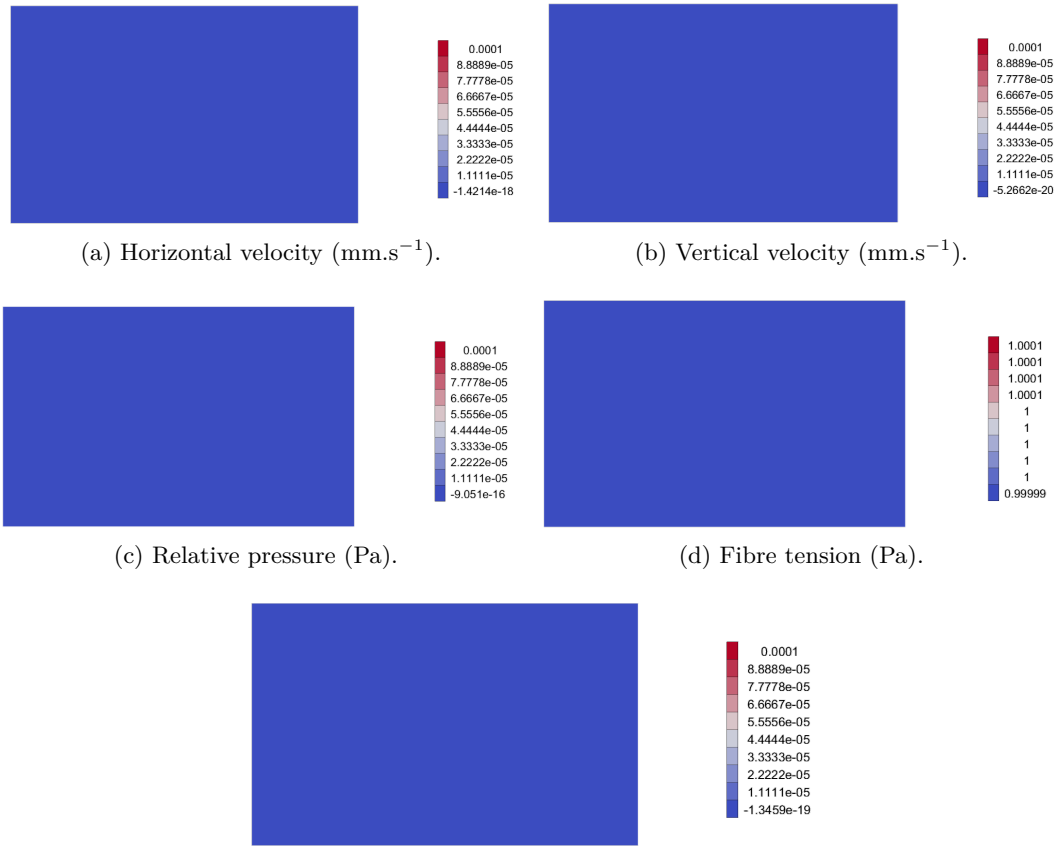

(a) Horizontal velocity ($mm.s^{-1}$).

(b) Vertical velocity ($mm.s^{-1}$).

(c) Relative pressure (Pa).

(d) Fibre tension (Pa).

(e) Fibre orientation (°).

Figure 2.5 – Results of the traction along the fibre direction using a continuous interpolation for the fibre tension.

2.3.2 In-plane shear

To check the validity of the fibre tension field, the case of a shear transverse the fibre direction is computed. The problem is presented in Figure 2.6. The size of the domain is 16 mm length and 10 mm wide. The expected results are a null horizontal velocity, a vertical velocity linear with respect to the horizontal coordinate, a pressure and tension fields reducing the rotation and maintaining the fibres parallel and an homogeneous fibre reorientation.

Results obtained with a discontinuous interpolation for the pressure and the fibre tension are presented in Section 2.3.2.1, and results obtained with a continuous interpolation for the pressure and the fibre tension are presented in Section 2.3.2.2. It will be shown that in this specific case a continuous interpolation for the pressure and the fibre tension yields better results.

Finally the results of the dynamic computation will be presented in Section 2.3.2.3, where it will be shown that the model is stable even though an explicit update scheme is used and there is no regularization.

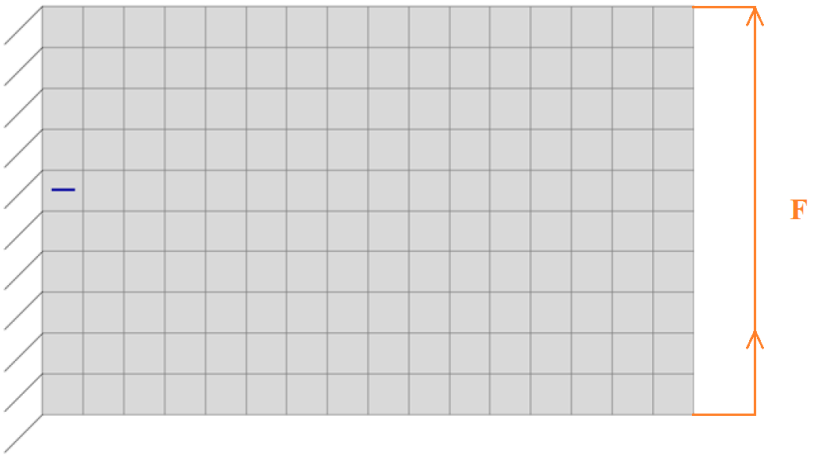

Figure 2.6 – Case of a transverse shear. Velocity is imposed null on the left edge of the mesh and a vertical Neumann condition is imposed on the right edge, equal to 100N. Elements are represented, fibres are placed horizontally.

2.3.2.1 Discontinuous fibre tension

The results obtained using a discontinuous interpolation for the fibre tension are presented in Figure 2.7.

As presented in Figures 2.7a and 2.7b there is no velocity in the horizontal direction and the velocity in the vertical direction is linear with respect to the horizontal coordinate. Although this result is satisfactory, Figure 2.7d shows that the fibre tension is not correct. This arises because a discontinuous interpolation for the fibre tension is used and as a consequence each element becomes inextensible. The same result would be obtained imposing a transverse shear condition on each element individually. It can also be seen in Figures 2.7c and 2.7e that the computed tension field is not realistic, therefore it can be concluded that the discontinuous interpolation for the pressure and fibre tension is not suitable.

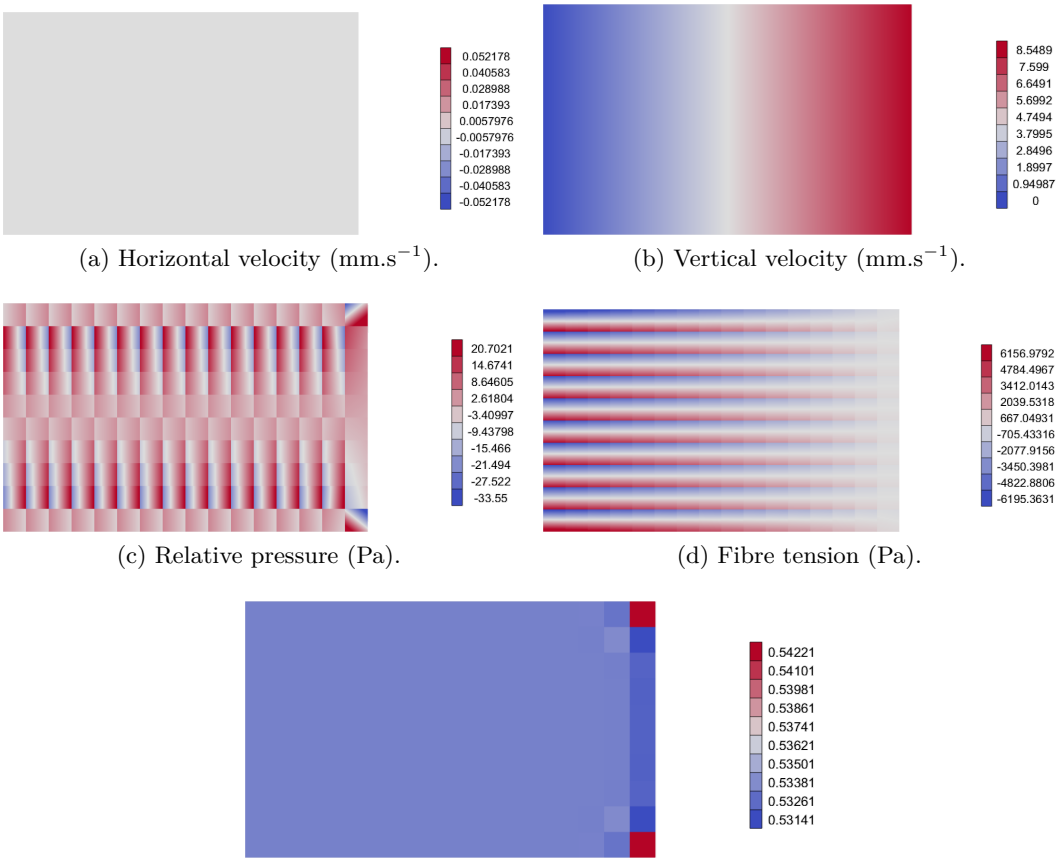

(a) Horizontal velocity ($mm.s^{-1}$).

(b) Vertical velocity ($mm.s^{-1}$).

(c) Relative pressure (Pa).

(d) Fibre tension (Pa).

(e) Fibre orientation (°).

Figure 2.7 – Results of the transverse shear using a discontinuous interpolation for the fibre tension.

2.3.2.2 Continuous fibre tension

Given the results obtained in Figure 2.7d, it is very clear that in this particular case the use of a discontinuous interpolation for the fibre tension yields non-physical results, as the fibre tension jumps from a negative value to a positive value of the same magnitude when crossing the element edge. For this reason, a continuous interpolation for the fibre tension was chosen.

The results obtained with a continuous interpolation for the fibre tension are presented in Figure 2.8.

As presented in Figures 2.8a and 2.8b the vertical velocity is still correct but the horizontal velocity is not zero everywhere. This is due to the fact that the fibre tension is now continuous, therefore the inextensibility is verified on average, leading to a horizontal velocity of zero on average. It is important to note that although this velocity field is not correct, the maximum horizontal velocity is 8% of the maximum vertical velocity, thus the error is acceptable.

As shown in Figure 2.8d, the fibre tension field is more realistic for a transverse shear loading. Furthermore, the results presented in Figures 2.8c and 2.8e are more physical than those presented in Figures 2.7c and 2.7e.

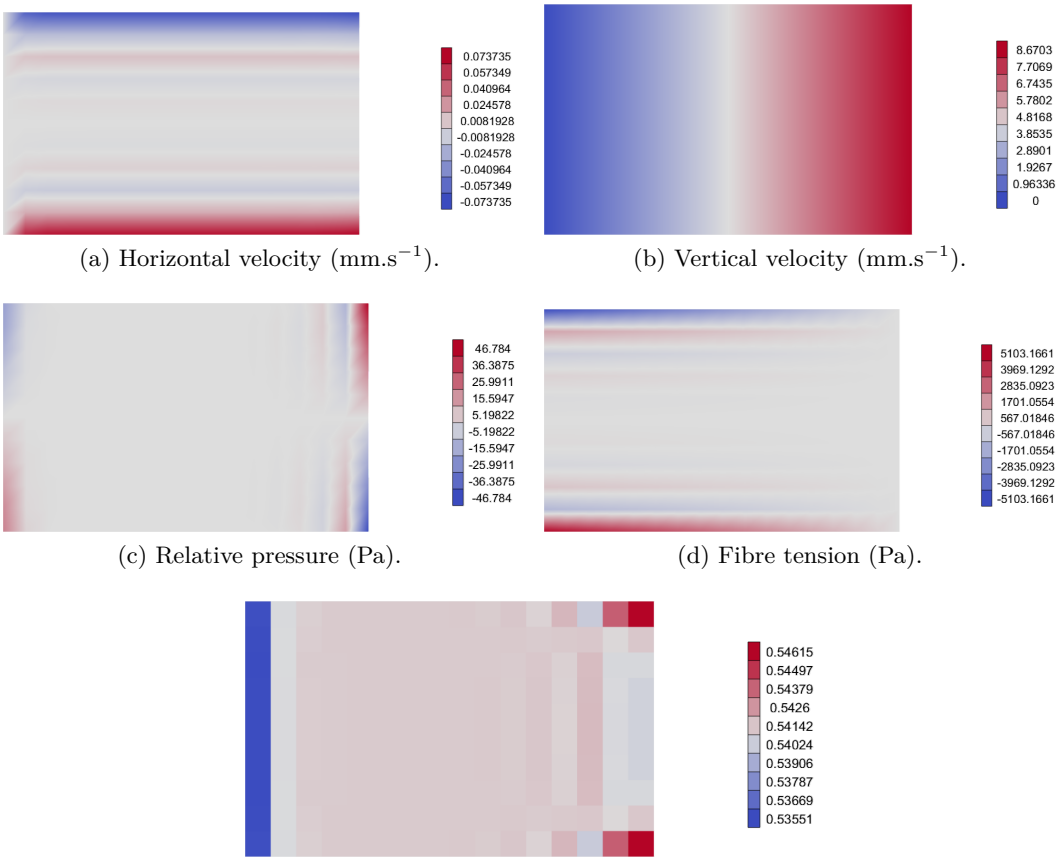

(a) Horizontal velocity ($mm.s^{-1}$).

(b) Vertical velocity ($mm.s^{-1}$).

(c) Relative pressure (Pa).

(d) Fibre tension (Pa).

(e) Fibre orientation (°).

Figure 2.8 – Results of the transverse shear using a continuous interpolation for the fibre tension.

2.3.2.3 Dynamic results

The results obtained with a dynamic simulation are presented in this section. Continuous interpolation was used for the pressure and the fibre tension, simulation time is $t_{max} = 10$s and the timestep is $\delta t = 0.5$s. Figure 2.9 presents the horizontal velocity, Figure 2.10 the vertical velocity, Figure 2.11 the pressure, Figure 2.12 the fibre tension and Figure 2.13 the fibre orientation at $t = 2.5$s, $t = 5$s, $t = 7.5$s and $t = 10$s.

In the early stages of the computation the horizontal velocity is nearly zero everywhere. When the time increases, the fibres are reoriented and the direction of the inextensibility changes. Therefore the inextensibility is no longer in the horizontal direction but in a linear combination of the horizontal and the vertical direction. When this happens the horizontal velocity value starts increasing.

As expected fibres are reoriented homogeneously during the deformation. There is a small numerical variation near the boundary conditions, due to the fact that the orientation is computed with the velocity gradient which is numerically unstable, especially around Dirichlet boundary conditions.

As can be seen in Figures 2.9 to 2.13 the results are numerically stable even though an explicit update scheme is used.

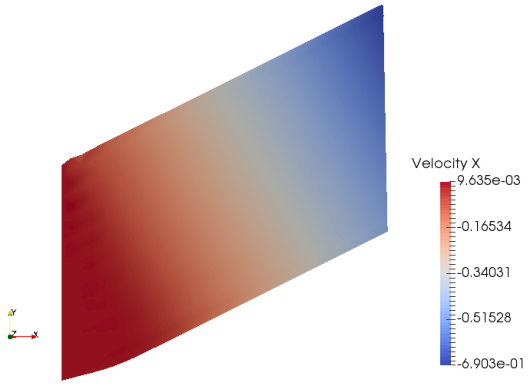

(a) Horizontal velocity (mm.s^{-1}) at 2.5s (5^{th} timestep).

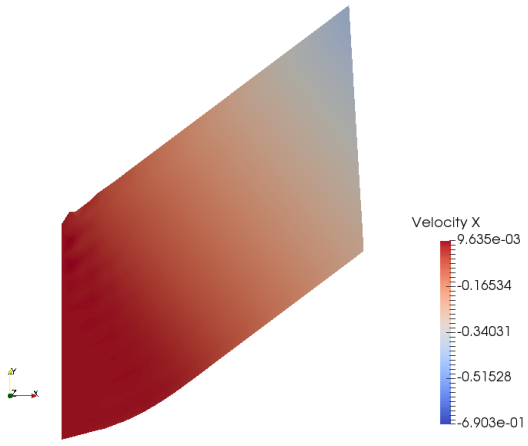

(b) Horizontal velocity (mm.s^{-1}) at 5s (10^{th} timestep).

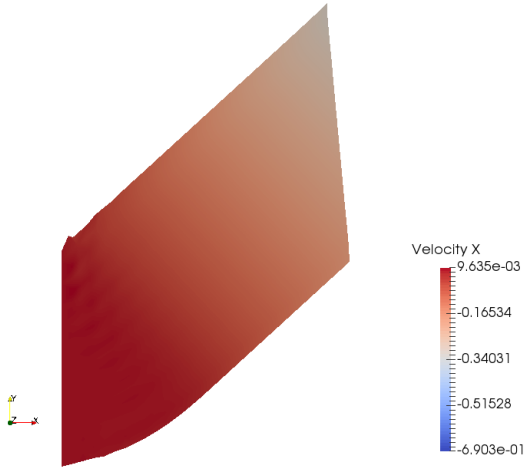

(c) Horizontal velocity (mm.s^{-1}) at 7.5s (15^{th} timestep).

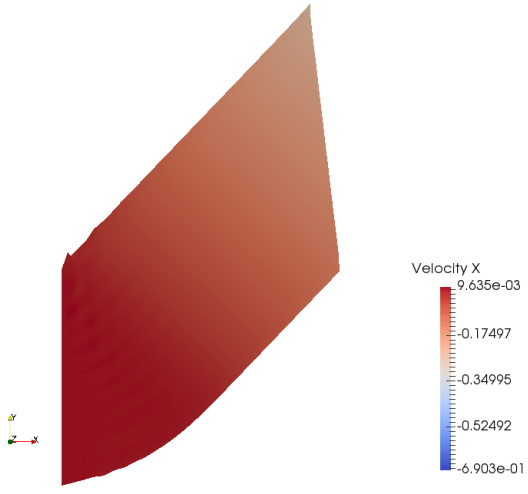

(d) Horizontal velocity (mm.s^{-1}) at 10s (20^{th} timestep).

Figure 2.9 – Horizontal velocity for the plane transverse shear, dynamic simulation.

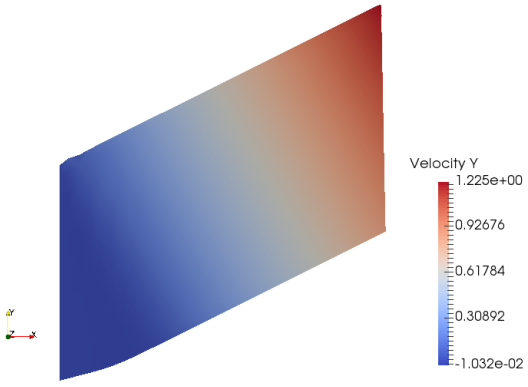

(a) Vertical velocity (mm.s^{-1}) at 2.5s (5^{th} timestep).

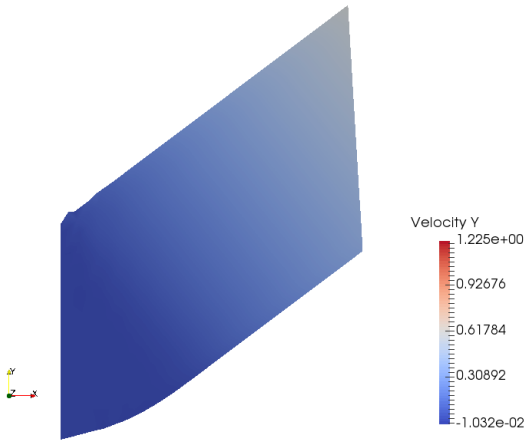

(b) Vertical velocity (mm.s^{-1}) at 5s (10^{th} timestep).

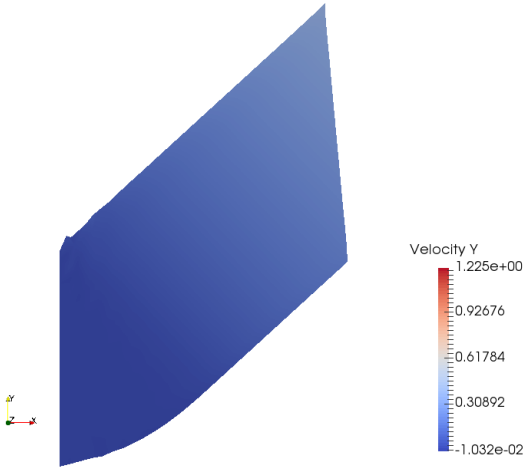

(c) Vertical velocity (mm.s^{-1}) at 7.5s (15^{th} timestep).

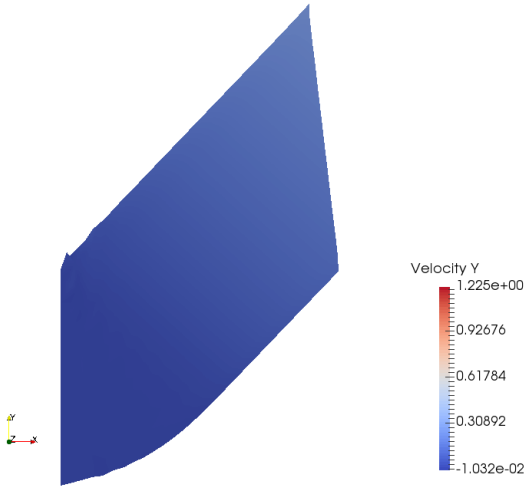

(d) Vertical velocity (mm.s^{-1}) at 10s (20^{th} timestep).

Figure 2.10 – Vertical velocity for the plane transverse shear, dynamic simulation.

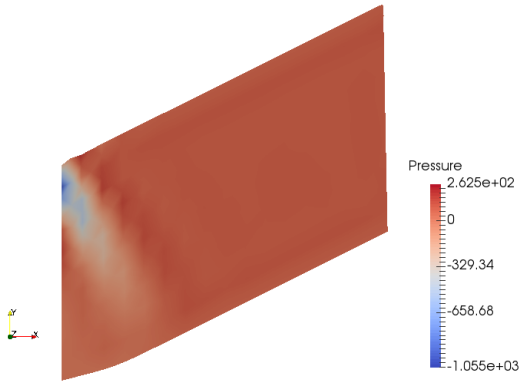

(a) Relative pressure (Pa) at 2.5s (5^{th} timestep).

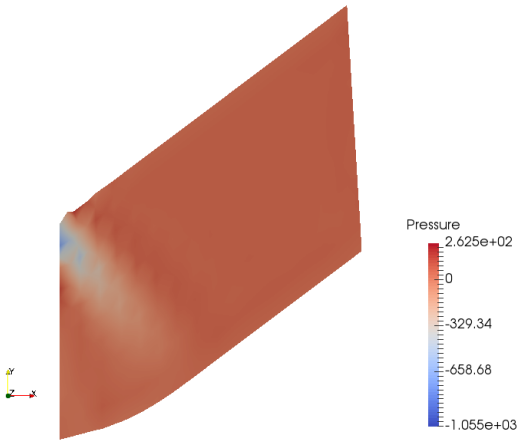

(b) Relative pressure (Pa) at 5s (10^{th} timestep).

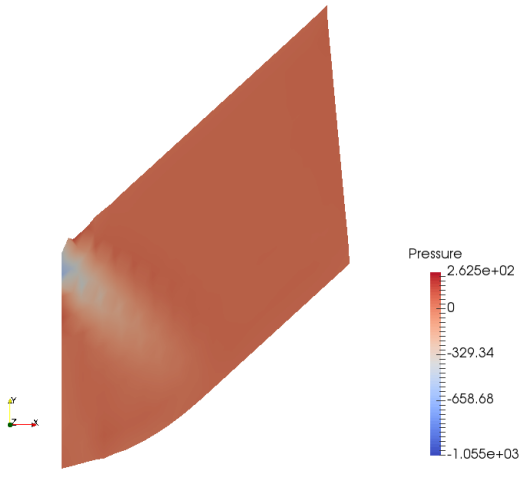

(c) Relative pressure (Pa) at 7.5s (15^{th} timestep).

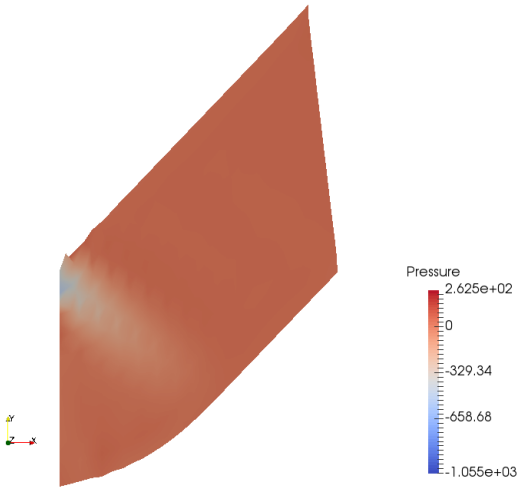

(d) Relative pressure (Pa) at 10s (20^{th} timestep).

Figure 2.11 – Relative pressure for the plane transverse shear, dynamic simulation.

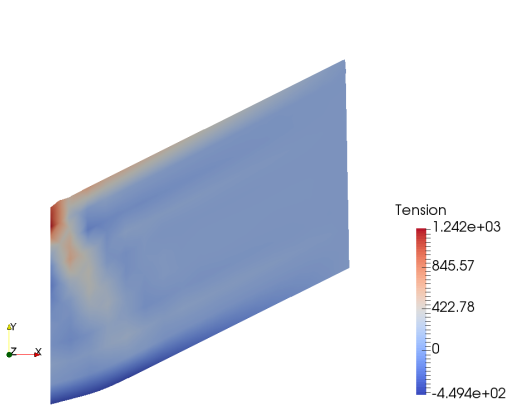

(a) Fibre tension (Pa) at 2.5s (5^{th} timestep).

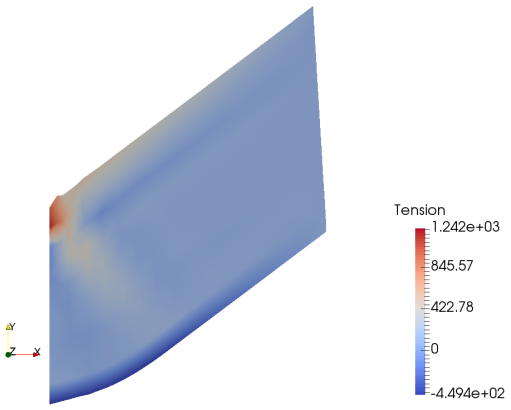

(b) Fibre tension (Pa) at 5s (10^{th} timestep).

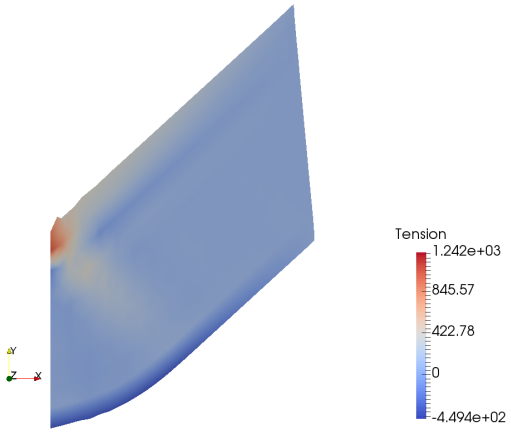

(c) Fibre tension (Pa) at 7.5s (15^{th} timestep).

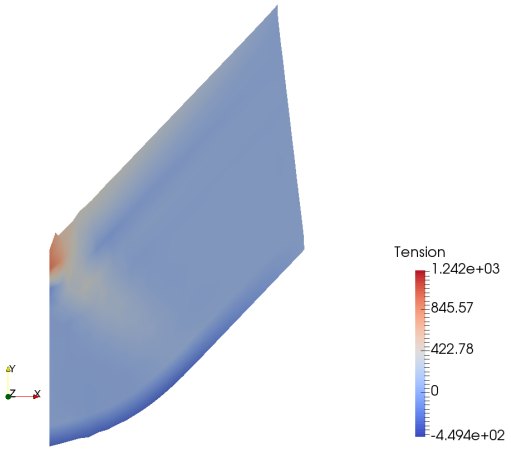

(d) Fibre tension (Pa) at 10s (20^{th} timestep).

Figure 2.12 – Fibre tension for the plane transverse shear, dynamic simulation.

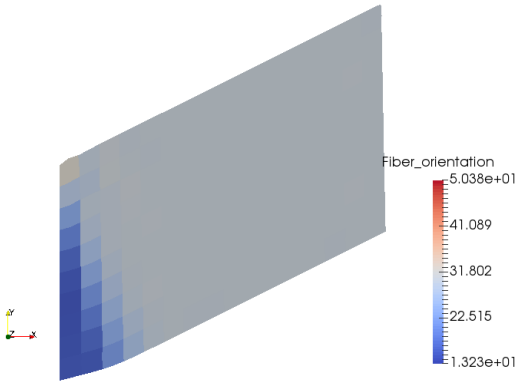

(a) Fibre orientation (°) at 2.5s (5^{th} timestep).

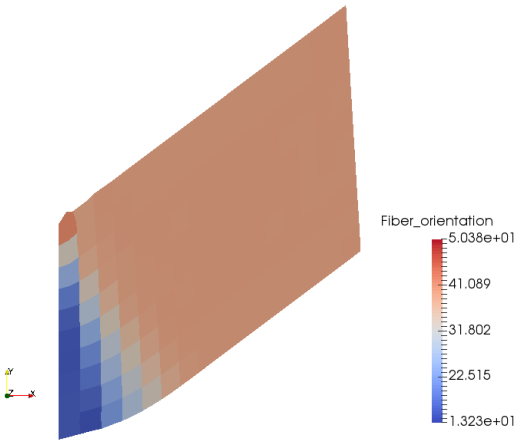

(b) Fibre orientation (°) at 5s (10^{th} timestep).

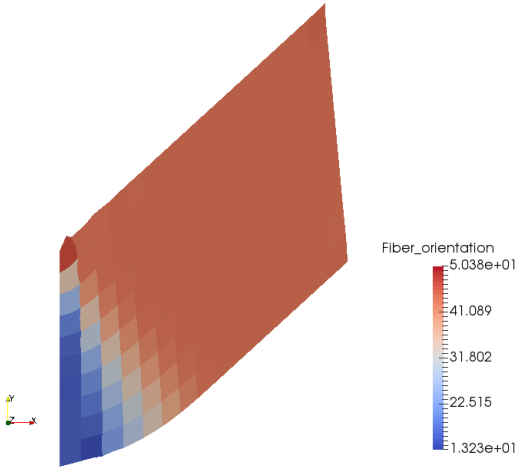

(c) Fibre orientation (°) at 7.5s (15^{th} timestep).

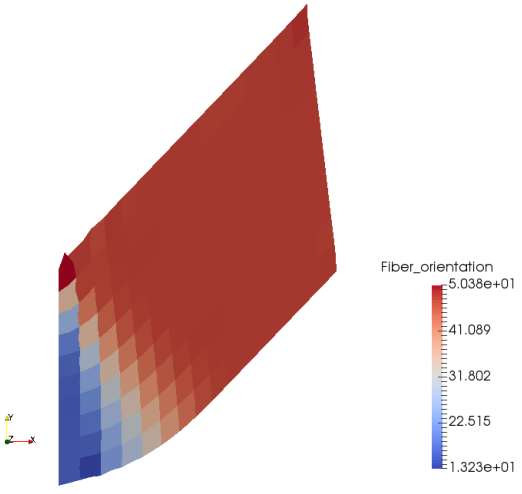

(d) Fibre orientation (°) at 10s (20^{th} timestep).

Figure 2.13 – Fibre orientation for the plane transverse shear, dynamic simulation.

2.3.3 Traction with two different fibre orientations

To further verify the validity of the computed fibre tension field, the more complex case of traction with two different fibre orientations was computed to examine the model's response when addressing a sharp discontinuity in material properties. The problem defined is presented in Figure 2.14. The size of the domain is 16 mm length and 10 mm wide. In the left half of the computational domain, fibres are horizontally oriented while they are in the vertical direction in the second half. A null velocity field is expected everywhere, in the left half because the horizontal fibres prevent the composite to flow in the traction direction and in the right half because the vertical fibres hinder the necking effect occurring due to the incompressibility. A null pressure field is expected in the left half, a fibre tension field positive in the left half and equal to the force applied and negative and equal to the necking force in the right half, and finally no fibre reorientation.

Results obtained using a continuous interpolation for the pressure and the fibre tension are presented in Section 2.3.3.1, and the results obtained using a discontinuous interpolation for the pressure and the fibre tension are presented in Section 2.3.3.1. These outcomes indicate that a discontinuous interpolation for the pressure and fibre tension fields yields better results as there is a sharp discontinuity in the material properties.

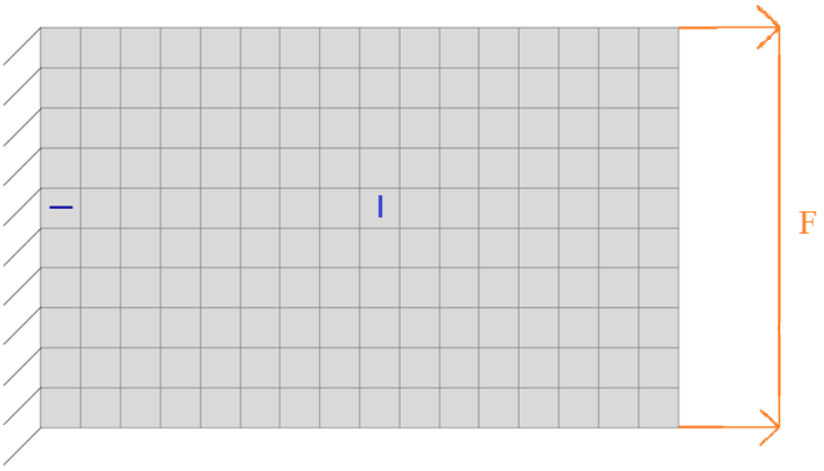

Figure 2.14 – Case of traction with two different fibre orientations problem. Velocity is imposed null on the left side and an horizontal Neumann condition is imposed on the right side, equal to 1N. The fibres on the left half of the domain are horizontal, and vertical in the right half. The elements are represented in the figure.

2.3.3.1 Continuous fibre tension

The results obtained using a continuous interpolation for the fibre tension are presented in Figure 2.15.

As presented in Figures 2.15a and 2.15b the velocity field is almost null everywhere. Figures 2.15c, 2.15d and 2.15e are consistent with the expected results dscussed in 2.3.3, although there are numerical instabilities since continuous interpolation functions were imposed to represent fields where discontinuity exists. As a result of this, the solution tries to accommodate the strong discontinuity without complete success.

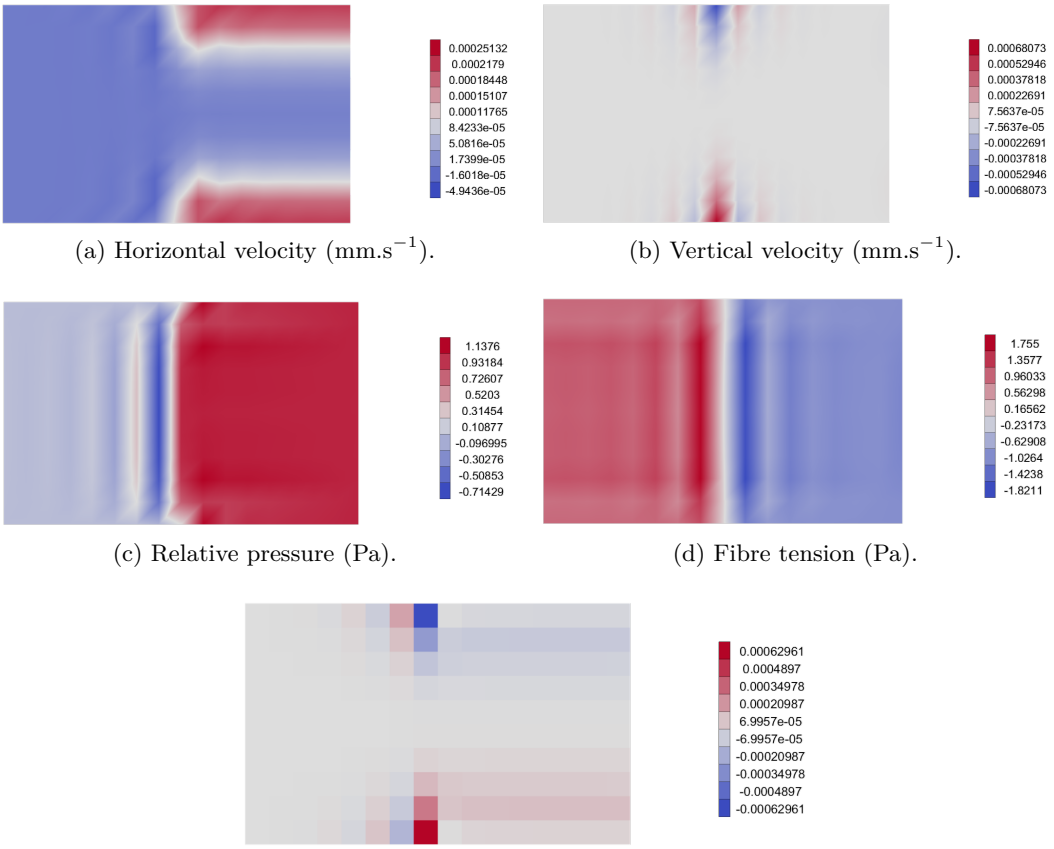

(a) Horizontal velocity (mm.s^{-1}).

(b) Vertical velocity (mm.s^{-1}).

(c) Relative pressure (Pa).

(d) Fibre tension (Pa).

(e) Fibre orientation (°).

Figure 2.15 – Results of the traction with two different fibre orientations using a continuous interpolation for the fibre tension.

2.3.3.2 Discontinuous fibre tension

The results obtained using a discontinuous interpolation for the fibre tension are presented in Figure 2.16.

As presented in Figure 2.16, results obtained with a discontinuous interpolation for the pressure and the fibre tension are far better than the results obtained using a continuous interpolation presented in Figure 2.15. Allowing a discontinuity between the elements in the pressure and fibre tension fields allows the results to perfectly accomodate the strong discontinuity presented in this case, leading to the expected results.

(a) Horizontal velocity (mm.s^{-1}).

(b) Vertical velocity, expressed in mm.s^{-1}.

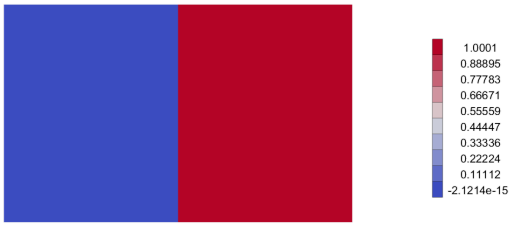

(c) Relative pressure (Pa).

(d) Fibre tension (Pa).

(e) Fibre orientation (°).

Figure 2.16 – Results of the traction with two different fibre orientations using a discontinuous interpolation for the fibre tension.

2.3.4 Tensile loading on sinusoidal fibres

During the compression of a stack of woven and even UD prepreg, most of the time the fibres are initially not perfectly aligned and they are straighten by the flow of polymer. To verify that the fibres in the model are able to realign, a case of tensile loading with initially sinusoidal fibres was treated. The problem is presented in Figure 2.17. The size of the domain is 16 mm length and 10 mm wide. The results obtained with a dynamic simulation are presented in this section. Continuous interpolation was used for the pressure and the fibre tension, simulation time is $t_{max} = 10$s and the timestep is $\delta t = 0.5$s. Figure 2.18 presents the horizontal velocity, Figure 2.19 the vertical velocity, Figure 2.20 the pressure, Figure 2.21 the fibre tension and Figure 2.22 the fibre orientation at $t = 2.5$s, $t = 5$s, $t = 7.5$s and $t = 10$s.

As presented in Figures 2.18 and 2.19 the fibres move to realign in the horizontal direction, carrying the resin with them as the material in the model is a homogenization of the resin and the fibres. The geometry is therefore allowed to extend in the horizontal direction to gradually reach the developed fibres' length.

The top right part moves differently than the other part due to the fact that the fibres are not continuous throughout all the geometry. Therefore when they realign they are not held by the left side and move in the horizontal direction.

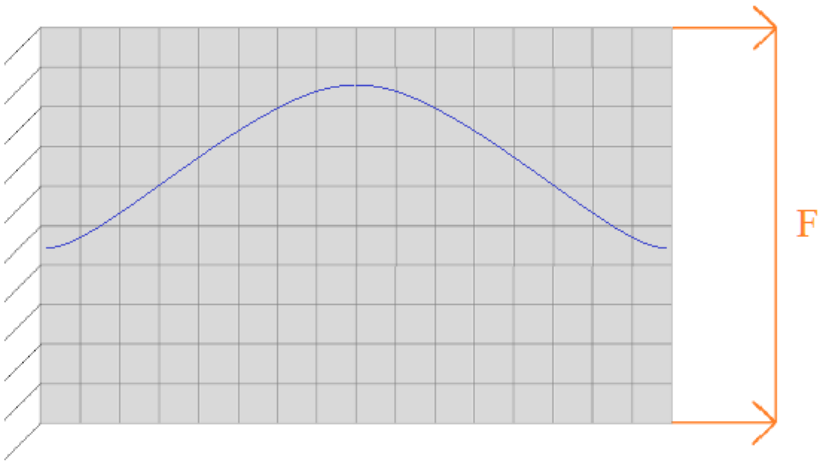

Figure 2.17 – Case of tensile loading on sinusoidal fibres. Velocity is imposed null on the left edge of the mesh and a horizontal Neumann condition is imposed on the right edge, equal to 100N. Elements are represented. Fibres describe a sinusoid in the horizontal direction and their orientation is the same throughout the width.

(a) Horizontal velocity (mm.s^{-1}) at 2.5s (5^{th} timestep).

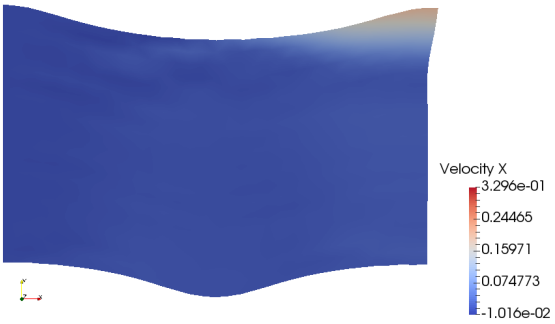

(b) Horizontal velocity (mm.s^{-1}) at 5s (10^{th} timestep).

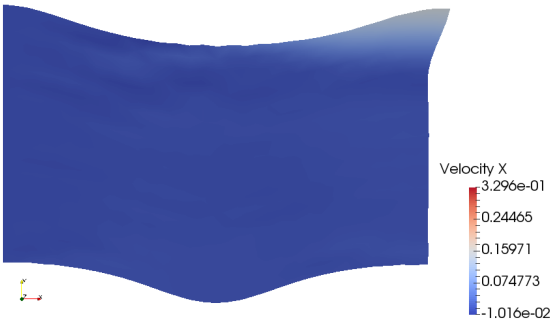

(c) Horizontal velocity (mm.s^{-1}) at 7.5s (15^{th} timestep).

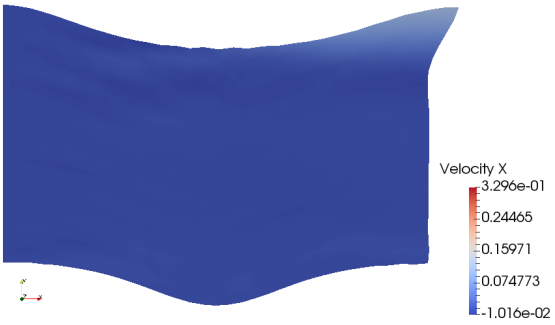

(d) Horizontal velocity (mm.s^{-1}) at 10s (20^{th} timestep).

Figure 2.18 – Horizontal velocity for the tensile loading on sinusoidal fibres, dynamic simulation.

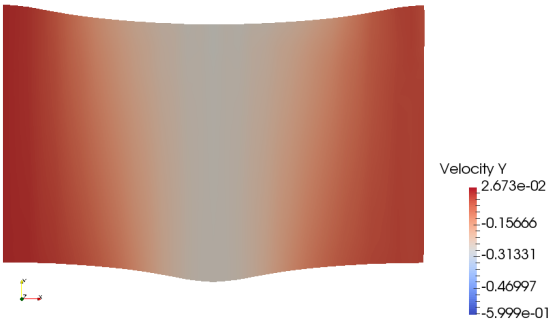

(a) Vertical velocity (mm.s^{-1}) at 2.5s (5^{th} timestep).

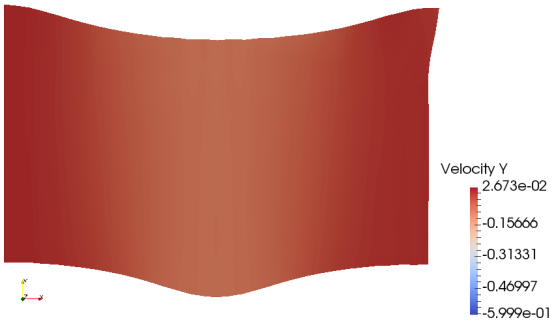

(b) Vertical velocity (mm.s^{-1}) at 5s (10^{th} timestep).

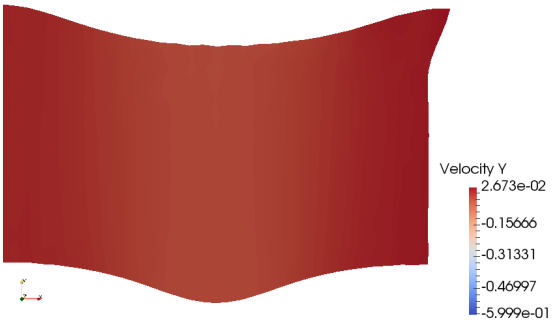

(c) Vertical velocity (mm.s^{-1}) at 7.5s (15^{th} timestep).

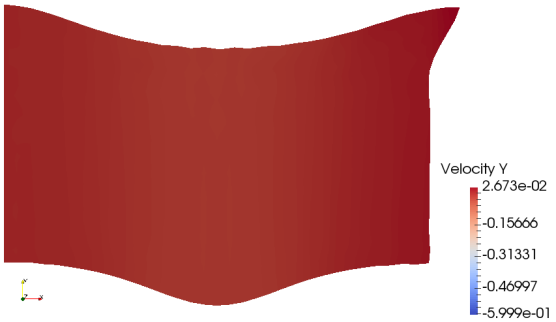

(d) Vertical velocity (mm.s^{-1}) at 10s (20^{th} timestep).

Figure 2.19 – Vertical velocity for the tensile loading on sinusoidal fibres, dynamic simulation.

As presented in Figure 2.21 the fibre tension increases while the fibres realign with the horizontal direction, the force being applied in the horizontal direction. This illustrates the fact that the fibres are not constraining the movement when they are not aligned with the applied force, while gradually increasing as they realign to finally prevent any movement when they are perfectly horizontal.

As presented in Figure 2.22 the fibres are gradually reoriented horizontaly as obtained experimentally. The reorientation is slower as the geometry is deformed due to the fact that the fibres in the center are closer to horizontal, restraining the movement of the others.

Considering the results presented in this section, it can be concluded that the TIF model is able to predict the realignement under load of initially wavy fibres. This is of interest when dealing with industrial manufacturing simulation taking into account the actual initial geometry for two major reasons:

- Fibres are never perfectly aligned in reality.
- This allows some extension, that can be used to facilitate the compression or to heal discontinuous patches.

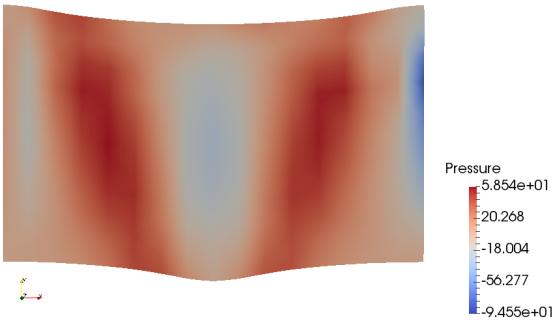

(a) Relative pressure (Pa) at 2.5s (5^{th} timestep).

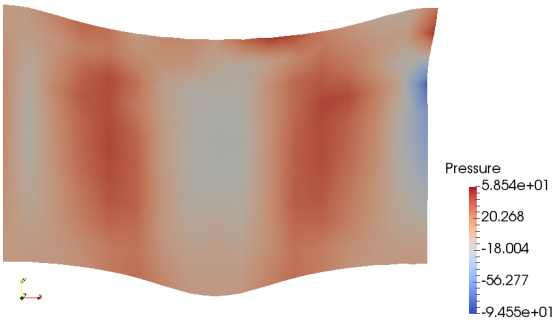

(b) Relative pressure (Pa) at 5s (10^{th} timestep).

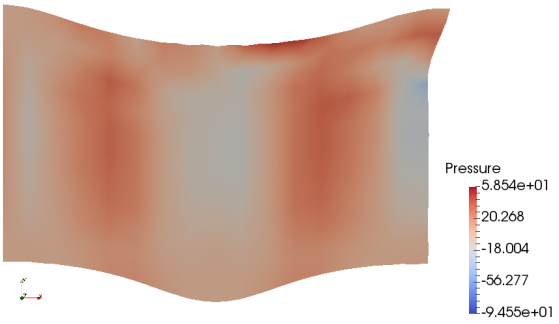

(c) Relative pressure (Pa) at 7.5s (15^{th} timestep).

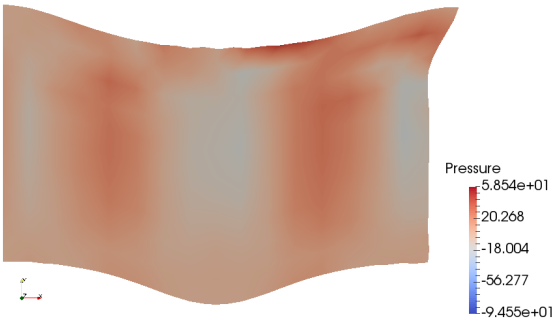

(d) Relative pressure (Pa) at 10s (20^{th} timestep).

Figure 2.20 – Relative pressure for the tensile loading on sinusoidal fibres, dynamic simulation.

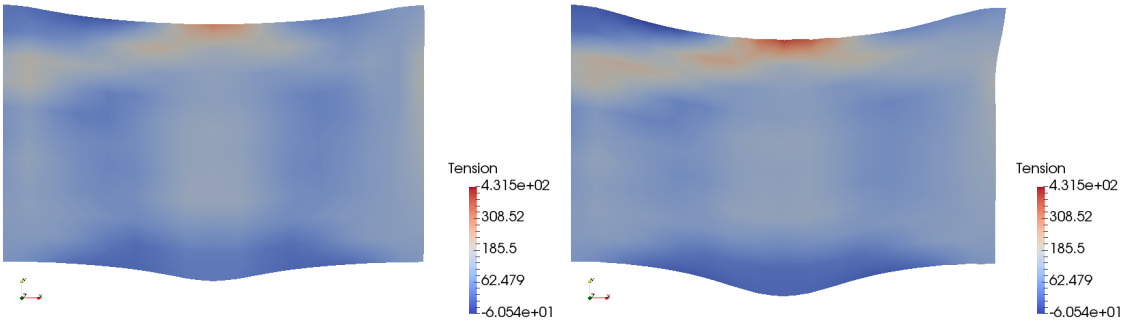

(a) Fibre tension (Pa) at 2.5s (5^{th} timestep).

(b) Fibre tension (Pa) at 5s (10^{th} timestep).

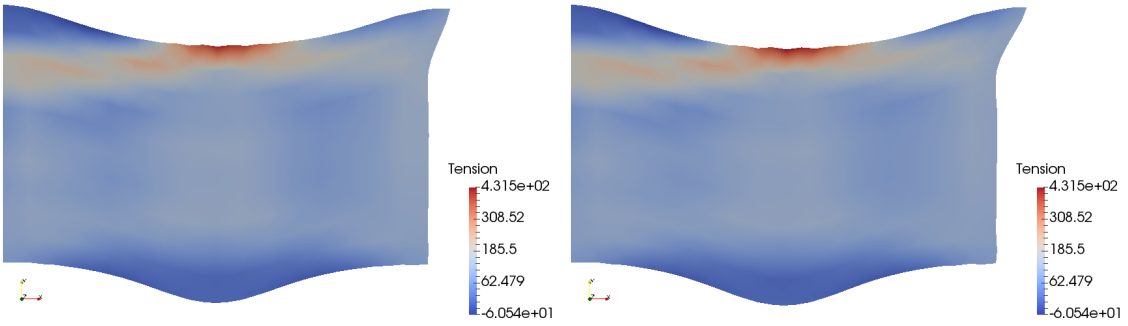

(c) Fibre tension (Pa) at 7.5s (15^{th} timestep).

(d) Fibre tension (Pa) at 10s (20^{th} timestep).

Figure 2.21 – Fibre tension for the tensile loading on sinusoidal fibres, dynamic simulation.

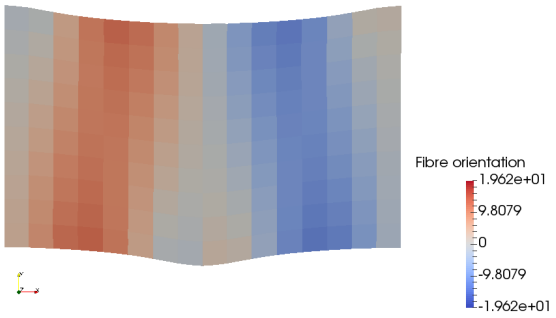

(a) Fibre orientation (°) at 2.5s (5^{th} timestep).

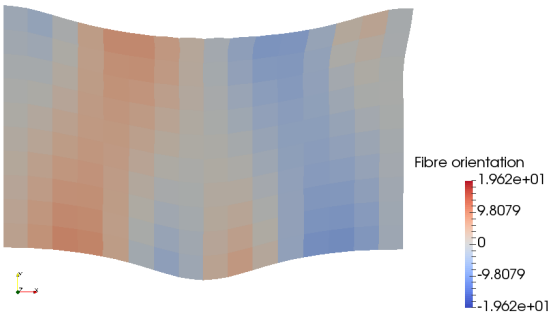

(b) Fibre orientation (°) at 5s (10^{th} timestep).

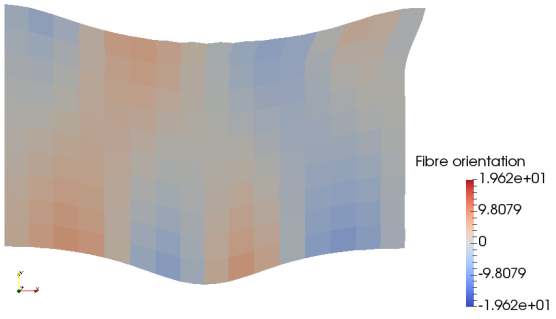

(c) Fibre orientation (°) at 7.5s (15^{th} timestep).

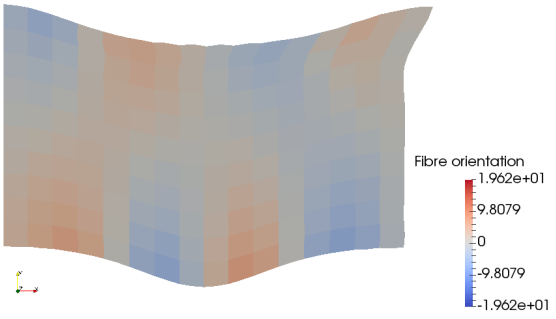

(d) Fibre orientation (°) at 10s (20^{th} timestep).

Figure 2.22 – Fibre orientation for the tensile loading on sinusoidal fibres, dynamic simulation.

2.3.5 Discontinuous patch under in-plane shearing, force, velocity and friction force

During the compression of a stack of ply containing a discontinuous patch within, the patch being not held it is free to move and deform. To verify that the model is able to simulate this behaviour, a case of mixed sollicitation was developed:

- fibres are placed horizontaly;
- horizontal velocity of 1 mm.s^{-1} is imposed on the right side, modelling the pulling of the patch by the tool;
- vertical force of 1N is imposed on the right side;
- horizontal force of -1N is imposed on all the domain, modelling the friction from the outside layers;
- vertical velocity is imposed null on the middle node to avoid rigid body motion.

The problem is presented in Figure 2.23. The size of the domain is 16 mm length and 10 mm wide. The results obtained with a dynamic simulation are presented in this section. Continuous interpolation was used for the pressure and the fibre tension, simulation time is $t_{max} = 10$s and the timestep is $\delta t = 0.5$s. Figure 2.24 presents the horizontal velocity, Figure 2.25 the vertical velocity, Figure 2.26 the pressure, Figure 2.27 the fibre tension and Figure 2.28 the fibre orientation at $t = 2.5$s, $t = 5$s, $t = 7.5$s and $t = 10$s.

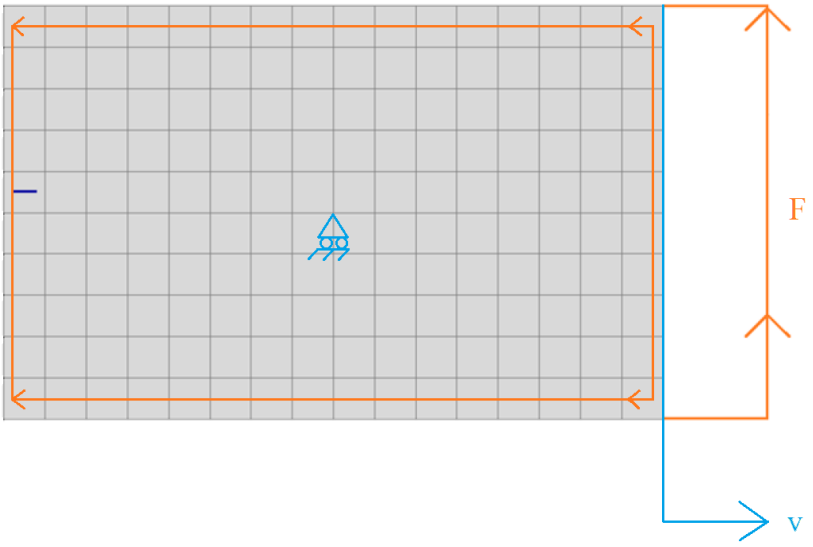

Figure 2.23 – Case of discontinuous patch under in-plane shearing, force, velocity and friction force. Horizontal velocity of 1 mm.s^{-1} and vertical force of 1N are applied on the right side, horizontal force of -1N is applied on all the domain. Elements are represented, fibres are placed horizontaly.

As can be seen in Figures 2.24 and 2.25 the velocity field corresponds to a solid body translation on the left side, and the plane shearing case on the right side. This is due to the vertical velocity blocked on the middle node decoupling the problem in two areas, the imposed horizontal velocity pulling all the geometry and the vertical force corresponding

(a) Horizontal velocity (mm.s^{-1}) at 2.5s (5^{th} timestep).

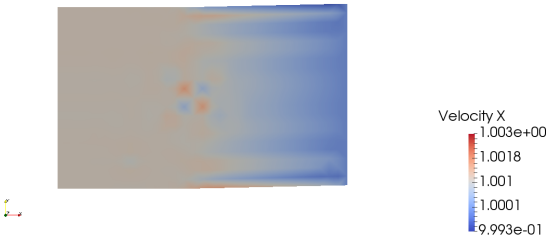

(b) Horizontal velocity (mm.s^{-1}) at 5s (10^{th} timestep).

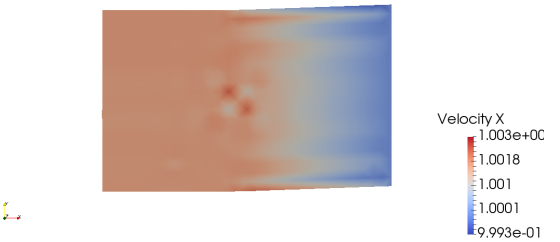

(c) Horizontal velocity (mm.s^{-1}) at 7.5s (15^{th} timestep).

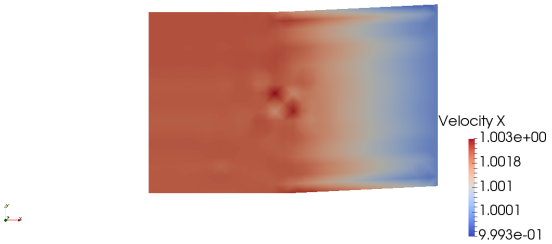

(d) Horizontal velocity (mm.s^{-1}) at 10s (20^{th} timestep).

Figure 2.24 – Horizontal velocity for the patch, dynamic simulation.

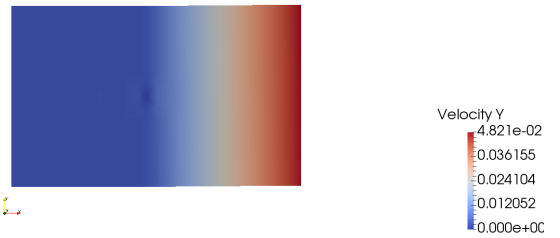

(a) Vertical velocity (mm.s^{-1}) at 2.5s (5^{th} timestep).

(b) Vertical velocity (mm.s^{-1}) at 5s (10^{th} timestep).

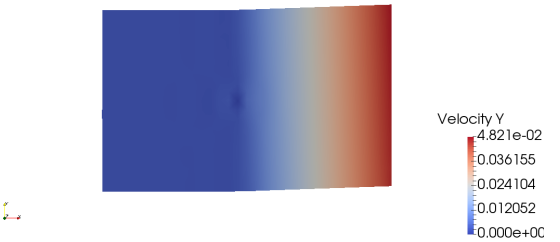

(c) Vertical velocity (mm.s^{-1}) at 7.5s (15^{th} timestep).

(d) Vertical velocity (mm.s^{-1}) at 10s (20^{th} timestep).

Figure 2.25 – Vertical velocity for the patch, dynamic simulation.

to a plane shearing on the right side. There is a numerical instability in the middle of the geometry due to the blocking of the vertical velocity on the middle node combined with the use of a continuous interpolation for the pressure and the fibre tension.

(a) Relative pressure (Pa) at 2.5s (5^{th} timestep).

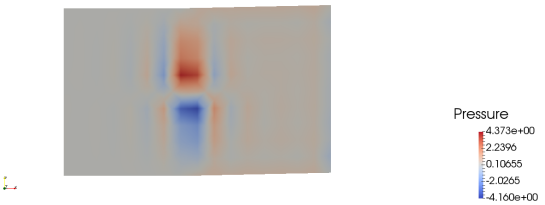

(b) Relative pressure (Pa) at 5s (10^{th} timestep).

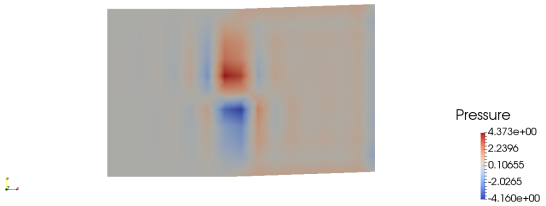

(c) Relative pressure (Pa) at 7.5s (15^{th} timestep).

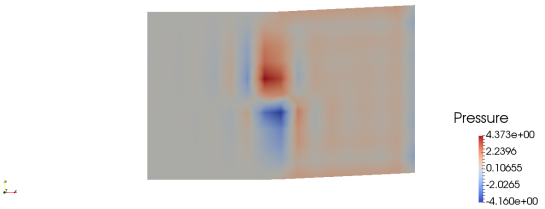

(d) Relative pressure (Pa) at 10s (20^{th} timestep).

Figure 2.26 – Relative pressure for the patch, dynamic simulation.

As presented in Figure 2.26 the pressure is nearly zero everywhere as the incompressibility is not sollicited in this problem, although there is an instability due to the blocking of the vertical velocity on the middle node.

As can be seen in Figure 2.27 the fibre tension on the left side is homogeneous and opposed to the friction force, and on the right side it corresponds to the sum of the tension opposed to the friction force and the tension obtained in the plane shearing case.

As can be expected, Figure 2.28 shows that on the left side the fibres are not moving as the only forces applied are horizontal, and on the right side they are homogeneously rotating as in the plane shearing case.

Considering the results presented in this section, it can be concluded that the TIF model is able to take into account the sliding of a ply subjected to an imposed velocity, imposed force and friction force, without numerical instabilities nor regularization. With the objective of optimizing the design of a composite part this can be of considerable interest as it allows to simulate the behaviour of discontinuous plies added in order to locally reinforce the structure without adding too much weight. As it allows to predict the position and configuration of the ply at the end of the forming process, it will allow to determine the initial position and configuration needed in order to achieve manufacturing of a part with optimized design including discontinuous patches.

(a) Fibre tension (Pa) at 2.5s (5^{th} timestep).

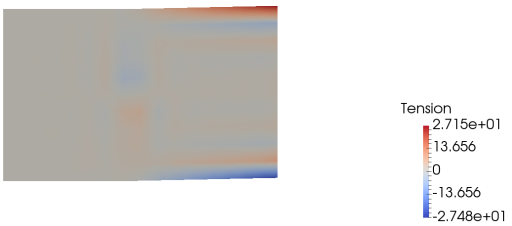

(b) Fibre tension (Pa) at 5s (10^{th} timestep).

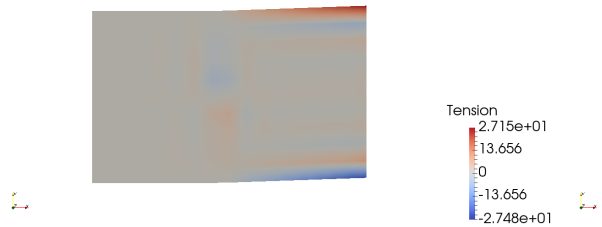

(c) Fibre tension (Pa) at 7.5s (15^{th} timestep).

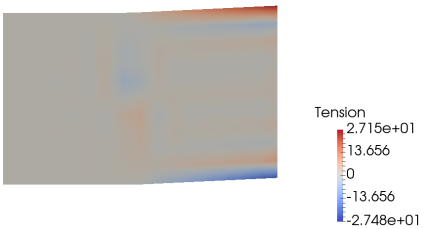

(d) Fibre tension (Pa) at 10s (20^{th} timestep).

Figure 2.27 – Fibre tension for the patch, dynamic simulation.

(a) Fibre orientation (°) at 2.5s (5^{th} timestep).

(b) Fibre orientation (°) at 5s (10^{th} timestep).

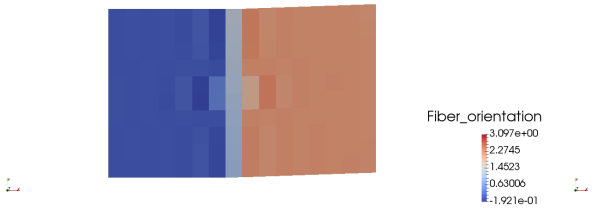

(c) Fibre orientation (°) at 7.5s (15^{th} timestep).

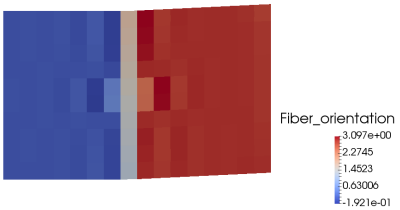

(d) Fibre orientation (°) at 10s (20^{th} timestep).

Figure 2.28 – Fibre orientation for the patch, dynamic simulation.

2.3.6 Traction with randomly oriented fibres

In order to verify the stability of the model, a case of traction on randomly oriented fibres, within the ±20° range, was computed. The problem is presented in Figure 2.29. The size of the domain is 16 mm length and 10 mm wide. The results obtained with a dynamic simulation are presented in this section. Continuous interpolation was used

for the pressure and the fibre tension, simulation time is $t_{max} = 10$s and the timestep is $\delta t = 0.5$s. Figure 2.30 presents the horizontal velocity, Figure 2.31 the vertical velocity, Figure 2.32 the pressure, Figure 2.33 the fibre tension and Figure 2.34 the fibre orientation at $t = 2.5$s, $t = 5$s, $t = 7.5$s and $t = 10$s. As a continuous interpolation was used this problem corresponds to continuous fibres randomly deposited, and not randomly placed chips of prepreg.

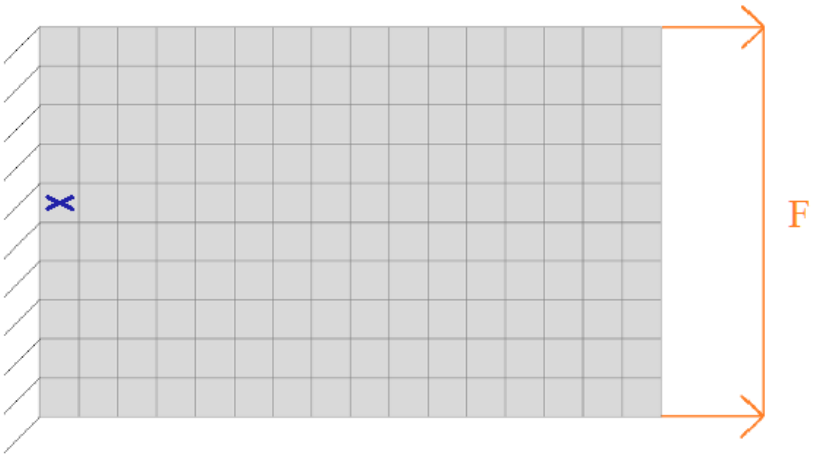

Figure 2.29 – Case of traction with randomly oriented fibres. Velocity is imposed null on the left edge of the mesh and a horizontal Neumann condition is imposed on the right edge, equal to 1N. Elements are represented, fibres are randomly oriented within the $\pm 20°$ range.

As presented in Figures 2.30 and 2.31 the velocity field accomodates with the random orientation. The more deformed the geometry is, the smaller the velocity is, because the fibre realignment strengthens the material in the direction of the imposed force. The vertical symmetry is a coincidence.

As presented in Figure 2.34 the fibres realign with the horizontal direction when pulled. There are some elements that do not realign due to the fact that the neighbour elements are blocking their movement.

Considering the results presented in this section, it can be concluded that the TIF model is able to simulate a patch of randomly oriented fibres, without numerical instabilities nor regularization, even with the use of an explicit update scheme.

(a) Horizontal velocity (mm.s^{-1}) at 2.5s (5^{th} timestep).

(b) Horizontal velocity (mm.s^{-1}) at 5s (10^{th} timestep).

(c) Horizontal velocity (mm.s^{-1}) at 7.5s (15^{th} timestep).

(d) Horizontal velocity (mm.s^{-1}) at 10s (20^{th} timestep).

Figure 2.30 – Horizontal velocity for the traction with randomly oriented fibres, dynamic simulation.

(a) Vertical velocity (mm.s^{-1}) at 2.5s (5^{th} timestep).

(b) Vertical velocity (mm.s^{-1}) at 5s (10^{th} timestep).

(c) Vertical velocity (mm.s^{-1}) at 7.5s (15^{th} timestep).

(d) Vertical velocity (mm.s^{-1}) at 10s (20^{th} timestep).

Figure 2.31 – Vertical velocity for the traction with randomly oriented fibres, dynamic simulation.

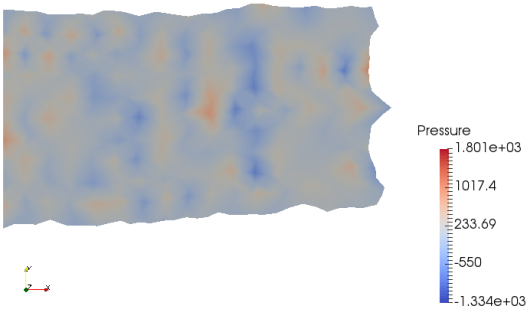

(a) Relative pressure (Pa) at 2.5s (5^{th} timestep).

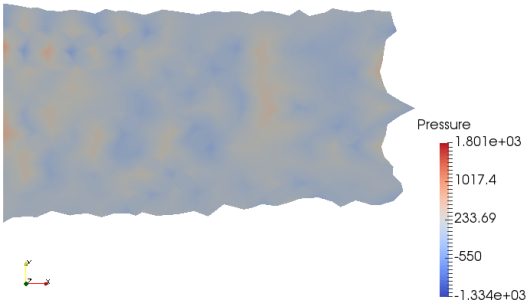

(b) Relative pressure (Pa) at 5s (10^{th} timestep).

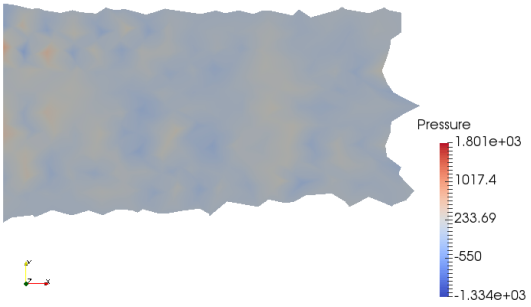

(c) Relative pressure (Pa) at 7.5s (15^{th} timestep).

(d) Relative pressure (Pa) at 10s (20^{th} timestep).

Figure 2.32 – Relative pressure for the traction with randomly oriented fibres, dynamic simulation. Pressure imposed at the right edge is 10^3 Pa.

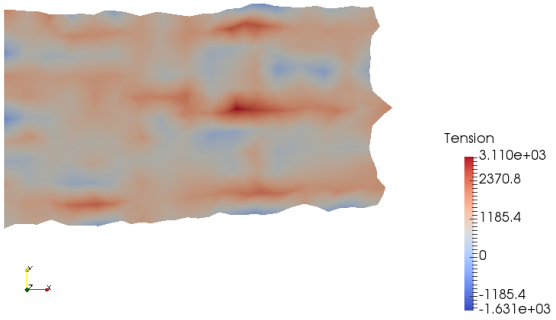

(a) Fibre tension (Pa) at 2.5s (5^{th} timestep).

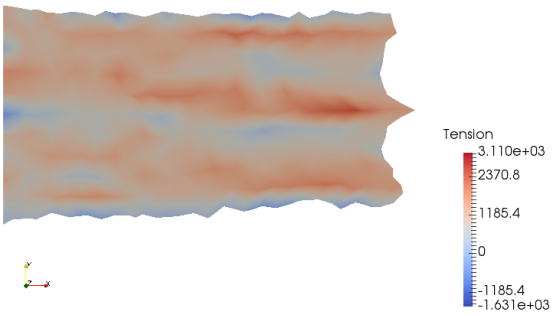

(b) Fibre tension (Pa) at 5s (10^{th} timestep).

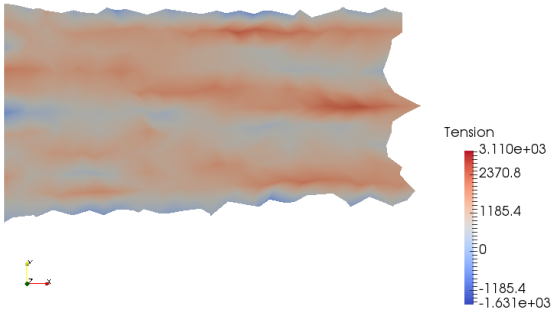

(c) Fibre tension (Pa) at 7.5s (15^{th} timestep).

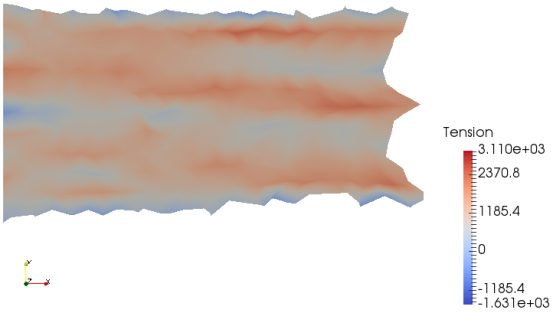

(d) Fibre tension (Pa) at 10s (20^{th} timestep).

Figure 2.33 – Fibre tension for the traction with randomly oriented fibres, dynamic simulation.

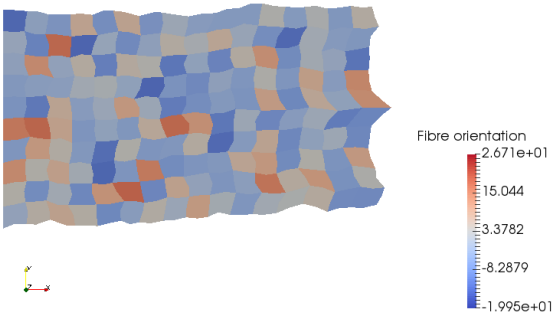

(a) Fibre orientation (°) at 2.5s (5^{th} timestep).

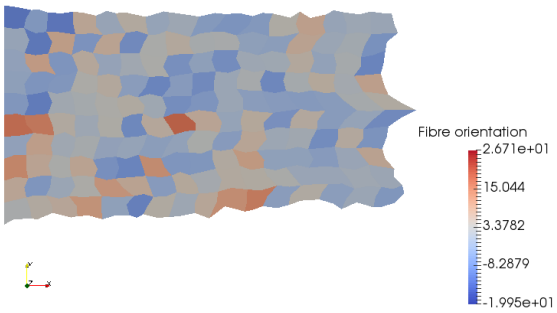

(b) Fibre orientation (°) at 5s (10^{th} timestep).

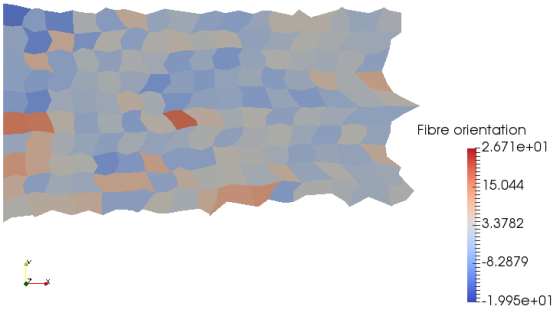

(c) Fibre orientation (°) at 7.5s (15^{th} timestep).

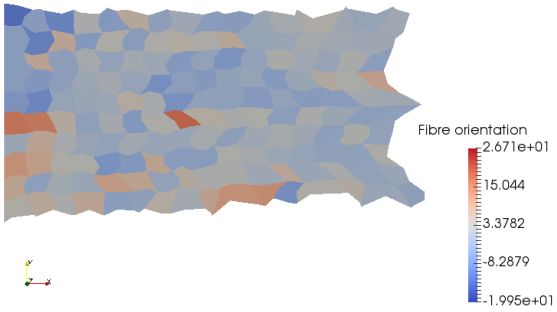

(d) Fibre orientation (°) at 10s (20^{th} timestep).

Figure 2.34 – Fibre orientation for the traction with randomly oriented fibres, dynamic simulation.

2.3.7 Pulling out of a single layer from a 0° stack

During the forming process, discontinuous plies can move when subjected to viscous drag forces. This is observed in vertical areas of parts as a consequence of the top mould closing, a shearing traction happens that induces a relative displacement of plies due to the viscous interactions. To verify that the model is able to retrieve this behaviour, a model representing a stack of five plies with a resin layer interface governed by the Stokes equation was developped. The middle ply is pulled out of the stack at a constant velocity. The resin layer interface and its importance on the squeeze flow kinematics of the viscous laminate will be presented in Chapter 3. The problem is presented in Figures 2.35 and 2.36. The size of the domain is 9 mm length and 4.5 mm wide. The thickness of each resin layer is assumed to be uniform throughout its cross section and this thickness is equal for all layers. The traction applied to the middle ply will induce velocity and stress fields, which will be function of position in the laminate. The material on the left side is squeezed out of the composite layers, while being pulled in the right direction. As the pulling is dominant compared to the squeezing, the global displacement of the resin layer is in the right direction.

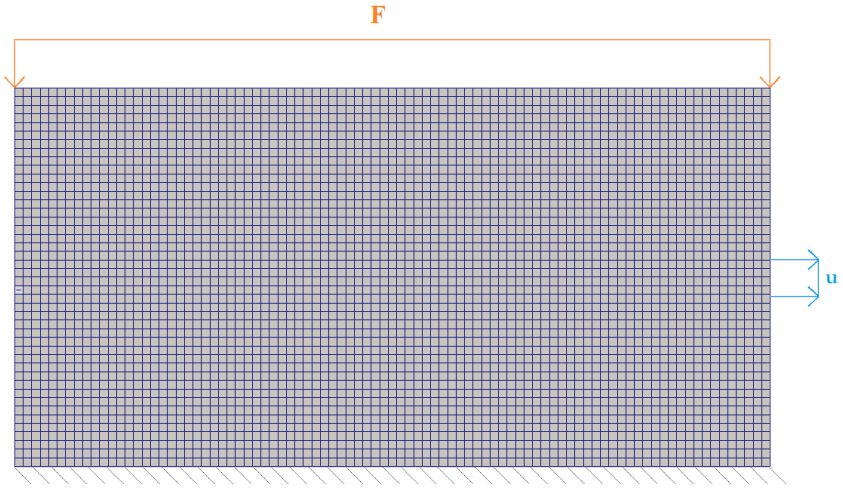

Figure 2.35 – Case of the pulling out of a single layer from a 0° stack. Horizontal velocity is imposed null on the top side, horizontal and vertical velocity is imposed null on the bottom side, a vertical Neumann condition is imposed on the top side, equal to 1N, and an horizontal velocity is imposed on the right side of the middle layer, equal to 1 $mm.s^{-1}$.

Results are presented in Figure 2.37.

It can be seen in Figure 2.37a that the plies that are not directly pulled out are moving due to the viscous interactions between the plies, which is driven by the pure resin layer at the interface. Figure 2.37c shows that the pressure is very low as the incompressibility is not activated by the boundary conditions. Vertical velocity, presented in Figure 2.37b is mostly induced by the compressive force. Figre 2.37d shows that a complex fibre tension arises, due to the fact that the fibres are pulled in both directions at the same time.

Figure 2.38 presents the geometry of the laminate after deformation. It can be seen that the outer layers deform more than they move, whereas the other layers move more than they deform. As only the middle layer is pulled out, the two TIF layers on both sides move under the viscous drag forces induced by the displacement of the middle layer.

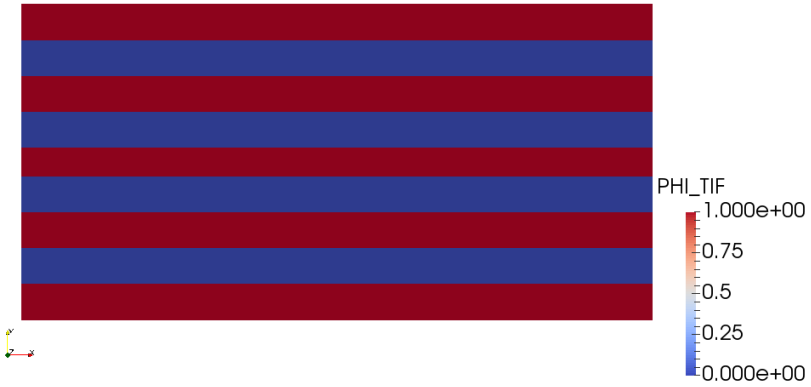

Figure 2.36 – Laminate cross-section. The TIF layers are represented in red and the resin layers are represented in blue.

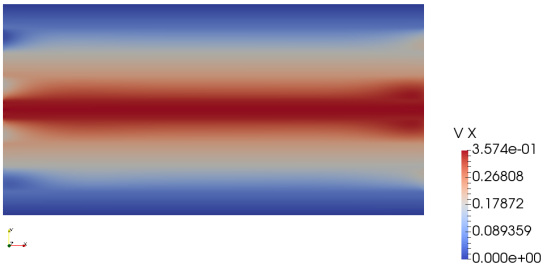

(a) Horizontal velocity (mm.s^{-1}).

(b) Vertical velocity (mm.s^{-1}).

(c) Relative pressure (Pa).

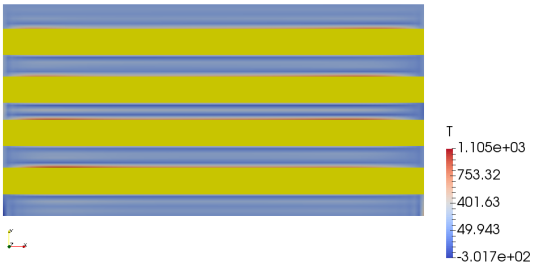

(d) Fibre tension (Pa).

Figure 2.37 – Results of the pulling of a single layer from a 0° stack, using a continuous interpolations for the pressure and the fibre tension.

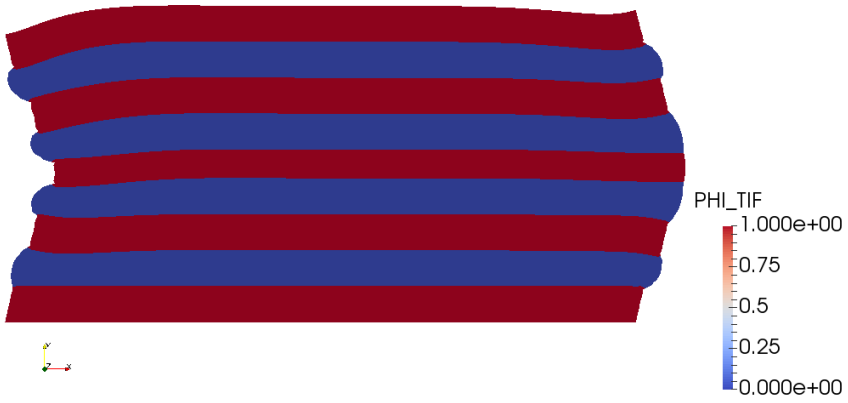

Figure 2.38 – Geometry of the laminate after deformation. The red represents the TIF layers and the blue represents the resin interfaces. A multiplicative factor of 2 was applied.

2.3.8 45° tensile test

One of the characterization test on a composite ply is the 45°tensile test of in-plane shear modulus and strength. To check wether this characterization test can be done numerically, a case of traction on 45° oriented fibres was computed. As the computation is 2D only a single ply was modelled, to take into account a second ply a 3D model is necessary. The problem is presented in Figure 2.39. The size of the domain is 16 mm length and 10 mm wide. The quantity of interest is the value of the angle under constant load, which will be represented with respect to the time. These results can then be used to identify the materials parameters from a tensile test, avoiding the need for more complicated experimental characterization.

Results obtained with different values of the applied force will be presented in Section 2.3.8.1, with different values of the fibre fraction in Section 2.3.8.2 and with different values of the resin viscosity in Section 2.3.8.3. All results were obtained using a continuous interpolation for the pressure and the fibre tension.

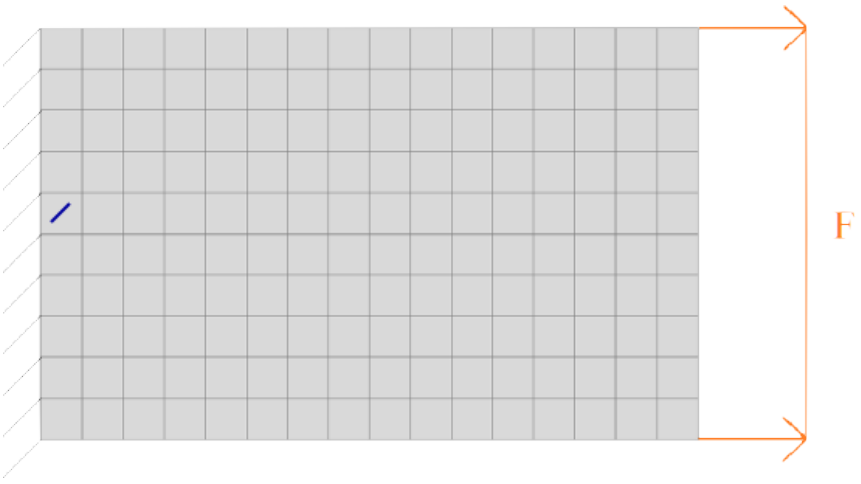

Figure 2.39 – Case of a tensile test on 45° oriented fibres. Velocity is imposed null on the left edge of the mesh and a horizontal Neumann condition on the right edge which value may vary. Fibres are represented by the blue segments, elements are represented too.

2.3.8.1 Variation of the applied force

The resin viscosity was set to $\eta = 200$Pa.s, fibre fraction $v_f = 56.9\%$ and applied force range from $F = 100$N to $F = 500$N with a step of 100N. The results are presented in Figure 2.40.

As can be seen in Figure 2.40 the fibres gradually realign towards the horizontal direction. The higher the applied force is, the faster they realign, which is the expected behaviour.

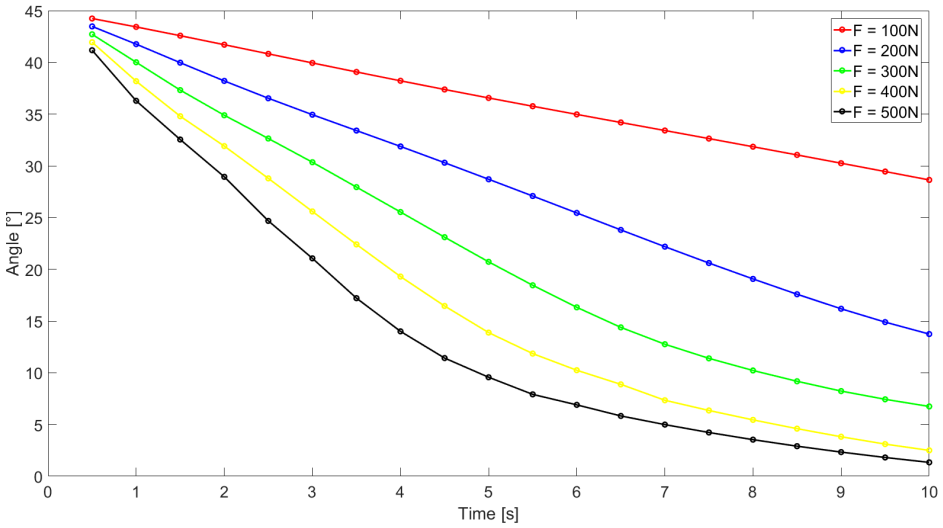

Figure 2.40 – Closing angle with respect to time for different values of applied force.

2.3.8.2 Variation of the fibre fraction

The resin viscosity was set to $\eta = 200$Pa.s, applied force $F = 500$N and fibre fraction range from $v_f = 48.9\%$ to $v_f = 56.9\%$ with a step of 2%. The results are presented in Figure 2.41.

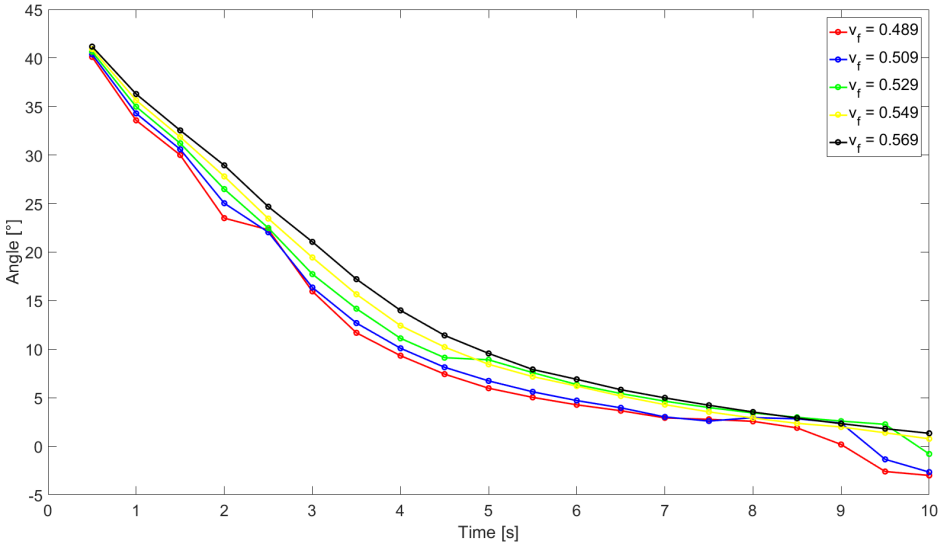

Figure 2.41 – Closing angle with respect to time for different values of fibre fraction.

As can be seen in Figure 2.41 the fibres gradually realign towards the horizontal direction. The higher the fibre fraction is, the slower they realign, which is the expected behaviour.

2.3.8.3 Variation of the resin viscosity

The applied force was set to $F = 500\,\mathrm{N}$, fibre fraction $v_f = 56.9\%$ and resin viscosity range from $\eta = 100\,\mathrm{Pa.s}$ to $\eta = 500\,\mathrm{Pa.s}$ with a step of $100\,\mathrm{Pa.s}$. It represents the influence of the temperature drop when the prepregs are cooled down in cold mould. The results are presented in Figure 2.42.

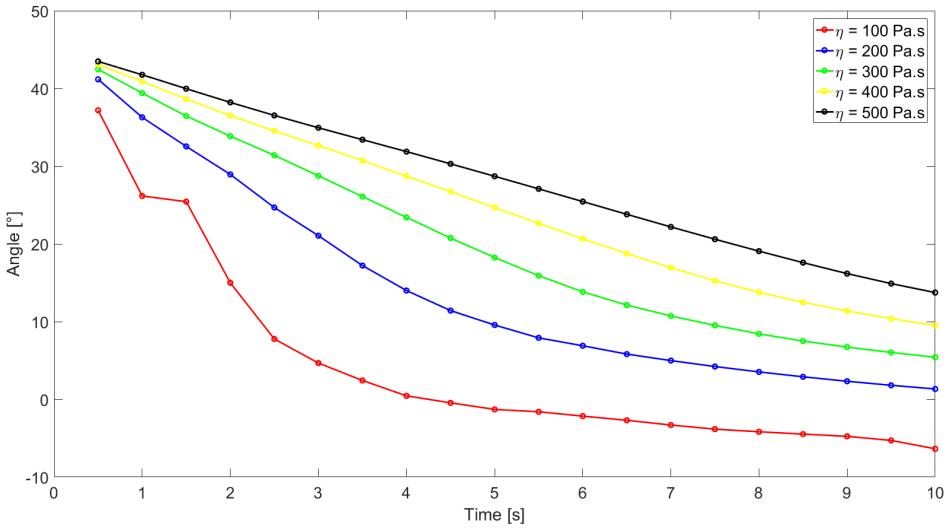

Figure 2.42 – Closing angle with respect to time for different values of resin viscosity. The curve for $\eta = 100$ Pa.s is not smooth as the computation presented an instability for this value.

As can be seen in Figure 2.42 the fibres gradually realign towards the horizontal direction. The higher the resin viscosity is, the slower they realign, which is the expected behaviour.

Conclusion

This chapter presented the formulation of the 2D Transversely Isotropic Fluid (TIF) model, its numerical simulation and some numerical results.

This model is able to give the expected results when the test case is simple, such as the traction along the fibre direction or the in-plane shearing. It was also demonstrated that in the case of a discontinuity in the problem, such as a sharp change in material properties, the use of discontinuous interpolation functions for the pressure and the fibre tension is mandatory to obtain good results, whereas when all properties are continuous the used of continuous interpolation functions for the pressure and the fibre tension yields better results.

The numerical tests conducted on the model showed that it is able to take into account an initial fibre misalignment, and that fibres realign correctly when subjected to traction. The case of misaligned fibres under compression necessitates the 3D model. The model is also able to simulate moving patches subjected to imposed velocity and imposed forces as well as displacement induced by viscous drag forces.

Results demonstrated the stability of the dynamic solution despite the use of an explicit update scheme, and this on each computed case even with randomly oriented fibres.

Finally, it was showed that the model gives consistent results when used to obtain quantities of interest over time for different material properties. This could be used to substitute numerical property identification to experimental characterization.

References

[1] S. P. McEntee and C. M. Ó. Brádaigh, "Large deformation finite element modelling of single-curvature composite sheet forming with tool contact", *Composites Part A: Applied Science and Manufacturing*, vol. 29, no. 1, pp. 207–213, 1998 (cit. on pp. 3, 32).

[2] T. G. Rogers, "Rheological characterization of anisotropic materials", *Composites*, vol. 20, no. 1, pp. 21–27, Jan. 1989, ISSN: 00104361. DOI: 10.1016/0010-4361(89)90677-0 (cit. on pp. 32, 34–36).

[3] A. C. Pipkin and T. G. Rogers, "Plane deformations of incompressible fiber-reinforced materials", *Journal of Applied Mechanics*, vol. 38, no. 3, p. 634, 1971. DOI: 10.1115/1.3408866 (cit. on p. 32).

[4] A. J. M. Spencer, *Deformations of fibre-reinforced materials*, ser. Oxford science research papers. Clarendon Press, 1972 (cit. on p. 32).

[5] C. M. Ó. Brádaigh and R. B. Pipes, "Finite element analysis of composite sheet-forming process", *Composites Manufacturing*, vol. 2, no. 3-4, pp. 161–170, 1991 (cit. on p. 32).

[6] G. B. McGuinness and C. M. Ó. Brádaigh, "Development of rheological models for forming flows and picture-frame shear testing of fabric reinforced thermoplastic sheets", *Journal of Non-Newtonian Fluid Mechanics*, vol. 73, no. 1, pp. 1–28, 1997 (cit. on p. 32).

[7] A. J. M. Spencer, "Theory of fabric-reinforced viscous fluids", *Composites Part A: Applied Science and Manufacturing*, vol. 31, no. 12, pp. 1311–1321, 2000 (cit. on p. 32).

[8] A. J. M. Spencer, "A theory of viscoplasticity for fabric-reinforced composites", *Journal of the Mechanics and Physics of Solids*, vol. 49, no. 11, pp. 2667–2687, 2001 (cit. on p. 32).

[9] A. J. M. Spencer, "Some results in the theory of non-Newtonian transversely isotropic fluids", *Journal of Non-Newtonian Fluid Mechanics*, vol. 119, no. 1-3, pp. 83–90, May 2004, ISSN: 03770257. DOI: 10.1016/j.jnnfm.2002.12.001 (cit. on p. 32).

[10] E. A. D. Lamers, R. Akkerman, and S. Wijskamp, "Fibre orientation modelling for rubber press forming of thermoplastic laminates", *International Journal of Forming Processes*, vol. 6, no. 3-4, pp. 443–463, 2003 (cit. on p. 32).

[11] E. A. D. Lamers, *Shape distortions in fabric reinforced composite products due to processing induced fibre reorientation*. University of Twente, 2004 (cit. on p. 32).

[12] R. H. W. Ten Thije, R. Akkerman, and J. Huétink, "Large deformation simulation of anisotropic material using an updated lagrangian finite element method", *Computer methods in applied mechanics and engineering*, vol. 196, no. 33, pp. 3141–3150, 2007 (cit. on p. 33).

[13] S. P. Haanappel, R. H. W. Ten Thije, U. Sachs, B. Rietman, and R. Akkerman, "Formability analyses of uni-directional and textile reinforced thermoplastics", *Composites Part A: Applied science and manufacturing*, vol. 56, pp. 80–92, 2014 (cit. on p. 33).

[14] E. Gazo Hanna, "Procédé de formage des composites à fibres longues et matrice thermoplastique: analyse expérimentale et numérique du glissement interpli", PhD thesis, Ecole centrale de Nantes, 2011 (cit. on p. 33).

[15] C. M. Ó. Brádaigh, "Sheet Forming of Composite Materials", in *Flow and Rheology in Polymer Composites Manufacturing*, Elsevier Science B.V., 1994 (cit. on pp. 37, 114).

[16] T. J. R. Hughes, "Finite element analysis of incompressible viscous flows by the penalty function formulation", *Journal of Computational Physics*, vol. 30, pp. 1–60, Jul. 1974 (cit. on p. 38).

[17] J. Delmas, *Manuel code_aster - fonctions de forme et points d'intégration des éléments finis, fascicule r03.01.01*, EDF - Code Aster, Sep. 2010 (cit. on p. 38).

[18] A. Fortin and A. Garon, *Les éléments finis : de la théorie à la pratique*, 2011 (cit. on p. 38).

[19] P.-L. George and B. Houman, "Sur les éléments finis quadrilatéraux de degré 1 et 2", Research Report RR-7909, Mar. 2012, p. 39 (cit. on p. 38).

[20] O. A. Ladyzhenskaya and H. Salkow, *The mathematical theory of viscous incompressible flow*, 2d English ed., rev. and enl. Translated from the Russian by Richard A. Silverman and John Chu. New York : Gordon and Breach, 1969, ISBN: 9780980382914 (cit. on p. 39).

[21] I. Babuška, "The finite element method with lagrangian multipliers", *Numerische Mathematik*, vol. 20, no. 3, pp. 179–192, 1973, ISSN: 0945-3245. DOI: 10.1007/BF01436561 (cit. on p. 39).

[22] F. Brezzi, "On the existence, uniqueness and approximation of saddle-point problems arising from lagrangian multipliers", eng, *ESAIM: Mathematical Modelling and Numerical Analysis*, vol. 8, no. R2, pp. 129–151, 1974 (cit. on p. 39).

[23] P. Šimáček, V. N. Kaliakin, and R. B. Pipes, "Pathologies associated with the numerical analysis of hyper-anisotropic materials", *International Journal for Numerical Methods in Engineering*, vol. 36, no. 20, pp. 3487–3508, 1993, ISSN: 1097-0207. DOI: 10.1002/nme.1620362006 (cit. on p. 39).

[24] J. T. Oden, "Rip-methods for stokesian flows", The Institute for Computational Engineering and Sciences, The University of Texas at Austin, Research Report 80-11, 1980 (cit. on p. 39).

[25] O. C. Zienkiewicz, R. L. Taylor, and J. Z. Zhu, *The finite element method : its basis and fundamentals*. Amsterdam, Boston, Paris: Elsevier Butterworth-Heinemann, 2005, ISBN: 0-7506-6320-0 (cit. on p. 41).

[26] R. M. Christensen, "Effective viscous flow properties for fiber suspensions under concentrated conditions", *Journal of Rheology*, vol. 37, no. 1, pp. 103–121, Jan. 1993. DOI: 10.1122/1.550459 (cit. on pp. 41, 100).

Chapter 3

3D Transversely Isotropic Fluid model

Previous works presented only 2D results. This chapter will show that the behaviour is strictly 3D and therefore a 2D model cannot capture all the distinctive features reviewed in Chapter 1. 3D results will be presented, and it will be showed that they are closer to the experimental observations. Moreover, the results are computed using a mixed formulation, allowing the computation of the Lagrange multipliers and the velocity field with more accuracy.

Contents

3.1 Modification of the model

As discussed in 2.1 when considering a stack of plies a linear viscous fluid need to be inserted in order to model correctly the interface. Section 3.2.1.1 will present a result of compression when the resin layer is not considered, showing its necessity.

3.1.1 3D constitutive model of viscous uniaxial composite

Considering that the resin is viscous enough to neglect the acceleration effects, as was done with the resin reinforced with fibres, the resin can be modelled as a Stokes fluid, leading to the 3D behaviour law for the interface:

$$\underline{\underline{\sigma}} = \eta \underline{\underline{\dot{\varepsilon}}} - P \underline{\underline{1}}, \tag{3.1}$$

with η the viscosity of the resin. This equation is similar to the 3D behaviour law for the TIF model but isotropic and without the inextensibility constraint.

As Equations (2.2) and (3.1) are very similar, a monolithic approach can be used to impose continuity of the fluid between the plies and the interface while allowing the use of a single mesh for the whole stack.

Using such an approach leads to the 3D unified model for a stack of heterogeneous plies:

$$\underline{\underline{\sigma}} = \left(\eta \underline{\underline{1}} + \varphi_n \delta \underline{\underline{\underline{\underline{D}}}}_n \right) : \underline{\underline{\dot{\varepsilon}}} - P \underline{\underline{1}} + \varphi_n T \underline{a}_n \otimes \underline{a}_n, \tag{3.2}$$

with $\underline{a}_n$ the orientation vector of the n^{th} composite ply and φ_n a function that locates the position of the n^{th} composite ply in the mesh, defined as:

$$\varphi_n(\underline{x}) = \begin{cases} 1, & \text{if } \underline{x} \in \Omega_n \\ 0, & \text{otherwise,} \end{cases} \tag{3.3}$$

with Ω_n the domain of definition of the n^{th} composite ply, and $\delta \underline{\underline{\underline{\underline{D}}}}$ the difference between the orthotropic viscosity and the resin viscosity:

$$\delta \underline{\underline{\underline{\underline{D}}}}_n = 2\delta\eta_T \underline{\underline{\underline{\underline{1}}}} + 2(\delta\eta_L - \delta\eta_T) \underline{\underline{A}}_n \otimes \underline{\underline{A}}_n, \tag{3.4}$$

with $\delta\eta_T = \eta_T - \eta$ and $\delta\eta_L = \eta_L - \eta$.

3.1.2 Choice of shape functions

For the same reasons as those presented in Section 2.2.3, triquadratic interpolation functions are chosen for the velocity and trilinear interpolation functions are chosen for the pressure and the fibre tension. As hexahedron will give more accurate results than tetrahedron elements, a H27-8 elements is chosen.

The H27-8 elements contains 27 velocity nodes and 8 pressure/tension nodes with continuous interpolation for all the unknowns, as can be seen on Figure 3.1.

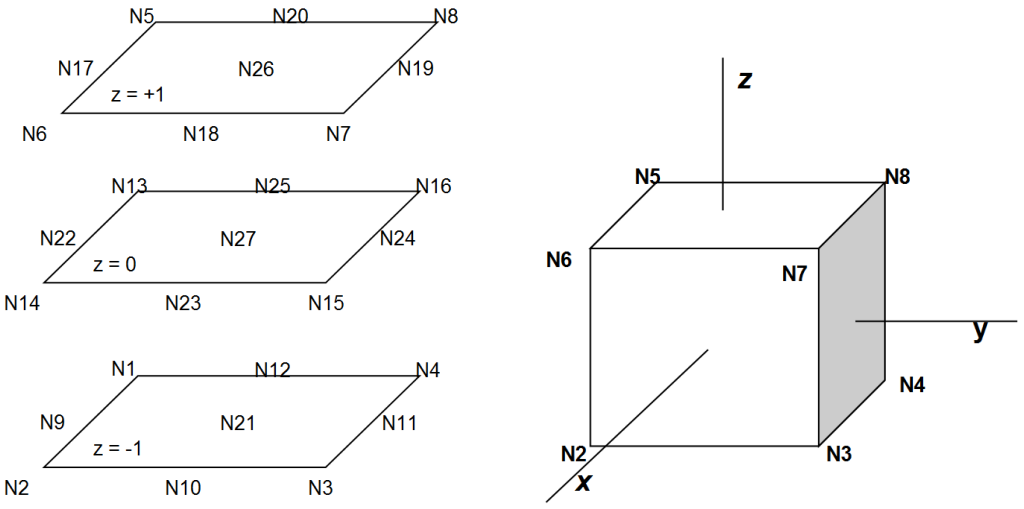

(a) Velocity nodes.

(b) Pressure/tension nodes.

Figure 3.1 – Nodes of the H27-8 element.

3.1.2.1 Velocity shape functions

Using a H27 element the shape functions for the velocity are triquadratic. Using the node numeration shown in Figure 3.1a the shape functions detailed in Table 3.1 are obtained.

Node	N	Node	N
1	$1/8x(x-1)y(y-1)z(z-1)$	15	$1/4x(x+1)y(y+1)(1-z^2)$
2	$1/8x(x+1)y(y-1)z(z-1)$	16	$1/4x(x-1)y(y+1)(1-z^2)$
3	$1/8x(x+1)y(y+1)z(z-1)$	17	$1/4(1-x^2)y(y-1)z(z+1)$
4	$1/8x(x-1)y(y+1)z(z-1)$	18	$1/4x(x+1)(1-y^2)z(z+1)$
5	$1/8x(x-1)y(y-1)z(z+1)$	19	$1/4(1-x^2)y(y+1)z(z+1)$
6	$1/8x(x+1)y(y-1)z(z+1)$	20	$1/4x(x-1)(1-y^2)z(z+1)$
7	$1/8x(x+1)y(y+1)z(z+1)$	21	$1/2(1-x^2)(1-y^2)z(z-1)$
8	$1/8x(x-1)y(y+1)z(z+1)$	22	$1/2(1-x^2)y(y-1)(1-z^2)$
9	$1/4(1-x^2)y(y-1)z(z-1)$	23	$1/2x(x+1)(1-y^2)(1-z^2)$
10	$1/4x(x+1)(1-y^2)z(z-1)$	24	$1/2(1-x^2)y(y+1)(1-z^2)$
11	$1/4(1-x^2)y(y+1)z(z-1)$	25	$1/2x(x-1)(1-y^2)(1-z^2)$
12	$1/4x(x-1)(1-y^2)z(z-1)$	26	$1/2(1-x^2)(1-y^2)z(z+1)$
13	$1/4x(x-1)y(y-1)(1-z^2)$	27	$(1-x^2)(1-y^2)(1-z^2)$
14	$1/4x(x+1)y(y-1)(1-z^2)$		

Table 3.1 – Shape functions for the H27 element.

3.1.2.2 Pressure/tension shape functions

The shape functions for the pressure/tension for a H8 element are trilinear. Using the node numeration shown in Figure 3.1b the shape functions are detailed in Table 3.2.

Node	N	Node	N
1	$1/8(1-x)(1-y)(1-z)$	5	$1/8(1-x)(1-y)(1+z)$
2	$1/8(1+x)(1-y)(1-z)$	6	$1/8(1+x)(1-y)(1+z)$
3	$1/8(1+x)(1+y)(1-z)$	7	$1/8(1+x)(1+y)(1+z)$
4	$1/8(1-x)(1+y)(1-z)$	8	$1/8(1-x)(1+y)(1+z)$

Table 3.2 – Shape functions for the H8 element.

3.1.2.3 Gauss points

The Gauss points coordinates and weights are detailed in Table 3.3 for complete integration and in Table 3.4 for reduced integration.

Point	x	y	z	w
1	$-\alpha$	$-\alpha$	$-\alpha$	c_1^3
2	$-\alpha$	$-\alpha$	0	$c_1^2c_2$
3	$-\alpha$	$-\alpha$	α	c_1^3
4	$-\alpha$	0	$-\alpha$	$c_1^2c_2$
5	$-\alpha$	0	0	$c_1c_2^2$
6	$-\alpha$	0	α	$c_1^2c_2$
7	$-\alpha$	α	$-\alpha$	c_1^3
8	$-\alpha$	α	0	$c_1^2c_2$
9	$-\alpha$	α	α	c_1^3
10	0	$-\alpha$	$-\alpha$	$c_1^2c_2$
11	0	$-\alpha$	0	$c_1c_2^2$
12	0	$-\alpha$	α	$c_1^2c_2$
13	0	0	$-\alpha$	$c_1c_2^2$
14	0	0	0	c_2^3
15	0	0	α	$c_1c_2^2$
16	0	α	$-\alpha$	$c_1^2c_2$
17	0	α	0	$c_1c_2^2$
18	0	α	α	$c_1^2c_2$
19	α	$-\alpha$	$-\alpha$	c_1^3
20	α	$-\alpha$	0	$c_1^2c_2$
21	α	$-\alpha$	α	c_1^3
24	α	0	α	$c_1^2c_2$
25	α	α	$-\alpha$	c_1^3
26	α	α	0	$c_1^2c_2$
27	α	α	α	c_1^3

Table 3.3 – Gauss points coordinates and weights for complete integration.

with $\alpha = \sqrt{\frac{3}{5}}$, $c_1 = \frac{5}{9}$ and $c_2 = \frac{8}{9}$.

Point	x	y	z	w
1	$-1/\sqrt{3}$	$-1/\sqrt{3}$	$-1/\sqrt{3}$	1
2	$-1/\sqrt{3}$	$-1/\sqrt{3}$	$1/\sqrt{3}$	1
3	$-1/\sqrt{3}$	$1/\sqrt{3}$	$-1/\sqrt{3}$	1
4	$-1/\sqrt{3}$	$1/\sqrt{3}$	$1/\sqrt{3}$	1
5	$1/\sqrt{3}$	$-1/\sqrt{3}$	$-1/\sqrt{3}$	1
6	$1/\sqrt{3}$	$-1/\sqrt{3}$	$1/\sqrt{3}$	1
7	$1/\sqrt{3}$	$1/\sqrt{3}$	$-1/\sqrt{3}$	1
8	$1/\sqrt{3}$	$1/\sqrt{3}$	$1/\sqrt{3}$	1

Table 3.4 – Gauss points coordinates and weights for reduced integration.

3.2 Results

Unless said otherwise only the results for the first timestep are presented. When velocity results are presented, it refers to the instantaneous velocity at the beginning of the timestep.

All computations were run with the longitudinal viscosity of the composite $\eta_L = 379\,\text{Pa.s}$ and transverse viscosity of the composite $\eta_T = 602\,\text{Pa.s}$. Those values were obtained considering the resin viscosity $\eta = 100\,\text{Pa.s}$ and a fibre volume fraction of 56.9%, using Equations (2.30) and (2.31).

The transverse viscosity is higher than the longitudinal one as given by Christensen's model, contrary to what was seen in previous papers. This means that making the fibres slide along them is easier than making them slide cross-wise, which is true when considering the sliding of one ply with respect to the other due to the fibres of one layer falling into the gaps of the other layer.

The first simulations run are not quantitatively representative of the real stack of plies, the first objective being the verification that the model retrieves qualitatively the observed phenomena. Therefore the geometry is not meant to be quantitatively compared against experimental samples.

3.2.1 Stack of unidirectional prepregs

3.2.1.1 Cross-ply stack without resin layer interface

A stack of two composite plies modelled as two layers of TIF oriented at 0° (bottom ply) and 90° (top ply) is considered, with no sliding at the interface. The height of the cube is 5mm and the thickness of each TIF layer is 2.5mm. Computation was run with the longitudinal viscosity of the composite $\eta_L = 379\,\text{Pa.s}$ and transverse viscosity of the composite $\eta_T = 602\,\text{Pa.s}$. Those values were obtained considering the resin viscosity $\eta = 100\,\text{Pa.s}$ and a fibre volume fraction of 56.9%, using Equations (2.30) and (2.31). A slip condition is applied on the top side, a no-slip condition on the bottom side and continuity of all the fields is imposed throughout the whole domain. A vertical velocity of -1 mm.s^{-1} is imposed on the top side. As seen on Figure 3.2 each layer cannot be elongated in the direction of their fibres, resulting in a blocking interface that contains fibres in the two directions and a numerical peak in the fibre tension as it is not allowing any movement as can be seen in Figure 3.4.

It can also be seen from Figure 3.2 that the bottom layer presents a velocity profile that is consistent with in-plane bending, however with a velocity that is higher in the extremities of the plies, contrary to what is observed experimentally.

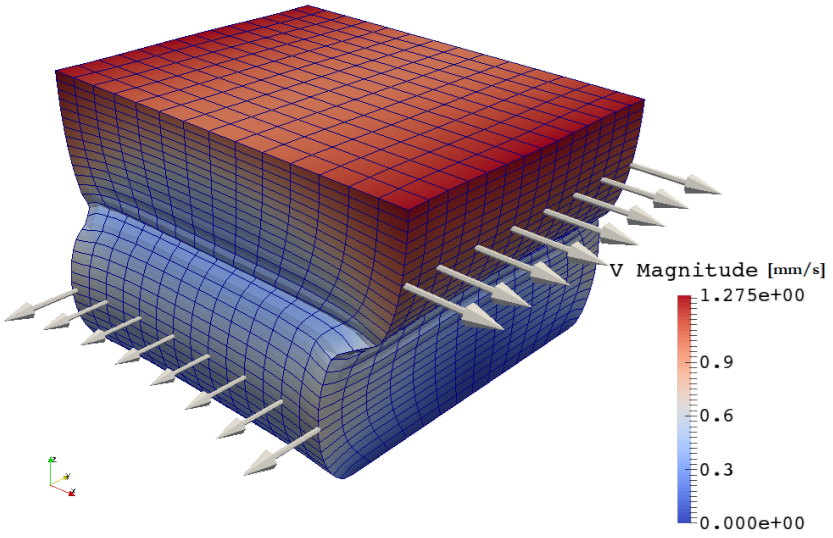

Figure 3.2 – Velocity magnitude expressed in $mm.s^{-1}$. The bottom ply is oriented at 0° and the top one at 90°.

The only remaining movement allowed for the interface is the out-of-plane bending, as can be seen in Figure 3.4, with the maximum displacement induced by the bending being equal to 75% of the displacement induced by the compression. This behaviour is not consistent with the hypothesis of plane interface made in previous works [27]. There is no indication from the experiments that such a mechanism occurs.

As can be seen in Figure 3.3, there is a resin rich layer at the interface between two UD plies. This resin rich layer need to be taken into account in the model to describe correctly the behaviour of the stack of plies.

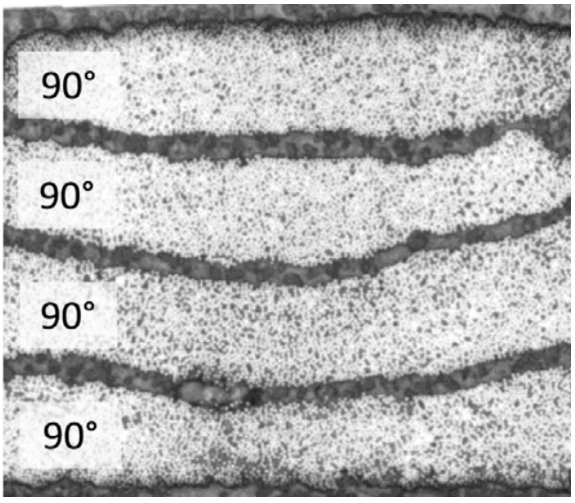

Figure 3.3 – Micrography of the thickness of a cross-ply stack. Orientation of the plies is 90°. Dark grey area represent a resin rich layer.

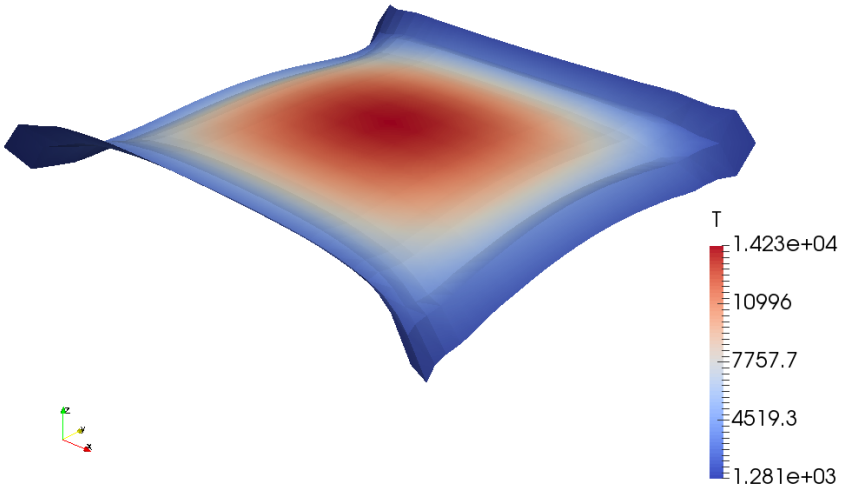

Figure 3.4 – Deformed interface corresponding to the case in Figure 3.2. A multiplicative factor of 3 was applied to the deformation to improve visualization. The fibre tension is expressed in Pa.

Moreover, it is observed experimentally that the composite layers can slide with respect to each other, this model is therefore not able to reproduce the phenomenon observed. As the 2D model is unable to describe the through-thickness behaviour, it will behave the same and is therefore not suitable.

3.2.1.2 Cross-ply stack with resin layer interface

To improve the 3D TIF model, layers of fluid are added to the previous cross-ply model as discussed in Section 3.1.1. Two layers at the tool/composite interface and one layer at the composite/composite interface are added. The middle fluid layer allows the plies to slide, and the side fluid layers allows the sliding between the plies and the tools. Modelling the interply layer as a 3D fluid layer allows to better capture the interaction between the two plies than the lubrication theory or a friction parameter, although the computational cost will greatly increase.

The cube is 5mm thick, the thickness of each TIF layer is 1mm and the thickness of each fluid layer is 1mm (3mm in total). Computation was run with the longitudinal viscosity of the composite $\eta_L = 379\,\text{Pa.s}$ and transverse viscosity of the composite $\eta_T = 602\,\text{Pa.s}$. Those values were obtained considering the resin viscosity $\eta = 100\,\text{Pa.s}$ and a fibre volume fraction of 56.9%, using Equations (2.30) and (2.31). No-slip conditions are applied on the top and the bottom sides and a vertical velocity of -1 mm.s^{-1} is imposed on the top side. Figure 3.5 shows the velocity component aligned with the fibre direction of the bottom unidirectional layer. Due to the viscous fluid layer each ply is now able to slide with respect to each other and spread transversely to the direction of their fibres. As a consequence the numerical peak in the fibre tension is greatly reduced as shown in the top interface in Figure 3.6. The bottom interface in Figure 3.6 represents the tool/composite interface, whereas the top one is the composite/composite interface. As the interfaces between the plies and the fluid are now less constrained they can elongate and they no longer bend during the transverse squeeze flow.

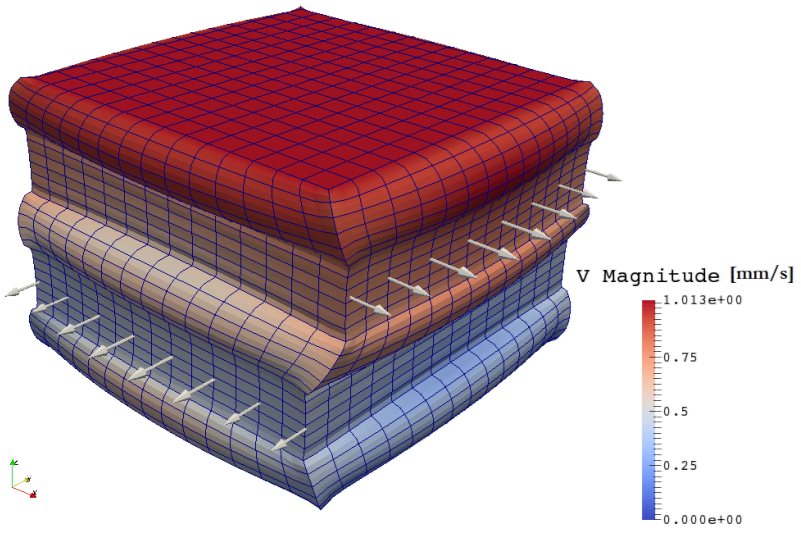

Figure 3.5 – Velocity magnitude expressed in mm.s^{-1}. The bottom ply is oriented at 0° and the top one at 90°.

As can be seen in Figure 3.5 the bottom layer presents a velocity profile that is consistent with in-plane bending, with a velocity that is higher at the center of the ply. This is more similar to the experimental observations than the results of compression without the pure resin layer at the interface.

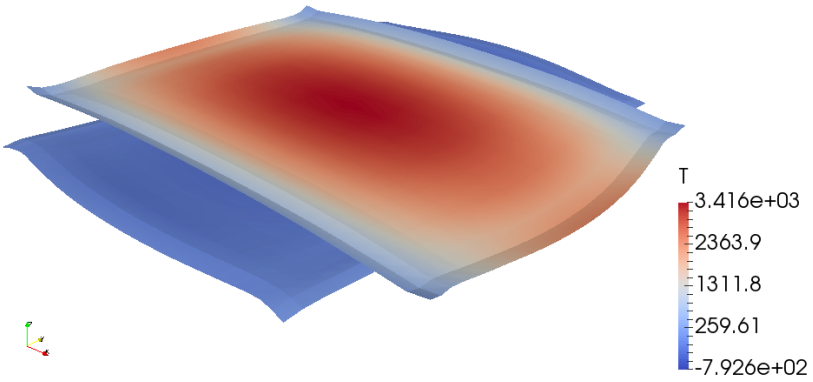

Figure 3.6 – Deformed interface corresponding to the case in Figure 3.5. The bottom interface correponds to the tool/composite interface. The top interface if the composite/composite interface. A multiplicative factor of 3 was applied to the deformation to improve visualization. The fibre tension is expressed in Pa.

As can be seen in Figure 3.5 the behaviour of the fluid layer is entirely 3D and cannot be reduced to 2D without a great loss of information, proving once more the necessity of the 3D model.

Figure 3.7 presents a comparison of the fibre tension and the velocity between the simulations with and without the explicit resin layer. Figures 3.7b and 3.7c show that the presence of the Stokes layer dampens greatly the peak in the fibre tension and reduces the pressure. Figure 3.7a shows that the inextensibility is verified in each ply, and that the Stokes layer accomodates the velocity of each adjacent ply, effectively relieving the coupling between them.

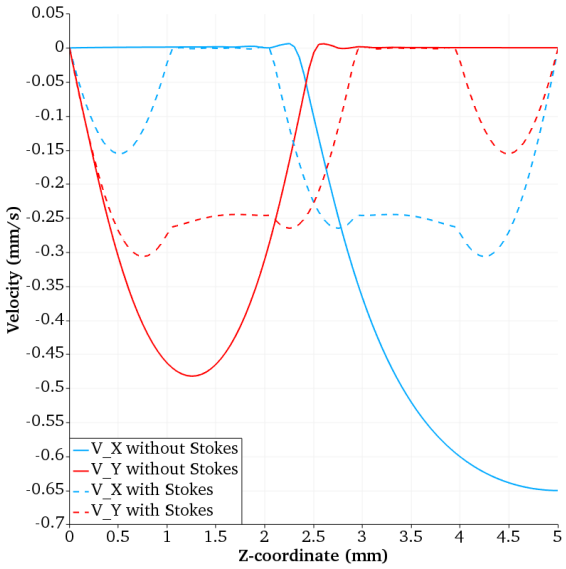

(a) Values of the velocity in mm.s^{-1}.

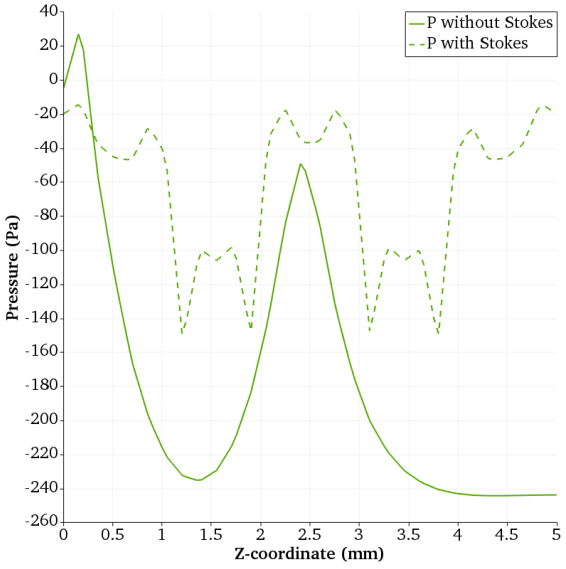

(b) Values of the pressure in Pa.

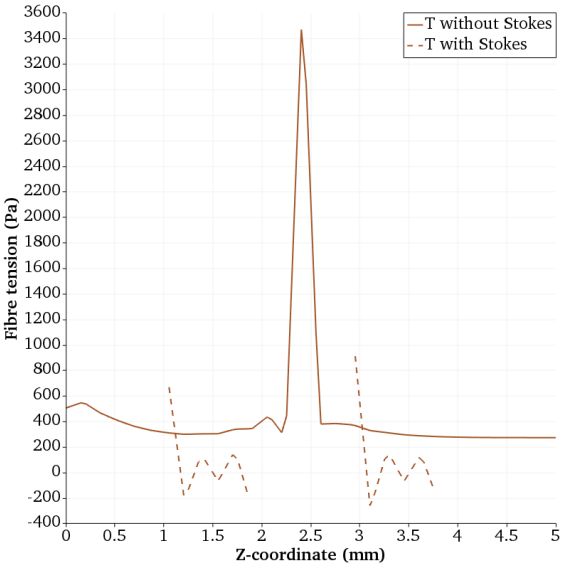

(c) Values of the fibre tension in Pa.

Figure 3.7 – Comparison between the simulation with and without the explicit Stokes layer interface. Values are taken along the line (x = 0.5mm, y=0.5mm).

3.2.1.3 [30/-30] stack with resin layer interface

A stack of two composite plies modelled as two layers of TIF oriented at 30° and -30°, with layers of fluid is considered. The height of the cube is 5mm, the thickness of each TIF layer is 1mm and the thickness of each fluid layer is 1mm.Computation was run with the longitudinal viscosity of the composite $\eta_L = 379$ Pa.s and transverse viscosity of the composite $\eta_T = 602$ Pa.s. Those values were obtained considering the resin viscosity $\eta = 100$ Pa.s and a fibre volume fraction of 56.9%, using Equations (2.30) and (2.31). No-slip conditions are applied on the top and the bottom sides and a vertical velocity of -1 mm.s^{-1} is imposed on the top side.

Experimental observations revealed that alternate layers inclined at an angle different from 90° tend to rotate when they are subjected to compression. The computed velocity field for the first time step in [27] suggested the same behaviour. Some parametric studies achieved here show that the magnitude of rotation depends on the enforced thickness reduction and the rheological properties of both the composite and resin layers. It is then mandatory to compute the full compression through all the timesteps to determine the final deformation of the composite, as shown for instance in Figure 3.8. The ply re-orientation cannot be predicted correctly without the combination of the TIF model and the presence of the fluid layer between the plies.

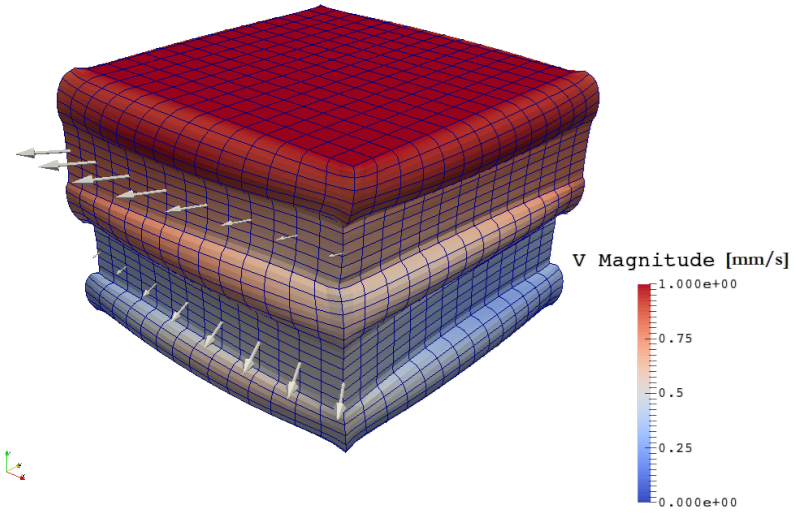

Figure 3.8 – Velocity magnitude expressed in $mm.s^{-1}$. The bottom ply is oriented at 30° and the top one at -30°.

As mentioned in Chapter 1 solid rotation is not the only occurring phenomenon, as can be seen on Figure 3.9 the ply is also subject to in-plane shear and in-plane bending, although this deformation is somehow hindered by the presence of the fibres.

Figure 3.9 presents the decomposition of the velocity field, projected in the plane, taken in the middle of the bottom ply. On Figure 3.9a the spreading, i.e. the velocity orthogonal to the fibre direction, is shown. The further from the center, the higher the spreading is, which is consistent with a squeeze flow orthogonal to the fibre direction. On Figure 3.9b the rest of the velocity field is shown, and it can be seen that it is a combination of solid body rotation and in-plane bending.

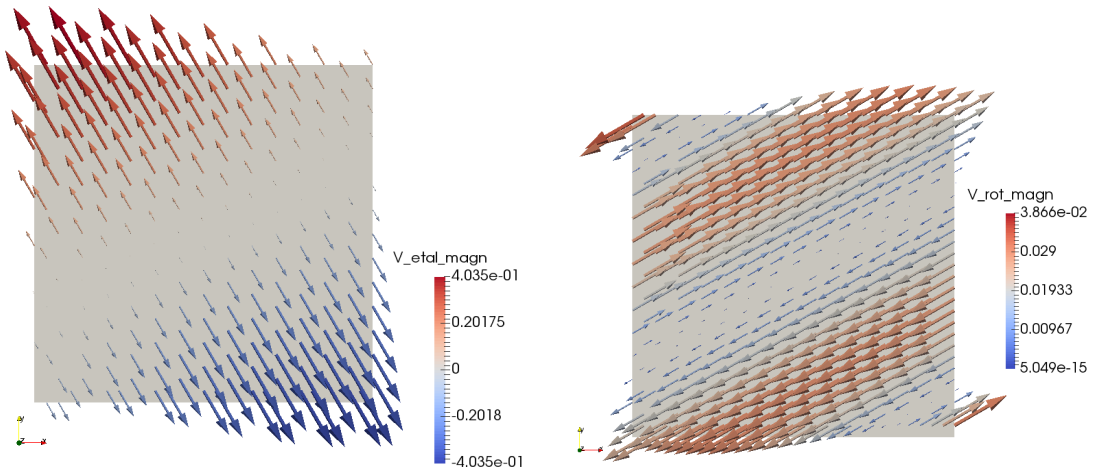

(a) Spreading velocity.

(b) Rotation velocity.

Figure 3.9 – Decomposition of the velocity field in the middle of the lower ply. The velocity is expressed in mm.s^{-1}.

3.2.1.4 Single UD ply with thickness variation of the fluid layer

Due to the variability of the prepreg material, it is very common to see thickness variation of the resin layer. In these situations it is observed that a discontinuous ply will be washed away when subjected to compression.

A single unidirectionnal ply modelled as a layer of TIF oriented at 0° with two layers of fluid is considered. The base dimensions of the cube are 3mm, the thickness of the TIF and resin layer is 1mm and the extra height on the right hand side of the computational domain is 1mm. Computation was run with the longitudinal viscosity of the composite $\eta_L = 379\,\text{Pa.s}$ and transverse viscosity of the composite $\eta_T = 602\,\text{Pa.s}$. Those values were obtained considering the resin viscosity $\eta = 100\,\text{Pa.s}$ and a fibre volume fraction of 56.9%, using Equations (2.30) and (2.31). No-slip conditions are applied on the top and the bottom sides and a vertical velocity of -1 mm.s^{-1} is imposed on the top side. The inclination is along the direction of the fibres.

As presented on Figure 3.10 the TIF layer slides along the fibre direction when subjected to transverse compression. The initial undeformed mesh is displayed in the figures to better show the displacement of the TIF layer.

Figure 3.10b shows the deformed mesh for the tenth time step, proving that the method does not suffer from numerical instabilities in the velocity field. This is also true for the pressure and the fibre tension fields. It is recalled here that nor stabilization method nor implicit update is used to obtain these results.

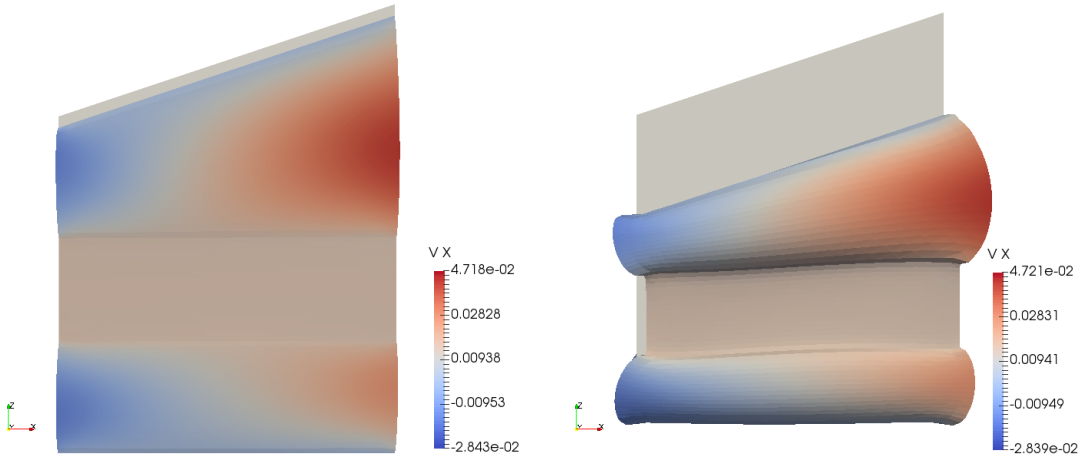

(a) First time step.

(b) Tenth time step.

Figure 3.10 – Velocity component along the fibre direction. The horizontal velocity is expressed in mm.s^{-1}. The plain geometry represents the undeformed shape.

3.2.1.5 Two UD plies subjected to bending under the self-weight

Bending properties are required to simulate the forming of composite prepregs when using a finite element approach based on shell elements. Moreover, it has been shown that bending stiffness of prepreg is not directly related to its in-plane tensile modulus like continuous material structure due to relative sliding between fibres and/or plies [28]. Among all possible ways to measure the bending properties of viscous prepregs, the cantilever test method is usually preferred because of its simplicity and flexibility. It is the reason why bending stiffness is determined by experimental method. It would be of great interest to perform this characterization numerically as it would reduce the time and the cost of the characterization of new materials or new temperature ranges, as well as giving parameters that can be put directly in the model without the need for further identification.

A stack of two unidirectionnal plies modelled as two layers of TIF oriented at 0° is considered, separated by a pure resin layer.

The test case presented here is motivated by the observation that the transverse shear deformation of a viscous laminate experienced during forming is the result of interply slip. This latter can be modelled by transverse shear deformation of the laminate using the Mindlin plate theory [29], [30] for instance. For such a model, the behaviour of the transverse shear deformation of the laminate must be related to the behaviour of interply slip, which is controlled by the viscous properties of the pure resin layer. The dimensions of the parallelepiped is 0.57x0.57 mm^2 for the base and 2mm for the length. The thickness of each TIF layer is 0.26mm and the thickness of the Stokes layer is 0.05mm. Computation was run with the longitudinal viscosity of the composite $\eta_L = 379\,\text{Pa.s}$ and transverse viscosity of the composite $\eta_T = 602\,\text{Pa.s}$. Those values were obtained considering the resin viscosity $\eta = 100\,\text{Pa.s}$ and a fibre volume fraction of 56.9%, using Equations (2.30) and (2.31). A no slip condition is applied on the left side and all the domain is subjected to gravity. Continuous interpolation was used for the pressure and the fibre tension, simulation time is $t_{max} = 15\text{s}$ and the timestep is $\delta t = 0.5\text{s}$. Figure 3.11 presents the X-axis velocity, Figure 3.12 the Y-axis velocity, Figure 3.13 the Z-axis velocity, Figure 3.14 the pressure and Figure 3.15 the fibre tension at $t = 5\text{s}$, $t = 10\text{s}$ and $t = 15\text{s}$.

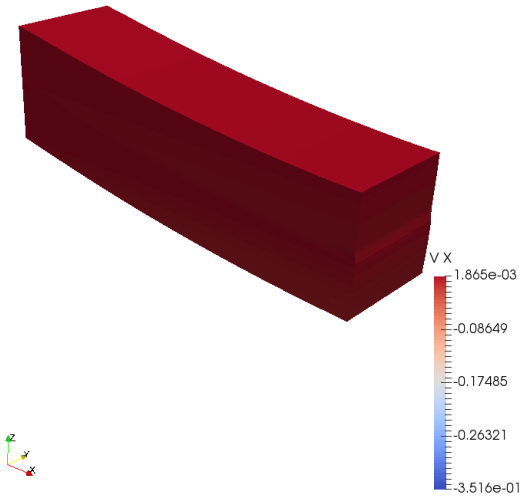

(a) X-axis velocity (mm.s^{-1}) at 5s (10^{th} timestep). The fixed end is on the top left.

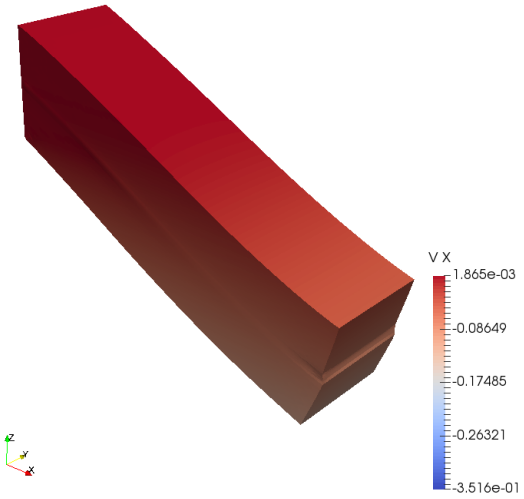

(b) X-axis velocity (mm.s^{-1}) at 10s (20^{th} timestep).

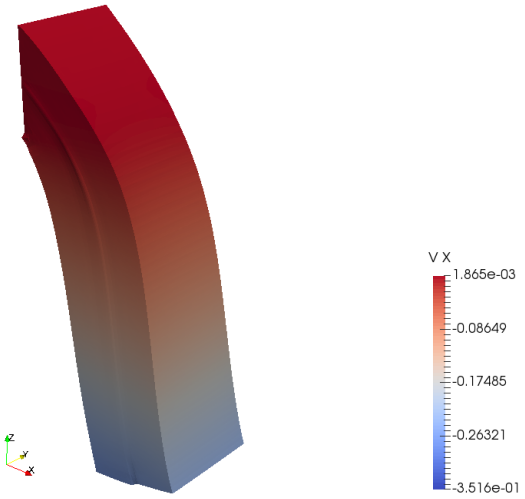

(c) X-axis velocity (mm.s^{-1}) at 15s (30^{th} timestep).

Figure 3.11 – X-axis velocity for the bending of two UD plies, dynamic simulation. Maximum deflection of the composite plies is 61°.

As can be seen in Figure 3.11 the results present a transitional phase when the fluid first falls (Figure 3.11a), then is pulled by the fibres when the inextensibility is propagated from the blocked side (Figure 3.11b) to finally reach an equilibrium state (Figure 3.11c). This equilibrium is not physical, as such a stack of plies would not reach a vertical position. This is due to the fluid behaviour of the material which is purely viscous, and does not account for the elasticity of the fibres. It can be seen in Figure 3.11c that the inextensibility of each layer induces the shearing of the pure resin layer, which leads to a staircase profile of the TIF layers that can be seen in Figure 3.16, as can be expected.

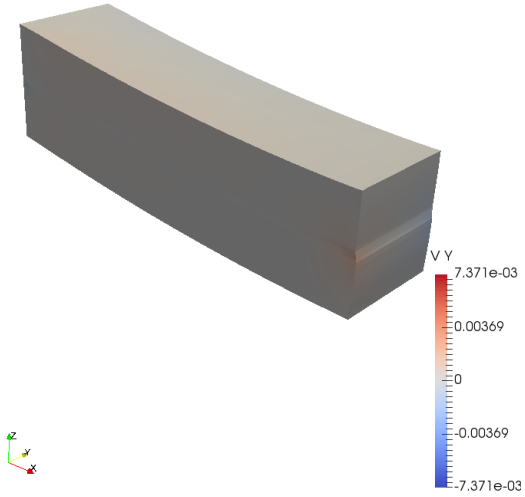

(a) Y-axis velocity (mm.s^{-1}) at 5s (10^{th} timestep).

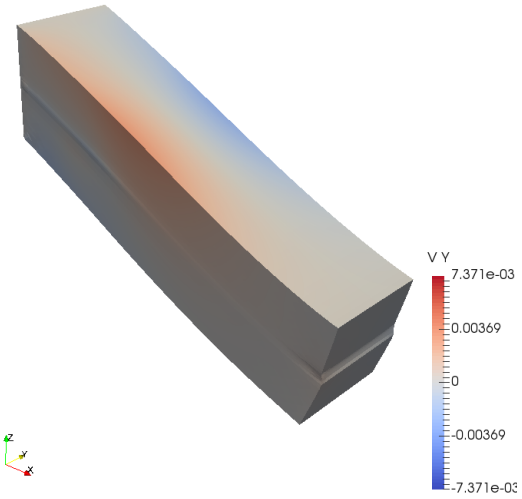

(b) Y-axis velocity (mm.s^{-1}) at 10s (20^{th} timestep).

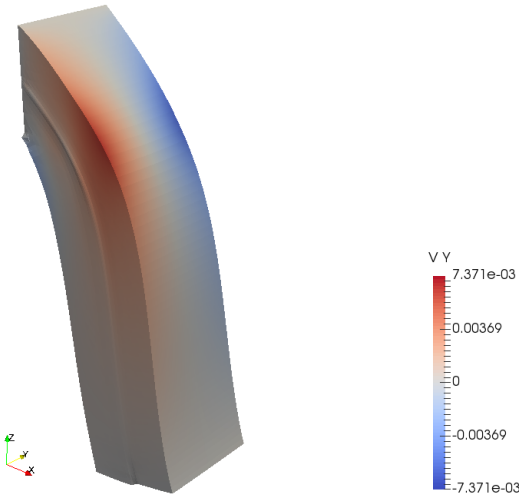

(c) Y-axis velocity (mm.s^{-1}) at 15s (30^{th} timestep).

Figure 3.12 – Y-axis velocity for the bending of two UD plies, dynamic simulation.

It can be seen in Figure 3.15 that the TIF layers are subjected to pulling and compression, therefore area with risk of buckling can be easily identified by the use of the TIF model.

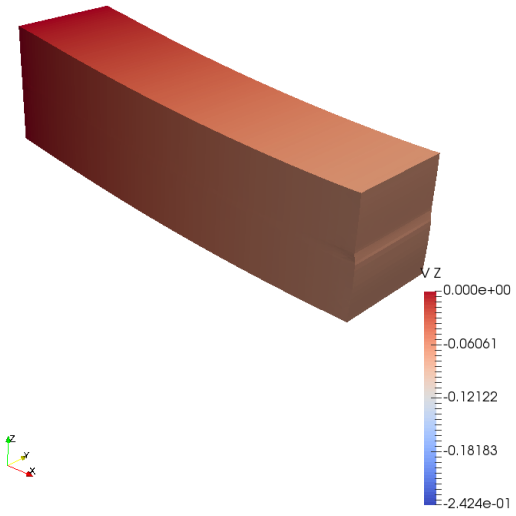

(a) Z-axis velocity (mm.s^{-1}) at 5s (10^{th} timestep).

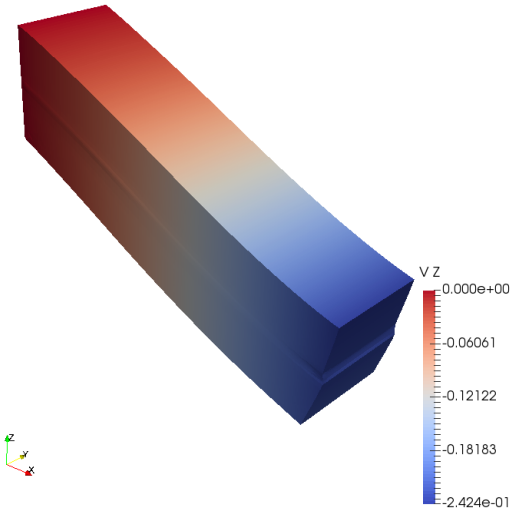

(b) Z-axis velocity (mm.s^{-1}) at 10s (20^{th} timestep).

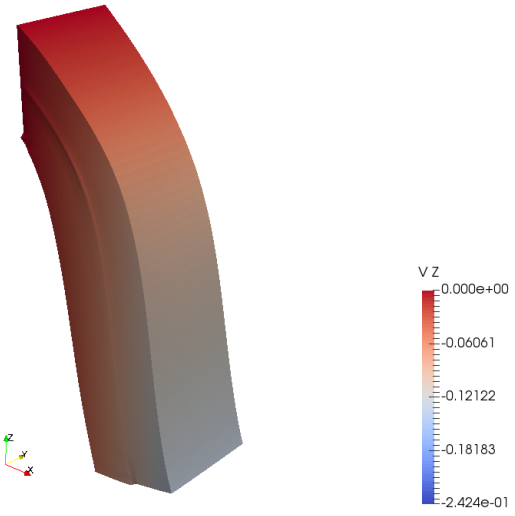

(c) Z-axis velocity (mm.s^{-1}) at 15s (30^{th} timestep).

Figure 3.13 – Z-axis velocity for the bending of two UD plies, dynamic simulation.

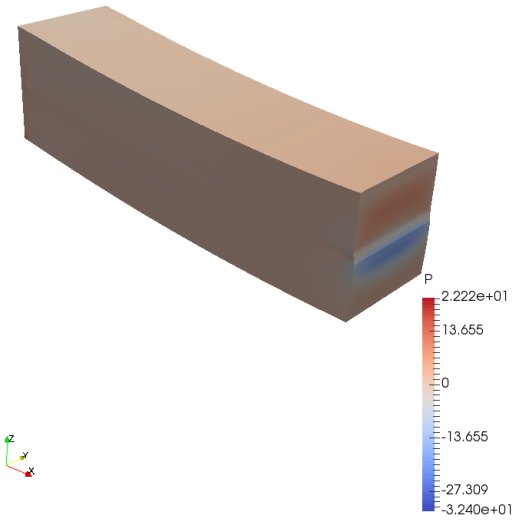

(a) Relative pressure (Pa) at 5s (10^{th} timestep).

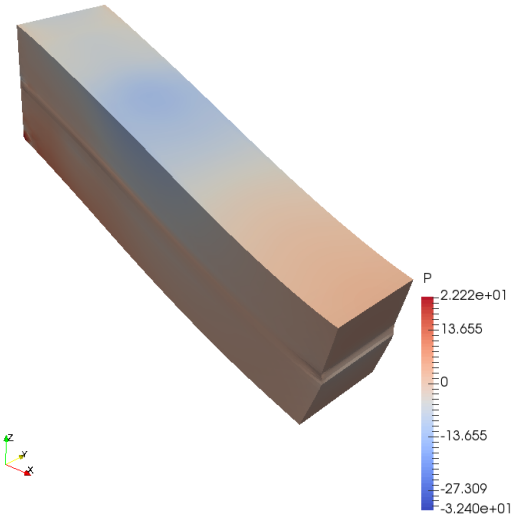

(b) Relative pressure (Pa) at 10s (20^{th} timestep).

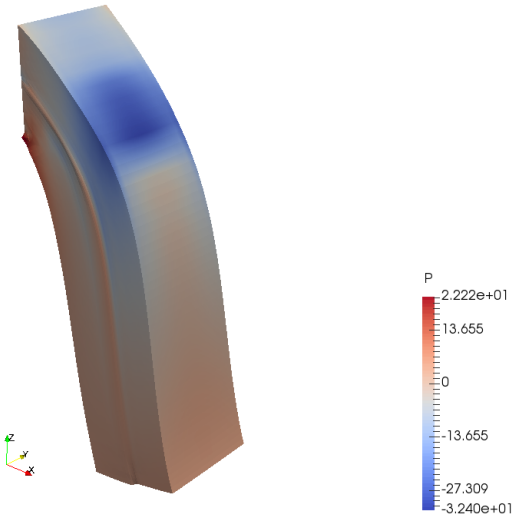

(c) Relative pressure (Pa) at 15s (30^{th} timestep).

Figure 3.14 – Relative pressure for the bending of two UD plies, dynamic simulation.

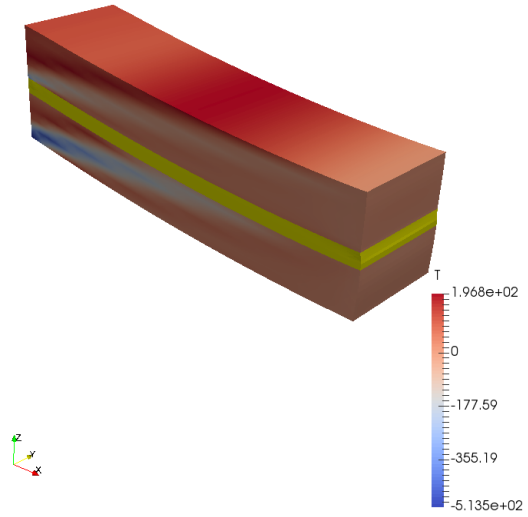

(a) Fibre tension (Pa) at 5s (10^{th} timestep).

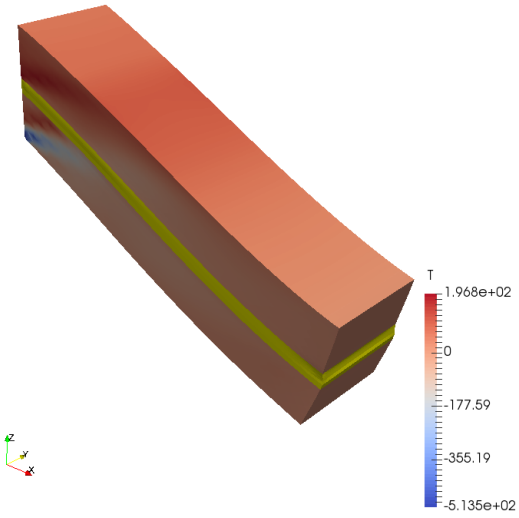

(b) Fibre tension (Pa) at 10s (20^{th} timestep).

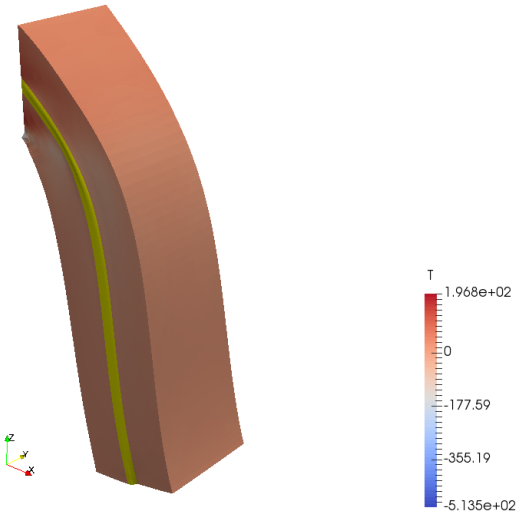

(c) Fibre tension (Pa) at 15s (30^{th} timestep).

Figure 3.15 – Fibre tension for the bending of two UD plies, dynamic simulation. Yellow areas represent the domain where the fibre tension is not defined, in this case in the pure resin layer.

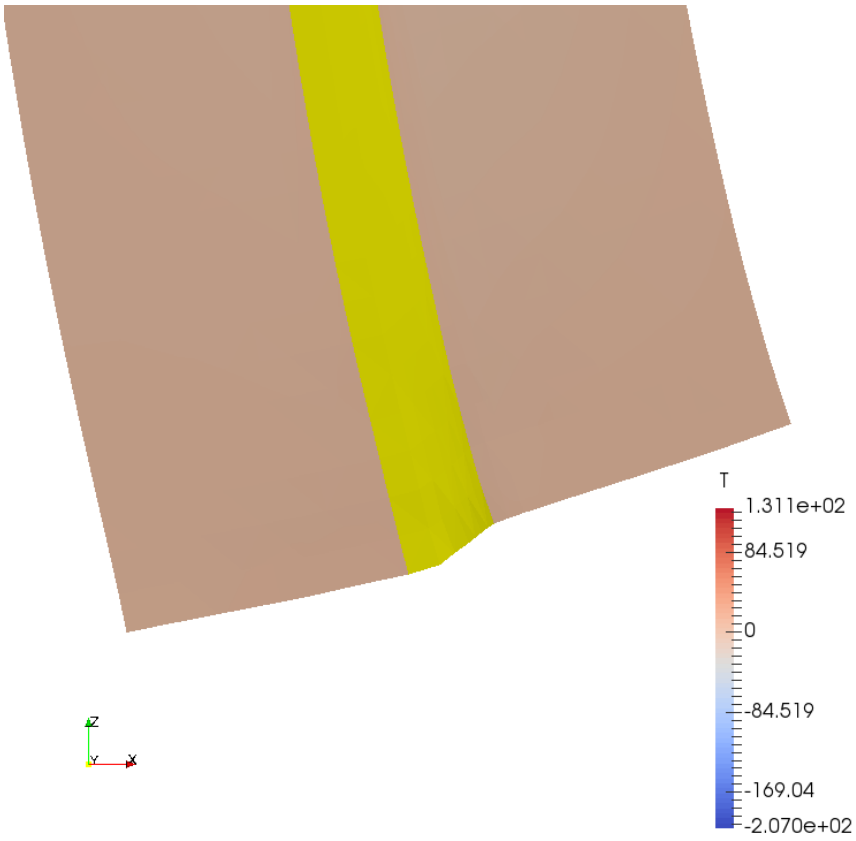

Figure 3.16 – Details of the unheld edge of the stack, the staircase profile can be clearly seen as the different layers are not aligned. Yellow areas represent the domain where the fibre tension is not defined, in this case in the pure resin layer.

3.2.1.6 Comparison with experiment

The objective is now to quantitatively compare the simulation results with the experimental observations. Due to the dimensions of the prepreg material, a finer mesh is required in the thickness.

The modelled stack consists of two layers of TIF of 0.78mm each surrounded by layers of Stokes of 0.04mm each, corresponding approximately to 5% of the composite layer thickness. The initial orientation of the bottom layer is 30° and the initial orientation of the top layer is -30°. Computation was run with the longitudinal viscosity of the composite $\eta_L = 379\,\text{Pa.s}$ and transverse viscosity of the composite $\eta_T = 602\,\text{Pa.s}$. Those values were obtained considering the resin viscosity $\eta = 100\,\text{Pa.s}$ and a fibre volume fraction of 56.9%, using Equations (2.30) and (2.31). Due to the use of FEM, the entire stack cannot be computed with a sufficient accuracy on the results due to the computational cost. The simulations were therefore carried out on an area of interest in the middle of the stack. In this case the area of interest is a cube of dimension 1.7mm. The effect of the scale up to the real size of the ply will need to be assessed, but it will first require a method that would make such a computation at the reach of modern computers.

Figure 3.17 presents the deformation of the middle of the TIF layer, were it is shown that there is a solid body rotation of 2.35° between the two plies. Comparison between the numerical and experimental values is given in Table 3.5.

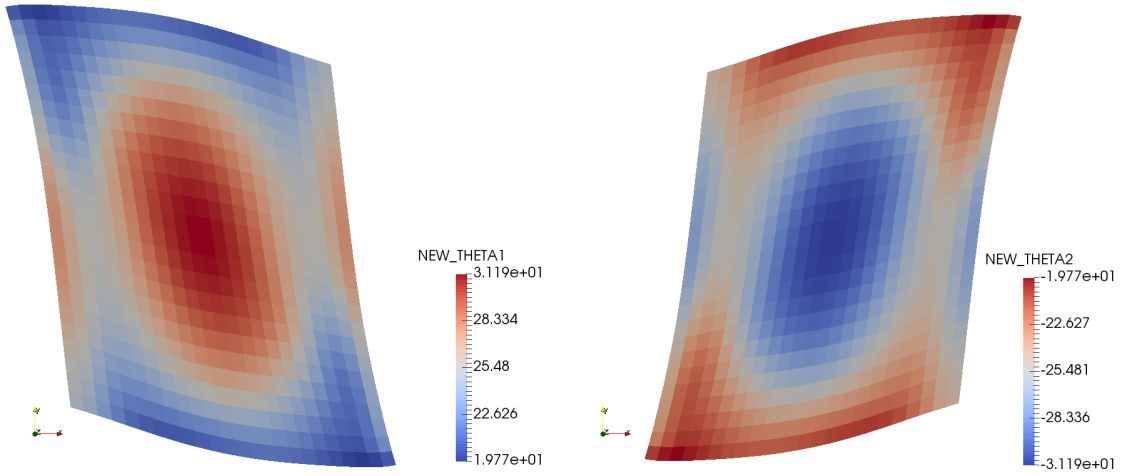

(a) Bottom layer, initially at 30°.

(b) Top layer, initially at -30°.

Figure 3.17 – Deformed geometry of the middle of the TIF layers. The angle is expressed in °.

	Experimental	Numerical
Solid body rotation	8 - 10°	2.34°
Spreading	13 - 16%	14%

Table 3.5 – Comparison between the experimental and the numerical values for the [30/-30] stack.

The differences between the experimental and the numerical values can arise from various origins:

- The assumption was made that the pure resin layer represented 5% of the TIF thickness, and that it is of constant thickness. This is not always verified in industrial prepregs, and the thickness might be not constant in the same sample and might change from one sample to another. It was presented in Section 3.2.1.4 that an heterogeneity in the thickness of the resin layer have an impact that cannot be neglected.
- The resin viscosity was taken from the manufacturer datasheet, and the TIF viscosities calculated using Christensen's semi-empirical model presented in [26]. The actual homogenized viscosity of the ply may vary from one sample to another, and Christensen's model gives accurate results considering the material is homogeneous at the scale of the part, which it may not be at the scale of the ply.
- The experimental values are calculated from the displacement of the copper tracers which position in the thickness of the interfacial layer is not perfectly controlled. It is worth to note they are located in-between the composite layers and not inside them, which could change the results.
- The values are retrieved from a simulation run on a volume of interest in the middle of the sample. A sensitivity study is presented in Section 3.2.1.7, which combined with the fact that the material used is of industrial grade lead to variations of the solution that might be important.

3.2.1.7 Sensitivity study

To assess the impact of the parameters of the model on the results, a sensitivity study has been performed. The viscosity was changed by ± 20% and the thickness of the Stokes layers by ± 10%.

As the material is linear viscous, and the boundary conditions are Dirichlet boundary conditions, the change of viscosity does not impact the velocity field, therefore the rotation and spreading retrieved are not impacted.

Table 3.6 presents the impact of the thickness of the Stokes layers on the rotation and the spreading, in which it can be seen that the results are very sensitive to the thickness. This sensitivity explains the differences between the experimental and the numerical values, as the material used is of industrial grade and therefore contains inherent structural variation, such as the average and the geometrical distribution of the thickness.

Variation of the thickness of the Stokes layers	+10%	-10%
Variation of the rotation	-22%	+26%
Variation of the spreading	-21%	+14%

Table 3.6 – Results of the sensitivity study

The sensitivity also proves the importance of the Stokes layers, as well as the necessity of a fine and precise information on the initial structure of the material.

3.2.2 Stack of woven prepregs

In order to compare the model to the experimental observations, simulations were carried out on the test specimens described in Sections 1.3.1, 1.3.2 and 1.3.4.2. To model the woven ply, two TIF layers were stacked without an interfacial resin layer to introduce the two fibre directions, with a ratio of thickness chosen so as to respect the warp/weft ratio of the woven prepreg. The behaviour of the woven ply is assimilated to the behaviour of the interface between the two TIF layers.

This representation is unable to take into account the direct interaction between the two fibre directions. However, the in-plane shear energy of a dry woven fabric before its locking is very small compared to the energy of the squeeze flow and rotation of viscous prepreg laminate, therefore this assumption is thought to be reasonable.

Due to the use of 3D FEM, the entire stack cannot be computed with a sufficient accuracy on the results due to the computational cost. The simulations were therefore carried out on an area of interest in the middle of the stack, corresponding to points F and G in the first specimen recalled in Figure 3.18a and to points A, B, C, D and E in the second specimen recalled in Figure 3.18b. The number of elements in the plane is 24 x 24, and 49 in the thickness to obtain a sufficient accuracy without degrading the conditioning of the system, leading to a total of 28 224 elements and 775 597 degrees of freedom.

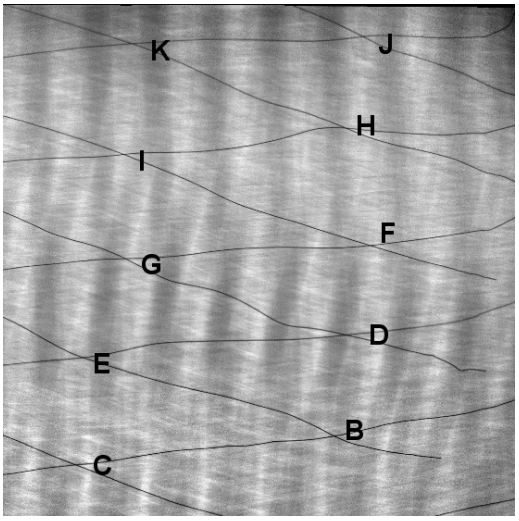

(a) [0/20/0] stack of Vizilon™ SU75G1 after compression.

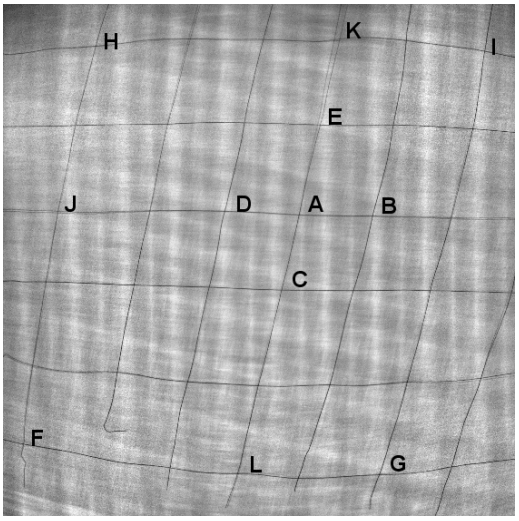

(b) [0/80/0] stack of Vizilon™ SU75G1 after compression.

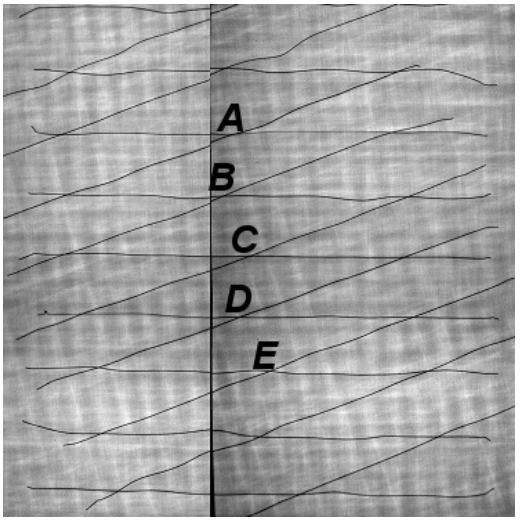

(c) [0/20/0] stack of Vizilon™ SB75G1 after compression.

Figure 3.18 – Recall of the experiments for comparison with the numerical simulation.

3.2.2.1 [0/20/0] stack of unbalanced prepreg with resin layer interface

The first test specimen was modelled as six layers of TIF grouped two by two, as can be seen in Figure 3.19. The bottom and top layers consist of a layer oriented at 0° of thickness 0.3mm and a layer oriented at 90° of thickness 1.1mm to represent the 4/1 volumetric fraction of fibre orientation in the woven fabric. With the same ratio, the middle layers consist of a layer oriented at 20° of thickness 0.3mm and a layer oriented at -70° of thickness 1.1mm. The orientation of -70° was prefered over 110° for numerical considerations, the fibre reorientation being computed based on the velocity gradient which tends to be unstable. A smaller angle value reduces the instability. The length of each side of the cube is 5mm. A pure resin layer is introduced to model the inter-ply resin-rich on either side of a prepreg sheet. Computation was run with the longitudinal viscosity of the composite $\eta_L = 379\,\text{Pa.s}$ and transverse viscosity of the composite $\eta_T = 602\,\text{Pa.s}$. Those values were obtained considering the resin viscosity $\eta = 100\,\text{Pa.s}$ and a fibre volume fraction of 56.9%, using Equations (2.30) and (2.31).

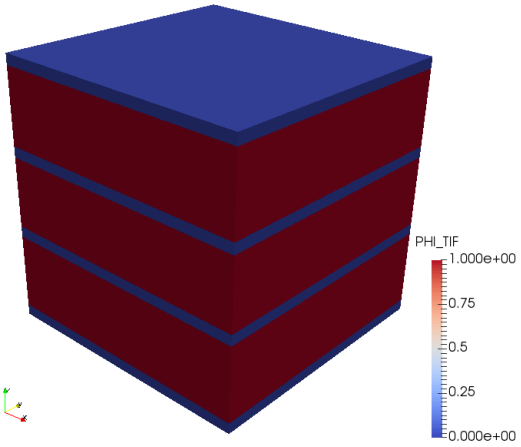

Figure 3.19 – Model of the [0/20/0] specimen. In red (thick layer) are the TIF layers and in blue (thin layer) the resin layers.

As can be seen in Figure 3.20 a solid body rotation appears when the stack is subjected to compression, which is consistent with what was observed experimentally. The values were extracted from the interface between the two TIF for each of the three layers, as it contains both fibre direction. The comparison between the numerical and the experimental values is presented in Table 3.7, where it is seen that the numerical model is in reasonable agreement with the experimental measurements. The difference can be explained by the stacking of two unidirectional plies to model a woven fabric ply. The solid body rotation is predicted correctly, but this model lacks a bit of accuracy when predicting the angle values for an initial orientation of 20°. Considering that the proper woven prepreg model using a fluid approach has not been developed yet, the double TIF layer is found to be a fairly good approach to model the solid body rotation of the woven fabric.

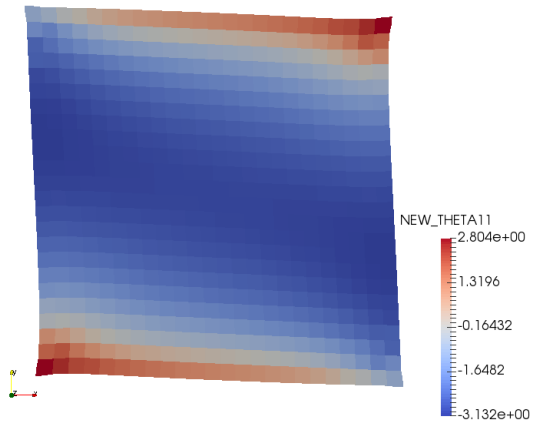

(a) Bottom layer.

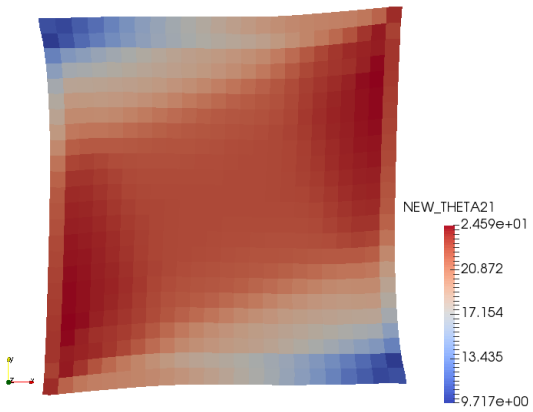

(b) Middle layer.

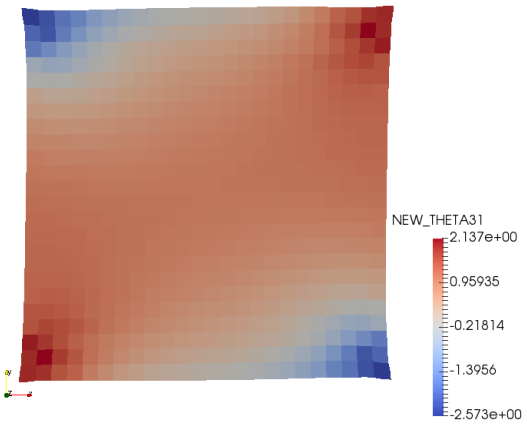

(c) Top layer.

Figure 3.20 – Comparison of the deformed interfaces for the [0/20/0] specimen. Angles are expressed in °.

Case	Initial angle (°)	Final angle (°)	Difference (°)
Experimental	20	25.6	5.6
Bottom layer - Middle layer	20	23.494	3.494
Top layer - Middle layer	20	18.809	-1.191
Numerical total	2.303		

Table 3.7 – Computed angles for a 20° initial orientation. Comparison between experimental and numerical values. The total numerical value is the sum of the computed differences.

3.2.2.2 [0/80/0] stack of unbalanced prepreg with resin layer interface

The second test specimen was modelled as six layers of TIF grouped two by two, as can be seen in Figure 3.19, just as the first specimen. The bottom and top layers consist of a layer oriented at 0° of thickness 0.3mm and a layer oriented at 90° of thickness 1.1mm to represent the 4/1 volumetric fraction of fibre orientation in the woven prepreg. With

the same ratio, the middle layers consist of a layer oriented at 80° of thickness 0.3mm and a layer oriented at -10° of thickness 1.1mm. The orientation of -10° was prefered over 170° for the numerical reason previously mentioned. The length of each side of the cube is 5mm. In the same manner as the previous specimen, a resin layer is introduced between the prepreg layers. Computation was run with the longitudinal viscosity of the composite $\eta_L = 379\,\text{Pa.s}$ and transverse viscosity of the composite $\eta_T = 602\,\text{Pa.s}$. Those values were obtained considering the resin viscosity $\eta = 100\,\text{Pa.s}$ and a fibre volume fraction of 56.9%, using Equations (2.30) and (2.31).

As can be seen in Figure 3.21 a solid body rotation occurs when the stack is subjected to compression, just as with the previous specimen. The values were extracted from the interface between the two TIF for each of the three layers, as it contains both fibre direction. The comparison between the numerical and the experimental values is presented in Table 3.8. The numerical predictions match fairly well the experimental observations. Again the difference can be explained by the stacking of two unidirectional plies to model a woven fabric ply.

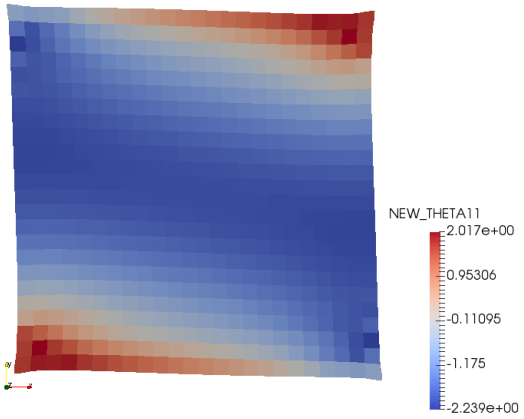

(a) Bottom layer.

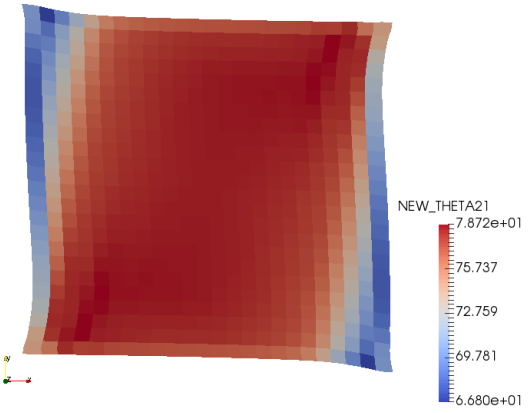

(b) Middle layer.

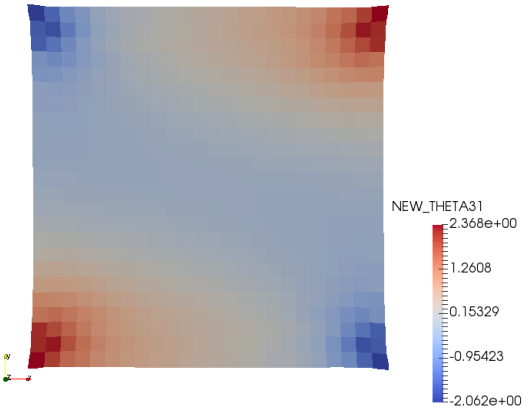

(c) Top layer.

Figure 3.21 – Comparison of the deformed interfaces for the [0,80,0] specimen. Angles are expressed in °.

Case	Initial angle (°)	Final angle (°)	Difference (°)
Experimental	80	76.86	-3.14
Bottom layer - Middle layer	80	80.387	0.387
Top layer - Middle layer	80	78.687	-1.313
Numerical total	-0.926		

Table 3.8 – Computed angles for a 80° initial orientation. Comparison between experimental and numerical values. The total numerical value is the sum of the computed differences.

It is worth to note that the experimental observations showed that the [0/20/0] stack opens and that the [0/80/0] stack closes, and that this behaviour is predicted correctly by the TIF model.

3.2.2.3 [0/20/0] stack of balanced prepreg with resin layer interface

The third test specimen was modelled as six layers of TIF grouped two by two, as can be seen in Figure 3.19, just as the two first specimens. The bottom and top layers consist of a layer oriented at 0° of thickness 0.7mm and a layer oriented at 90° of thickness 0.7mm to represent the 1/1 volummetric fraction of fibre orientation in the woven prepreg. With the same ratio, the middle layers consist of a layer oriented at 20° of thickness 0.7mm and a layer oriented at -70° of thickness 0.7mm. The orientation of -70° was prefered over 110° for the numerical reason previously mentioned. The length of each side of the cube is 5mm. In the same way as the previous specimen, a resin layer is introduced between the prepreg layers and in the extremities. Computation was run with the longitudinal viscosity of the composite $\eta_L = 379\,\text{Pa.s}$ and transverse viscosity of the composite $\eta_T = 602\,\text{Pa.s}$. Those values were obtained considering the resin viscosity $\eta = 100\,\text{Pa.s}$ and a fibre volume fraction of 56.9%, using Equations (2.30) and (2.31).

As can be seen in Figure 3.22 a solid body rotation occurs in the numerical model when the stack is subjected to compression, even though this phenomenon does not exist in the experimental observations. The angle values were extracted from the interface between the two TIF for each of the three layers, as it contains both fibre directions. The comparison between the numerical and the experimental values is presented in Table 3.9.

Case	Initial angle (°)	Final angle (°)	Difference (°)
Experimental	20	20.52	0.52
Bottom layer - Middle layer	20	25.7	5.7
Top layer - Middle layer	20	21.776	1.776
Numerical total	7.476		

Table 3.9 – Computed angles for a 20° initial orientation for the balanced specimen. Comparison between experimental and numerical values. The total numerical value is the sum of the computed differences.

From the results presented in Table 3.9 it can be seen that the TIF model is not accurate when used to model a layer of balanced woven fabric. It can be concluded that the real flow must be too complex to be retrieved by the TIF model, and that the interweaving effect must be taken into account in order for the model to be accurate.

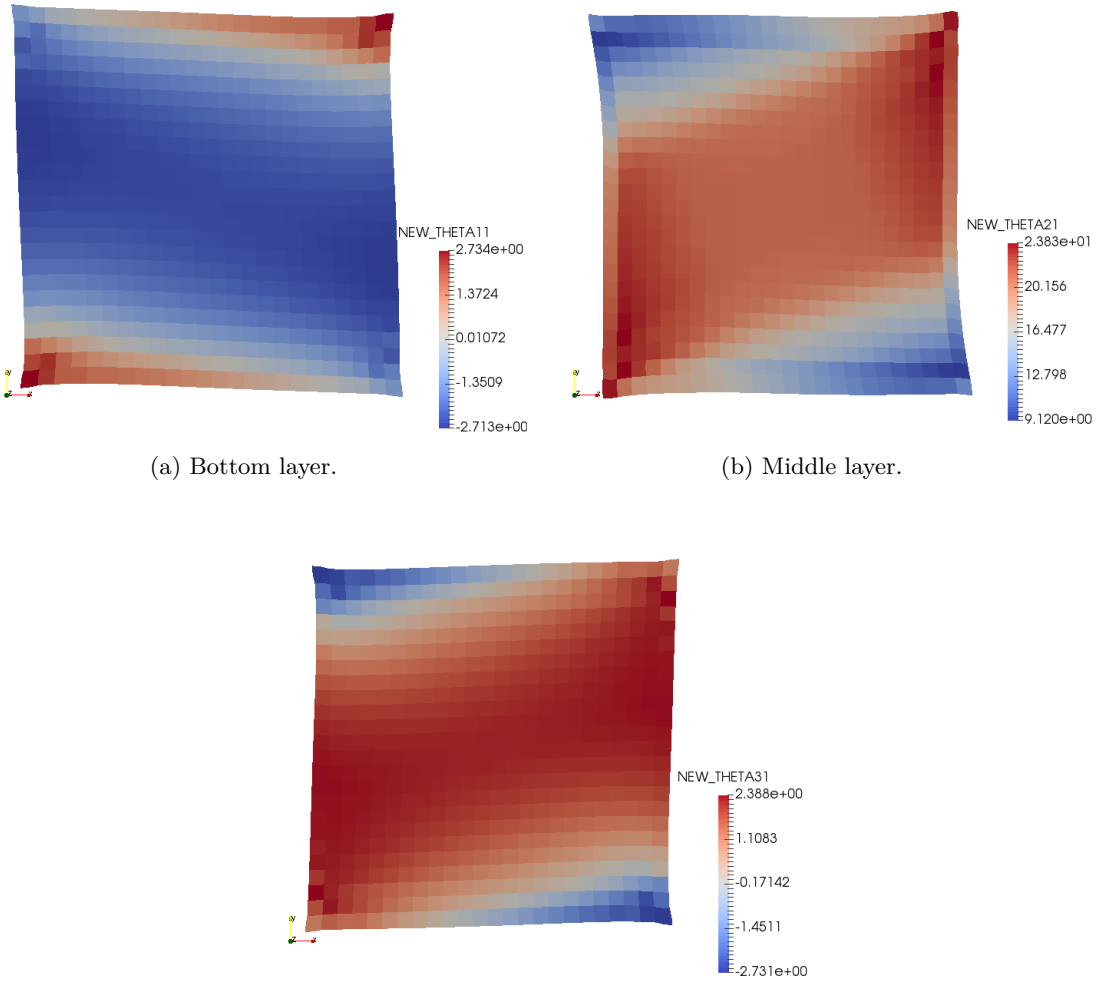

(a) Bottom layer.

(b) Middle layer.

(c) Top layer.

Figure 3.22 – Comparison of the deformed interfaces for the [0/20/0] balanced specimen. Angles are expressed in °.

Conclusion

This chapter presented an unified heterogeneous TIF/Stokes model that is able to take into account the resin rich layer at the interface between plies, which existence was experimentally demonstrated.

The importance of this resin rich layer was then numerically shown through the resolution of a compression problem of a stack without, then with a pure resin layer. The computation without the pure resin layer led to results that were not physical, whereas the computation with the pure resin layer led to results that were much closer the experimental observations.

The developped model was then employed to solve the compression of a [30/-30] stack, on a single layer of composite surrounded by Stokes layers with heterogeneous thickness to verify the ability of the model to simulate the sliding of a ply, then on a stack of two UD plies subjected to self-weight. This last case shown a limit of the model, as the behaviour of the material is purely viscous and does not take into account the elasticity of the fibres, leading to a non-physical equilibrium state. A sliding between the two plies was however retrieved.

The model was then used to simulate the compression of a stack of woven prepregs. It was shown that such a model is not able to represent correctly the flow of the real material, and it can be concluded that a model specific for the woven fabric must be developped within a fluid framework to give accurate results on this kind of computation.

References

[26] R. M. Christensen, "Effective viscous flow properties for fiber suspensions under concentrated conditions", *Journal of Rheology*, vol. 37, no. 1, pp. 103–121, Jan. 1993. DOI: 10.1122/1.550459 (cit. on pp. 41, 100).

[27] C. Ghnatios, E. Abisset-Chavanne, C. Binetruy, F. Chinesta, and S. Advani, "3d modeling of squeeze flow of multiaxial laminates", *Journal of Non-Newtonian Fluid Mechanics*, vol. 234, pp. 188–200, 2016 (cit. on pp. 85, 90, 126).

[28] W. R. Yu, M. Zampaloni, F. Pourboghrat, K. Chung, and T. J. Kang, "Analysis of flexible bending behavior of woven preform using non-orthogonal constitutive equation", *Composites Part A: Applied Science and Manufacturing*, vol. 36, no. 6, pp. 839–850, 2005, ISSN: 1359-835X. DOI: 10.1016/j.compositesa.2004.10.026 (cit. on p. 92).

[29] R. D. Mindlin, "Influence of rotary inertia and shear on flexural motion of isotropic, elastic plates", *ASME Journal of Applied Mechanics*, vol. 18, pp. 31–38, 1951 (cit. on p. 92).

[30] E. Reissner, "The effect of transverse shear deformation on the bending of elastic plates", *ASME Journal of Applied Mechanics*, vol. 12, pp. 68–77, 1945 (cit. on p. 92).

Chapter 4

Advanced numerical simulation

As said in Chapter 1 the pressure and the fibre tension, both Lagrange multipliers, are quantities of interest, so it is of importance to be able to compute them correctly. It is also interesting to be able to conduct simulations with a mesh fine enough through the thickness to retrieve the correct 3D behaviour of the stack of plies.

As was said in Chapter 3 the computational cost of the 3D FEM is very high. In order to reduce the cost, and therefore make possible a simulation at the real scale, the PGD framework is considered. However, as the PGD works well on symmetric definite positive problems, the problem needs to be modified as the mixed formulation leads to a saddle-point problem on which the PGD will not work.

Sections 4.3 and 4.4 focuses on the research and the testing of algorithms that are able to modify the system. Section 4.5 compares the different selected algorithms.

Section 4.6 introduces the PGD framework on this specific category of problem.

Section 4.6.3 presents results obtained with the PGD framework to verify the accuracy of the method.

Contents

4.1 Mixed formulation

4.1.1 Formulation

The system to be solved, presented in Equation (2.26), is recalled here:

$$\begin{bmatrix} \underline{\underline{K}}^v & \underline{\underline{K}}^p & \underline{\underline{K}}^t \\ \left(\underline{\underline{K}}^p\right)^T & \underline{\underline{0}} & \underline{\underline{0}} \\ \left(\underline{\underline{K}}^t\right)^T & \underline{\underline{0}} & \underline{\underline{0}} \end{bmatrix} \begin{bmatrix} \underline{\hat{v}} \\ \underline{\hat{p}} \\ \underline{\hat{t}} \end{bmatrix} = \begin{bmatrix} \underline{f} \\ \underline{0} \\ \underline{0} \end{bmatrix}. \tag{4.1}$$

As the incompressibility and the inextensibility are both Lagrange multiplier, they can be concatenated in a single Lagrange multiplier, leading to the system:

$$\begin{bmatrix} \underline{\underline{K}}^v & \underline{\underline{K}}^L \\ \left(\underline{\underline{K}}^L\right)^T & \underline{\underline{0}} \end{bmatrix} \begin{bmatrix} \underline{\hat{v}} \\ \underline{\hat{L}} \end{bmatrix} = \begin{bmatrix} \underline{f} \\ \underline{0} \end{bmatrix}, \tag{4.2}$$

with $\underline{\underline{K}}^L$ and $\underline{\hat{L}}$ the concatenated Lagrange constraint matrix and Lagrange multiplier vector, respectively:

$$\underline{\underline{K}}^L = \begin{bmatrix} \underline{\underline{K}}^P & \underline{\underline{K}}^T \end{bmatrix}, \tag{4.3}$$

and

$$\underline{\hat{L}} = \begin{bmatrix} \underline{\hat{p}} \\ \underline{\hat{t}} \end{bmatrix}. \tag{4.4}$$

System defined in Equation (4.2) is characteristic of a saddle-point problem. As it is non-definite, the choice of solver is restricted. To circumvent this difficulty the system will be modified in order to make it definite positive so as to extend the range of solver available.

4.1.2 Reference problem

A direct solver applied on system (4.5) provides the reference solution to compare the accuracy and effectiveness of the other algorithms. The boundary conditions are imposed through Lagrange multiplier method. The problem of reference will be the compression of a [30°, -30 °] stack of TIF using continuous interpolation functions for the pressure and the fibre tension. Boundary conditions are no-slip conditions on top and bottom sides, and an imposed constant velocity of -1 mm.s^{-1} on the top side. The discretisation is fixed at 10 elements for each dimension and only the first time-step is considered. The geometry is a cube of 5mm, and each layer is 1mm thick. Geometry is presented in Figure 4.1, results are presented in Figure 4.2.

The yellow areas represent the domain where the fibre tension is not defined.

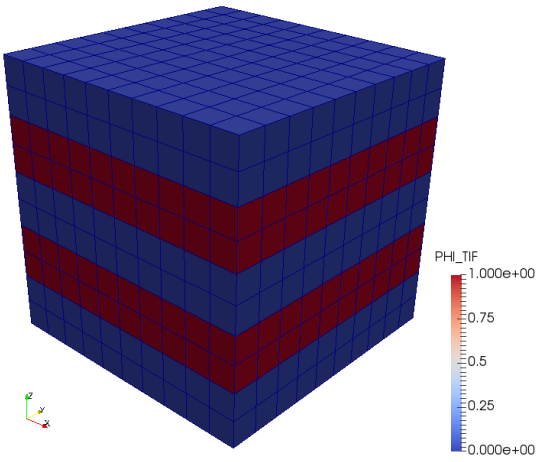

Figure 4.1 – Geometry of the reference problem. TIF layer are represented in red and Stokes layers in blue. Discretisation is fixed at 10 elements in each dimension.

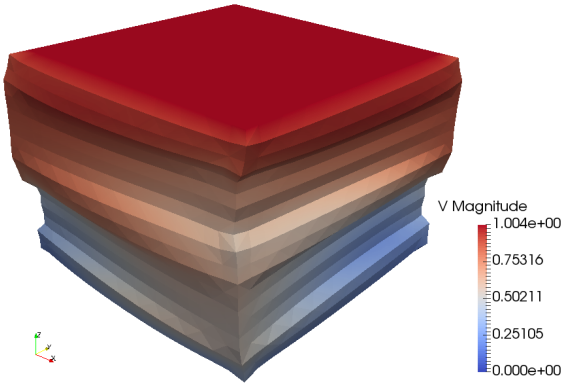

(a) Magnitude of the velocity and warped geometry. Velocity is expressed in $\mathrm{mm.s^{-1}}$.

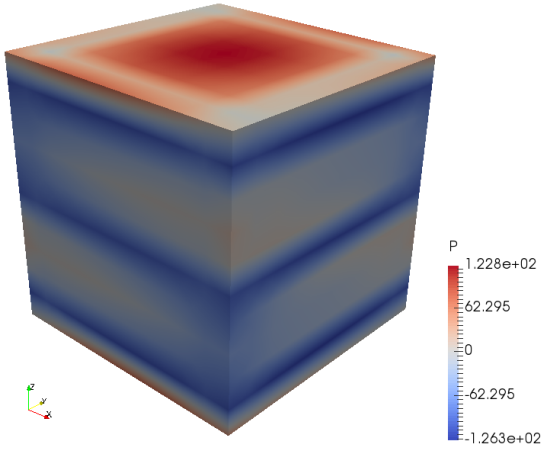

(b) Pressure difference to atmosphere (Pa).

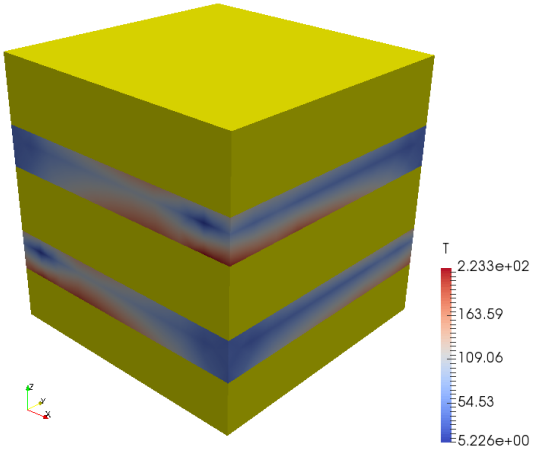

(c) Fibre tension (Pa).

Figure 4.2 – Results of the reference problem using a direct solver on the mixed formulation. Yellow areas represent the domain where the fibre tension is not defined.

4.2 Penalized formulation

The easiest way to modify the system (4.2) to make it positive definite is to penalize the incompressibility and inextensibility constraints, removing them from the system. Therefore only the velocity problem is solved, and the pressure and fibre tension can be obtained by post-treating the velocity field. It has the advantage of changing the system from a saddle-point problem to a definite positive problem on which a choice of direct or iterative solvers can be applied, while reducing the number of unknown by removing the necessity of computing the Lagrange multipliers values.

The drawback of that approach is that the solution depends on the penalization coefficient α which is purely numerical. Higher value of this parameter means the constraint is more precisely verified, but the conditioning of the system is degraded, which can lead to numerical instabilities. Furthermore, the reconstructed fluid pressure and fibre tension fields are unstable and not accurate, making them useless for further analysis.

4.2.1 Formulation

Ó. Brádaigh [15] presents the obtention of the penalized system to compute the velocity taking into account the inextensibility of the fibres. Based on the concatenated system presented in Equation (4.2), the formulation of the penalized system taking into account the incompressibility and the inextensibility is very similar, and leads to the system:

$$\begin{bmatrix} \underline{\underline{K}}^v & \underline{\underline{K}}^L \\ \left(\underline{\underline{K}}^L\right)^T & -\frac{1}{\alpha}\underline{\underline{M}}^L \end{bmatrix} \begin{bmatrix} \underline{\hat{v}} \\ \underline{\hat{L}} \end{bmatrix} = \begin{bmatrix} \underline{f} \\ \underline{0} \end{bmatrix} \qquad \text{as } \alpha \to \infty, \tag{4.5}$$

with $\underline{\underline{M}}^L$ the concatenated mass matrix:

$$\underline{\underline{M}}^L = \begin{bmatrix} \underline{\underline{M}}^P & \underline{\underline{0}} \\ \underline{\underline{0}} & \underline{\underline{M}}^T \end{bmatrix}. \tag{4.6}$$

A different penalization parameter can be used for the pressure and the fibre tension with a slight modification of the system:

$$\begin{bmatrix} \underline{\underline{K}}^v & \underline{\underline{K}}^L \\ \left(\underline{\underline{K}}^L\right)^T & \underline{\underline{M}}^L \end{bmatrix} \begin{bmatrix} \underline{\hat{v}} \\ \underline{\hat{L}} \end{bmatrix} = \begin{bmatrix} \underline{f} \\ \underline{0} \end{bmatrix} \qquad \text{as } \alpha^{\mathrm{P}} \to \infty \text{ and as } \alpha^{\mathrm{T}} \to \infty, \tag{4.7}$$

with α^P the penalization parameter associated with the incompressibility, α^T the penalization parameter associated with the inextensibility and $\underline{\underline{M}}^L$ the concatenated mass matrix:

$$\underline{\underline{M}}^L = \begin{bmatrix} -\frac{1}{\alpha^P}\underline{\underline{M}}^P & \underline{\underline{0}} \\ \underline{\underline{0}} & -\frac{1}{\alpha^T}\underline{\underline{M}}^T \end{bmatrix}. \tag{4.8}$$

For the rest of the section a unique penalization parameter will be used and the the penalized system will be the one in Equation (4.5).

Equation (4.5) leads to the following system of equations:

$$\begin{cases} \underline{\underline{K}}^v \underline{\hat{v}} + \underline{\underline{K}}^L \underline{\hat{L}} = \underline{f}, & \text{(4.9a)} \\ \left(\underline{\underline{K}}^L\right)^T \underline{\hat{v}} - \dfrac{1}{\alpha}\underline{\underline{M}}^L \underline{\hat{L}} = \underline{0}. & \text{(4.9b)} \end{cases}$$

Equation (4.9b) leads to the following expression of the constraint $\underline{\hat{L}}$:

$$\underline{\hat{L}} = \alpha \left(\underline{\underline{M}}^L\right)^{-1} \left(\underline{\underline{K}}^L\right)^T \underline{\hat{v}}, \tag{4.10}$$

that can be injected into Equation (4.9a) to obtain the equation to solve for the velocity:

$$\left[\underline{\underline{K}}^{v} + \alpha \underline{\underline{K}}^{L} \left(\underline{\underline{M}}^{L}\right)^{-1} \left(\underline{\underline{K}}^{L}\right)^{T}\right] \underline{\hat{v}} = \underline{f}. \tag{4.11}$$

As the purpose is to obtain a symmetric definite positive system, boundary conditions are enforced with a penalization method.

4.2.2 Results

Results obtained using a direct solver on the penalized formulation are presented in Figure 4.3. Figure 4.4 presents the plotted values of the solution along a line. As the pressure and the fibre tension are reconstructed from the velocity that is defined everywhere, the fibre tension is also defined everywhere and not only in the TIF layers.

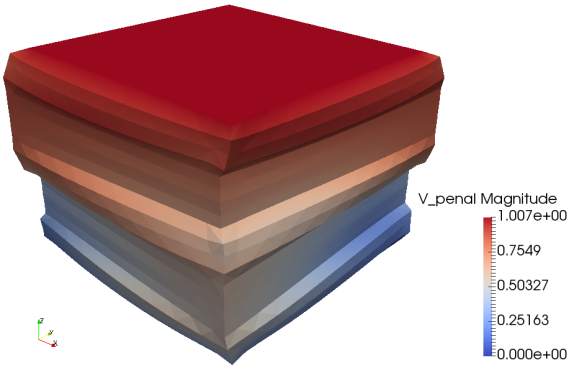

(a) Magnitude of the velocity and warped geometry. Velocity is expressed in $\mathrm{mm.s^{-1}}$.

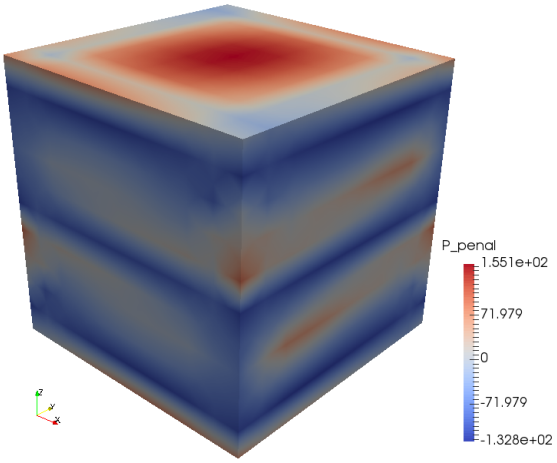

(b) Pressure difference to atmosphere (Pa).

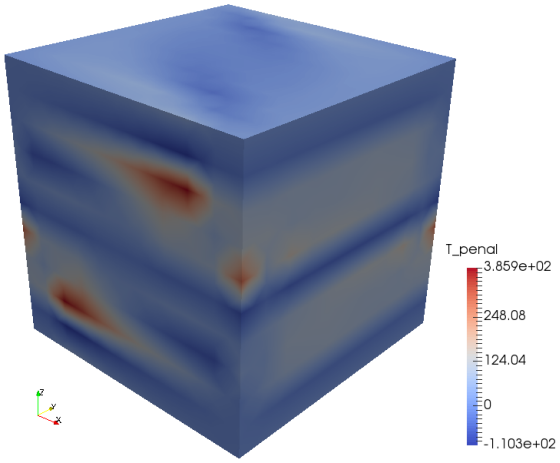

(c) Fibre tension (Pa).

Figure 4.3 – Results of the reference problem using a direct solver on the penalized formulation, with a penalization parameter $\alpha = 10^6$.

As seen in Figure 4.4a the velocity obtained with the penalized formulation is accurate enough. However, Figures 4.4b and 4.4c shows that the pressure and the fibre tension are not accurately reconstructed.

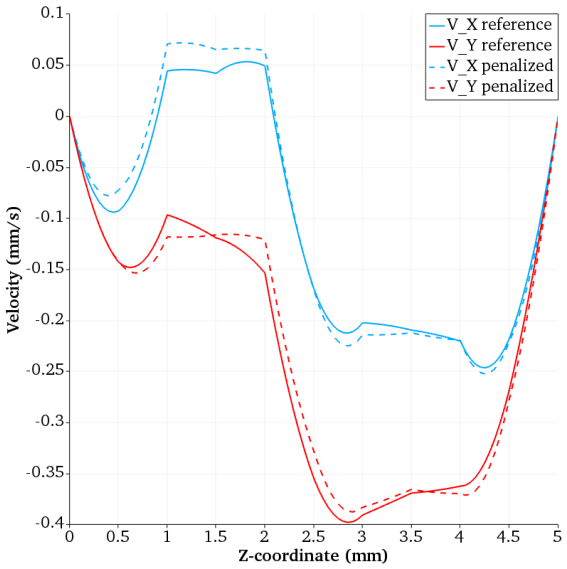

(a) Values of the velocity in $mm.s^{-1}$. Vertical velocity is not represented.

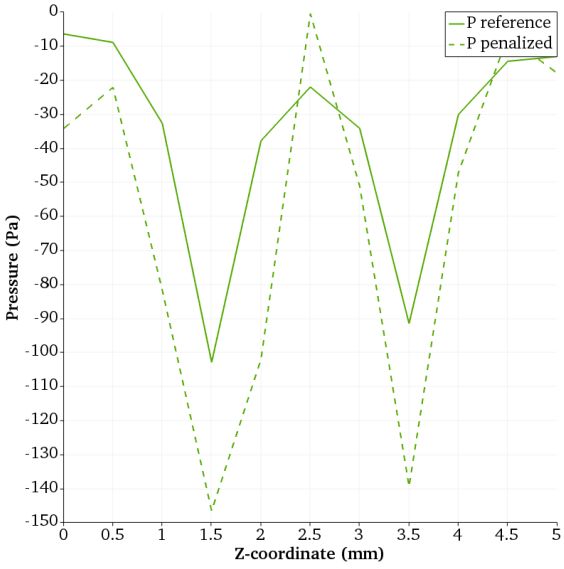

(b) Values of the pressure in MPa.

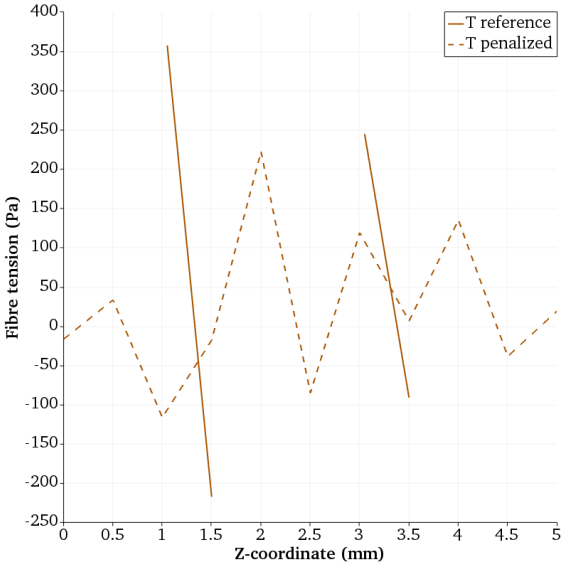

(c) Values of the fibre tension in MPa.

Figure 4.4 – Comparison between the penalized and the mixed formulation solutions. Values are taken along the line (x = 0.5mm, y=0.5mm).

The relative error between the penalized formulation and the reference solution on a given field $\underline{\hat{v}}$ is defined as

$$\varepsilon = \frac{||\underline{\hat{v}}_{ref} - \underline{\hat{v}}_{penal}||}{||\underline{\hat{v}}_{ref}||}. \tag{4.12}$$

If not specified otherwise, the second norm will be used in this work.

Using Equation 4.12 on the solution gives the error shown in Figure 4.5.

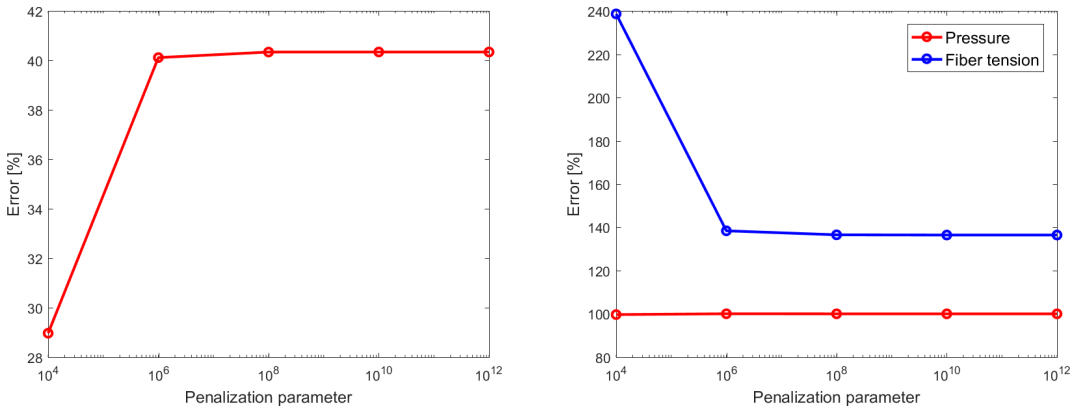

(a) Error on the velocity.

(b) Error on the Lagrange multipliers.

Figure 4.5 – Error on the solution using a direct solver on the penalized formulation. Error is expressed in %.

As seen in Figure 4.5a the error on the velocity decreases when the penalization parameter is greater than $\alpha = 10^6$ then increases as the conditioning of the system deteriorates for a penalization parameter of $\alpha = 10^{16}$. The error value is however acceptable. As seen in Figure 4.5b the error on the Lagrange multipliers is much greater than the error on the velocity. For this reason the penalized formulation is not a reliable solution when the Lagrange multipliers are quantities of interest.

4.3 Augmented Lagrangian

Another way of modifying the saddle-point problem so as to make a definite positive matrix arise is the use of the augmented Lagrangian method. The idea is to take advantage of the fact that $\underline{\underline{K}}^v$ is already symmetric and to use an iterative algorithm designed to solve an equilibrium problem under constraint.

A matrix $\underline{\underline{K}}_r^v$ is introduced as the augmented matrix in order to accelerate convergence:

$$\underline{\underline{K}}_r^v = \underline{\underline{K}}^v + r\underline{\underline{K}}^L \left(\underline{\underline{K}}^L\right)^T, \tag{4.13}$$

with r a numerical parameter. The augmented matrix is very similar to the penalized one, except that the augmentation vanishes at convergence as $\left(\underline{\underline{K}}^L\right)^T \hat{\underline{v}} = \underline{0}$.

Equation (4.13) is injected into Equation (4.2), leading to the augmented system:

$$\begin{cases} \underline{\underline{K}}_r^v \hat{\underline{v}} + \underline{\underline{K}}^L \hat{\underline{L}} = \underline{f}, & \text{(4.14a)} \\ \left(\underline{\underline{K}}^L\right)^T \hat{\underline{v}} = \underline{0}. & \text{(4.14b)} \end{cases}$$

The parameter r must be well chosen to achieve maximal acceleration of the convergence without degrading the conditioning of the system. Fortin [31] has proposed the following optimal value:

$$r_{opt} = \frac{1}{\sqrt{\lambda_{min}\lambda_{max}}}, \tag{4.15}$$

with λ_{min} and λ_{max} the minimum and maximum eigenvalues of $\underline{\underline{K}}^v$, respectively.

4.3.1 Uzawa algorithm

Uzawa algorithm was first presented in [32] and discussed in [33]. The basic concept is to solve the velocity problem without the constraint, then iterate between correcting the Lagrange multiplier and the velocity to take the constraint into account. At convergence the velocity and the Lagrange multiplier are known.

Only the initial algorithm is presented here, more recent work includes inexact and preconditioned Uzawa algorithm [34], fast Uzawa algorithm [35] and non-linear Uzawa algorithm [36].

First an arbitrary value of the Lagrange multiplier $\hat{\underline{L}}^{(0)}$ is guessed. Then, at each iteration, the corresponding velocity field $\hat{\underline{v}}^{(n)}$ is computed and the Lagrange multiplier $\hat{\underline{L}}^{(n)}$ is corrected with the equilibrium residue of the constraint, on which a relaxation parameter is applied to accelerate the convergence or to increase the stability, depending on whether its value is greater or lower than 1. Therefore, Uzawa algorithm is as follow:

Algorithm 1: Uzawa algorithm

begin

Choose $\hat{\underline{L}}^{(0)} \in \mathbb{R}^m$

while $\varepsilon >$ tol **do**

$\hat{\underline{v}}^{(n)} \leftarrow \left(\underline{\underline{K}}_r^v\right)^{-1} \left(\underline{f} - \underline{\underline{K}}^L \hat{\underline{L}}^{(n)}\right)$

$\hat{\underline{L}}^{(n+1)} \leftarrow \hat{\underline{L}}^{(n)} + \rho_n \left(\underline{\underline{K}}^L\right)^T \hat{\underline{v}}^{(n)}$

Compute ε

Fortin [31] has proposed an optimal value of ρ to achieve fastest convergence:

$$\rho_{opt} = \frac{2}{\lambda_{min} + \lambda_{max}}, \tag{4.16}$$

with λ_{min} and λ_{max} the minimum and maximum eigenvalues of $\underline{\underline{K}}^v$, respectively.

In the case where stability of the algorithm becomes a problem, the value of ρ_n can be changed at every iteration to increase the stability without reducing too much the convergence rate.

The stopping criteria ε can be defined in several ways:

- stagnation of the velocity and the Lagrange multiplier: $\varepsilon = \left\| \underline{\hat{v}}^{(n)} - \underline{\hat{v}}^{(n-1)} \right\|_2 + \left\| \underline{\hat{L}}^{(n)} - \underline{\hat{L}}^{(n-1)} \right\|_2$,
- respect of the constraint: $\varepsilon = \left\| \left(\underline{\underline{K}}^L \right)^T \underline{\hat{v}}^{(n)} \right\|_2$,
- stagnation of the velocity and the Lagrange multiplier and respect of the constraint: $\varepsilon = \left\| \underline{\hat{v}}^{(n)} - \underline{\hat{v}}^{(n-1)} \right\|_2 + \left\| \underline{\hat{L}}^{(n)} - \underline{\hat{L}}^{(n-1)} \right\|_2 + \left\| \left(\underline{\underline{K}}^L \right)^T \underline{\hat{v}}^{(n)} \right\|_2$,
- equilibrium residual: $\varepsilon = \left\| \underline{\underline{K}}_r^v \underline{\hat{v}}^{(n)} + \underline{\underline{K}}^L \underline{\hat{L}}^{(n)} + \left(\underline{\underline{K}}^L \right)^T \underline{\hat{v}}^{(n)} - \underline{f} \right\|_2$.

As the matrix $\underline{\underline{K}}_r^v$ solved at each iteration does not change, solving time can be greatly reduced by computing the decomposition of the matrix only once and storing it in memory. Therefore the algorithm necessitates an important number of iterations but each is computed very fast.

4.3.2 Conjugate corrections

The conjugate corrections algorithm share the basic idea of the Uzawa algorithm, the velocity is first computed without constraint and the Lagrange multiplier are corrected with each iteration, but the added correction is orthogonal to the other corrections. It necessitates the solving of a different system at each iteration but converges much faster in terms of number of iterations. At convergence the velocity and the Lagrange multiplier are known. The conjugate corrections algorithm is as follow:

where $(\cdot , \cdot)$ denotes the inner product.

The stopping criterium ε can be defined in the same fashion as in Section 4.3.1.

This algorithm and its convergence are discussed in more details in [37]–[39].

The advantage of this method is that theoretically the convergence is reached in a maximum of m iterations, m being the size of the vector $\underline{\hat{L}}$, although most of the time convergence is reached earlier. In practice though numerical rounding might lead to the loss of orthogonality of the corrections. To circumvent this problem, the base on which $\underline{\hat{L}}$ is expressed can be corrected using the Gram-Schmidt algorithm. Although the use of this algorithm might prevent the conjugate correction algorithm from stalling, it necessitates to store the whole space in memory and is numerically expensive. More information on the practical use of this method can be found in [40].

Algorithm 2: Conjugate corrections algorithm

begin

Choose $\underline{\hat{L}}^{(0)} \in \mathbb{R}^m$

Compute $\underline{\hat{v}}^{(0)} = \left(\underline{\underline{K}}_r^v\right)^{-1} \left(\underline{f} - \left(\underline{\underline{K}}^L\right)^T \underline{\hat{L}}^{(0)}\right)$

Compute $w_0 = -\left(\underline{\underline{K}}^L\right)^T \underline{\hat{v}}^{(0)}$

while $\varepsilon >$ tol **do**

$$\lambda_n = \frac{\left(\left(\underline{\underline{K}}^L\right)^T \underline{\hat{v}}^{(n)}, \left(\underline{\underline{K}}^L\right)^T \underline{\hat{v}}^{(n)}\right)}{\left(\left(\underline{\underline{K}}^L\right)^T \underline{\hat{v}}^{(n-1)}, \left(\underline{\underline{K}}^L\right)^T \underline{\hat{v}}^{(n-1)}\right)}$$

$$\underline{w}_n = -\left(\underline{\underline{K}}^L\right)^T \underline{\hat{v}}^{(n)} + \lambda_n \underline{w}_{n-1}$$

$$\underline{z}_n = \left(\underline{\underline{K}}_r^v\right)^{-1} \underline{\underline{K}}^L \underline{w}_n$$

$$\rho_n = -\frac{\left(\left(\underline{\underline{K}}^L\right)^T \underline{\hat{v}}^{(n)}, \left(\underline{\underline{K}}^L\right)^T \underline{\hat{v}}^{(n)}\right)}{\left(\left(\underline{\underline{K}}^L\right)^T \underline{\hat{v}}^{(n)}, \left(\underline{\underline{K}}^L\right)^T \underline{z}_n\right)}$$

Compute ε

Update $\underline{\hat{L}}^{(n+1)} = \underline{\hat{L}}^{(n)} - \rho_n \underline{z}_n$

Update $\underline{\hat{v}}^{(n+1)} = \underline{\hat{v}}^{(n)} + \rho_n \underline{w}_n$

4.4 Schur complement

The Schur complement is a condensation of the velocity nodes on the Lagrange multipliers nodes. It consists in modifying the system in order to remove the velocity from the unknown, to be able to compute only the Lagrange multipliers. Then the velocity is obtained by solving a last system.

Equation (4.2) gives:

$$\underline{\hat{v}} = \left(\underline{\underline{K}}^v\right)^{-1} \left(\underline{f} - \underline{\underline{K}}^L \underline{\hat{L}}\right). \tag{4.17}$$

Injecting Equation (4.17) into Equation (4.2) gives:

$$\left(\underline{\underline{K}}^L\right)^T \left(\underline{\underline{K}}^v\right)^{-1} \underline{\underline{K}}^L \underline{\hat{L}} = \left(\underline{\underline{K}}^L\right)^T \left(\underline{\underline{K}}^v\right)^{-1} \underline{f}, \tag{4.18}$$

that can be written:

$$\begin{bmatrix} \underline{\underline{K}}^v & \underline{\underline{K}}^L \\ \underline{\underline{0}} & \underline{\underline{S}} \end{bmatrix} \begin{bmatrix} \underline{\hat{v}} \\ \underline{\hat{L}} \end{bmatrix} = \begin{bmatrix} \underline{f} \\ \underline{f}_S \end{bmatrix}, \tag{4.19}$$

with $\underline{\underline{S}}$ the Schur complement such as:

$$\underline{\underline{S}} = \left(\underline{\underline{K}}^L\right)^T \left(\underline{\underline{K}}^v\right)^{-1} \underline{\underline{K}}^L, \tag{4.20}$$

and $\underline{f}_S$ the modified right-hand-side such as:

$$\underline{f}_S = \left(\underline{\underline{K}}^L\right)^T \left(\underline{\underline{K}}^v\right)^{-1} \underline{f}. \tag{4.21}$$

The Lagrange multipliers can be computed by solving Equation (4.18), and then the velocity can be computed using Equation (4.17).

In practice the Schur complement is a full matrix that is very expensive to compute in terms of time and memory usage, but solving it with an iterative solver such as a conjugate gradient makes it possible to avoid the construction of the Schur complement as the only information needed is the result of that operator on a given vector. Using the following conjugate gradient algorithm:
it can be noted that only the $\underline{\underline{S}}\,\underline{p}_n$ product is needed. Using the following algorithm: the

Algorithm 3: Conjugate gradient algorithm

begin
- Choose $\underline{\hat{v}}^{(0)} \in \mathbb{R}^n$
- Compute $\underline{r}_0 = \underline{f}_S - \underline{\underline{S}}\,\underline{\hat{v}}^{(0)}$
- Set $\underline{\hat{L}}^0 = \underline{r}_0$
- **while** $\varepsilon >$ tol **do**
  - $\alpha_n = \frac{(\underline{r}_n, \underline{r}_n)}{(\underline{p}_n, \underline{\underline{S}}\,\underline{p}_n)}$
  - $\underline{\hat{v}}^{(n+1)} = \underline{\hat{v}}^{(n)} + \alpha_n \underline{p}_n$
  - $\underline{r}_{n+1} = \underline{r}_n - \alpha_n \underline{\underline{S}}\,\underline{p}_n$
  - Compute $\varepsilon = \|\underline{r}_{n+1}\|$
  - $\beta_n = \frac{(\underline{r}_{n+1}, \underline{r}_{n+1})}{(\underline{r}_n, \underline{r}_n)}$
  - $\underline{\hat{L}}^{n+1} = \underline{r}_{n+1} + \beta_n \underline{\hat{L}}^n$

Algorithm 4: Compute the Schur complement application on a vector

Input : $\underline{\hat{L}}^n$
Output: $\underline{\underline{S}}\,\underline{\hat{L}}^n$
Compute $\underline{t}_1 = \underline{\underline{K}}^L \underline{\hat{L}}^n$
Solve $\underline{t}_2 = \left(\underline{\underline{K}}^v\right)^{-1} \underline{t}_1$
Compute $\underline{\underline{S}}\,\underline{\hat{L}}^n = \left(\underline{\underline{K}}^L\right)^T \underline{t}_2$

$\underline{\underline{S}}\,\underline{p}_n$ product can be easily computed with a direct solver applied to the system defined in Equation (4.20). This resolution can be accelerated by noting that the system to solve is always the same, and the decomposition can be stored in memory in a similar way as in the conjugate corrections algorithm described in Section 4.3.2.

A GMRES solver was also used on the Schur complement method, a non restarted version and one restarted every 20 iterations. The native Matlab® implementation was used.

4.5 Performance comparison

This section compares the efficiency of the different presented algorithms. Residual, number of iteration and CPU time will be compared. Results for Uzawa algorithm are not presented as the algorithm did not converge.

4.5.1 Residual

The residual against number of iteration for each algorithm is presented in Figure 4.6. Each algorithm is stopped when a residual of $\varepsilon = 10^{-6}$ is reached. The first ten iterations (Figure 4.6a) are separated from the other ones (Figure 4.6b) to improve readibility of the figures.

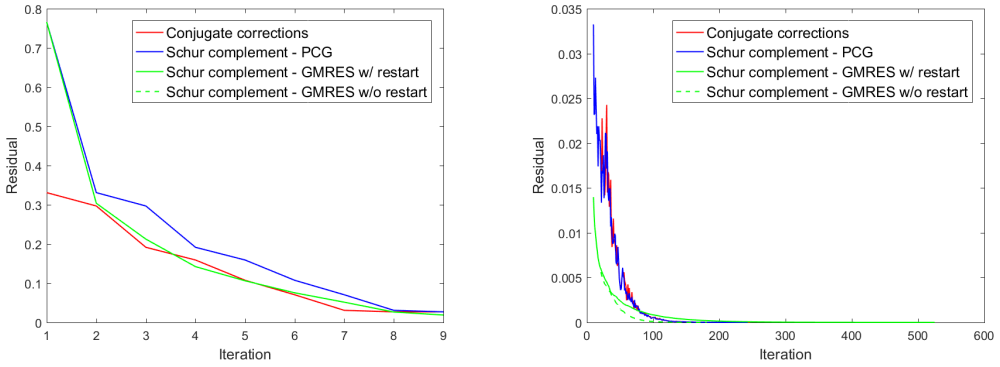

(a) First ten iterations.

(b) Rest of the iterations.

Figure 4.6 – Residual against number of iterations for each algorithm.

The conjugate corrections algorithm and the PCG solver applied to the Schur complement method gives a very similar residual because their principle is the same and they are applied to operators describing the same physical problem. They also do not present a monotonous residual reduction, likely because the problem is highly constrained.

The GMRES solver applied to the Schur complement method has an residual lower than the other algorithms. It is of interest to note that restarting the GMRES solver increases the residual.

4.5.2 Iterations

The necessary number of iteration to reach a given residual for each algorithm is presented in Figure 4.7.

The necessary number of iterations to reach convergence is nearly the same for each algorithm, except for the non restarted GMRES. Therefore the non restarted GMRES will not be the algorithm of choice.

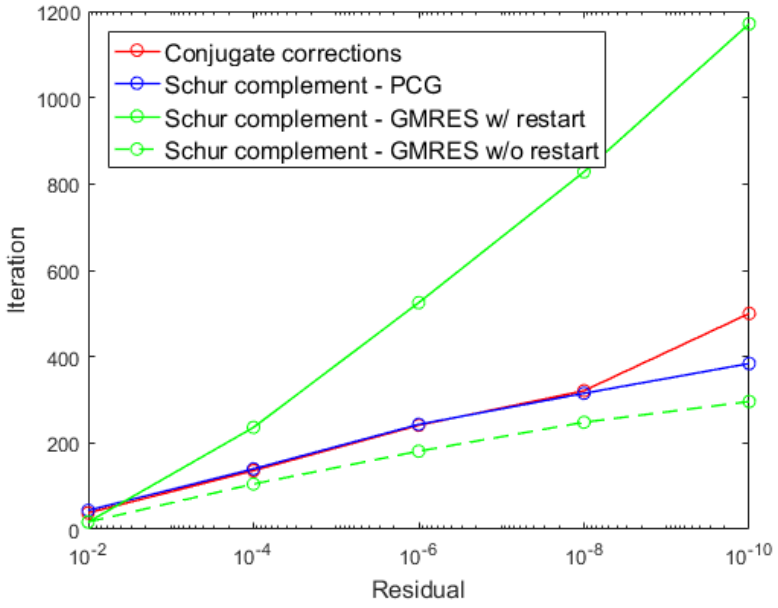

Figure 4.7 – Number of iteration against residual.

4.5.3 CPU time

The CPU time needed to reach a given residual for each algorithm is presented in Figure 4.8. Computed time takes into account the resymmetrisation of the viscous operator, the first factorization and the iterative solving. Those results are obtained using a single core of an AMD FX 8320E @ 3.2 GHz. Reference time using the direct solver is 114s.

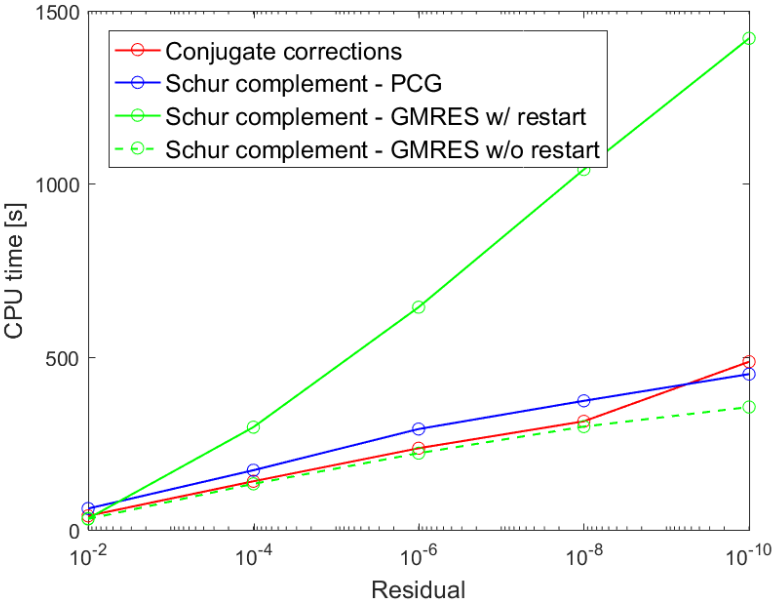

Figure 4.8 – CPU time against residual.

The PCG solver on the Schur complement method and the conjugate corrections algorithm perform very similarly, although the conjugate corrections algorithm seems to start stalling when the residual is lower than $\varepsilon = 10^{-8}$.

The non restarted GMRES solver performs slightly better than the PCG solver. They will therefore be the two solver of choice for the rest of this work.

4.5.4 Results

Results obtained for the velocity and the Lagrange multipliers for each algorithm are presented in Figure 4.9.

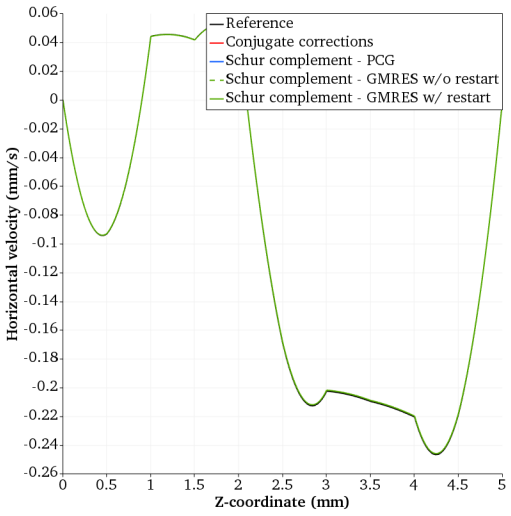

(a) Values of the horizontal velocity in mm.s^{-1}.

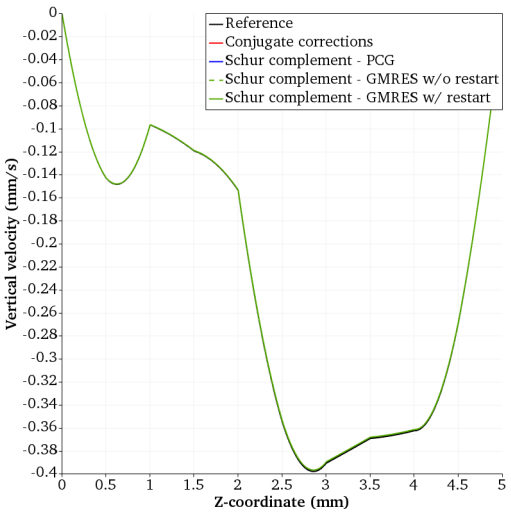

(b) Values of the vertical velocity in mm.s^{-1}.

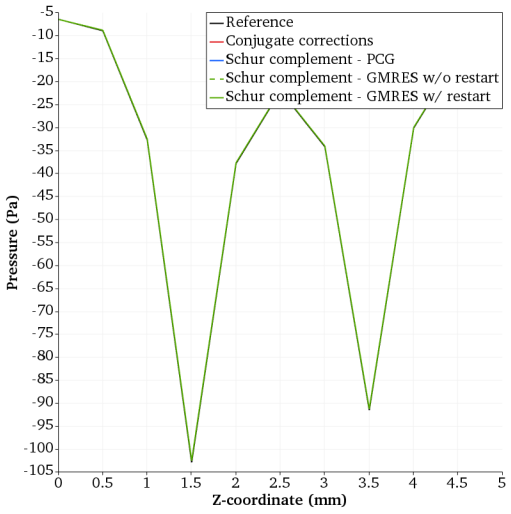

(c) Values of the pressure in Pa.

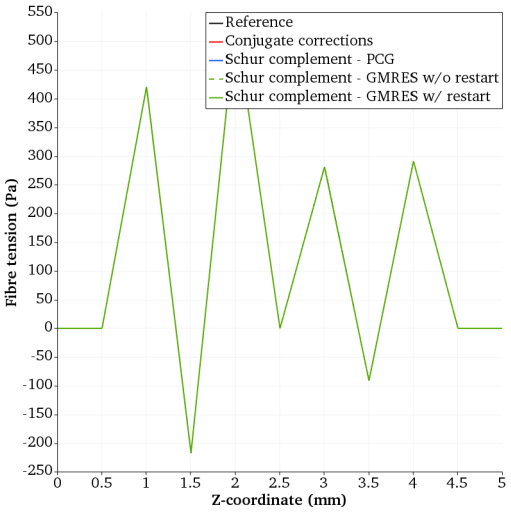

(d) Values of the fibre tension in Pa.

Figure 4.9 – Comparison between the results obtained by applying a direct solver to the mixed formulation and the results obtained by the presented algorithms. Values are taken along the line (x = 0.5mm, y=0.5mm).

As seen in Figures 4.9a, 4.9b, 4.9c and 4.9d the results for the velocity and the Lagrange multipliers are the same regardless of the algorithm used to obtain them, except for the fibre tension in the Stokes layers. This is of no importance since the fibre tension is not defined in the Stokes layer and its value is put to zero.

The error compared to the direct solver applied on the reference problem is presented in Figure 4.10.

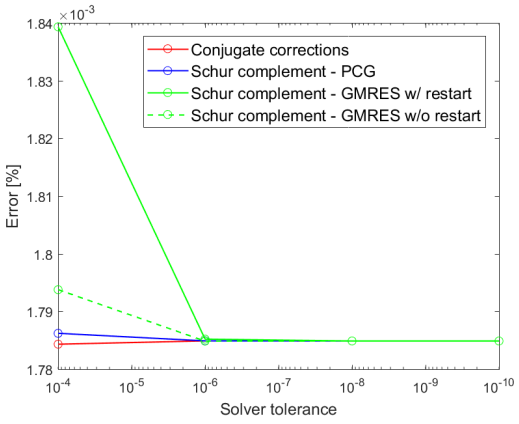

(a) Error on the velocity, expressed in %.

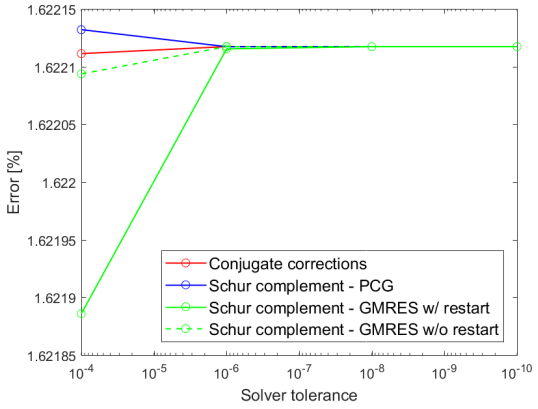

(b) Error on the pressure, expressed in %.

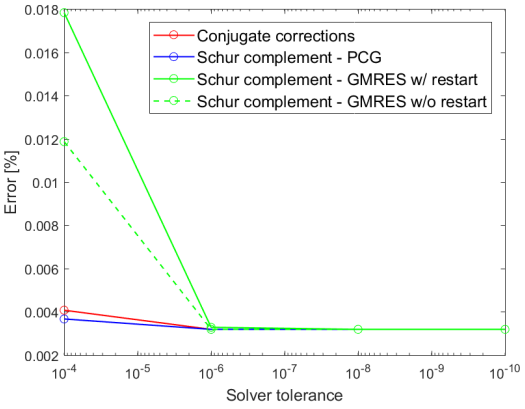

(c) Error on the fibre tension, expressed in %.

Figure 4.10 – Error of the different algorithms compared to the direct solver on the reference problem.

It can be seen in Figures 4.10a and 4.10c that the error on the velocity and the fibre tension decreases with the global residual of the algorithm, whereas Figure 4.10b shows that the pressure does the opposite while staying below a reasonable value.

For these reasons, quality of the results are not a criteria for the choice of the algorithm.

4.6 Proper Generalized Decomposition

Now that algorithms that takes advantage from the symmetric definite positive system were tested, the PGD framework can be used. The principle and the use of the PGD is presented in [41].

The PGD framework is known for its ability to reduce computational cost for a compatible problem. As the separation in this work is the spacial separation of a 3D problem into a 2D/1D set of problems, it will reduce the memory cost and therefore allow to compute 2D/1D problems that were out of the reach of modern desktop computers using a 3D FEM approach.

It was successfully used on an Eriksen fluid, very similar to the TIF model, in [27]. However, a penalized formulation was used. The combined use of the PGD framework with a mixed formulation problem with one constraint was presented in [42].

4.6.1 Chosen separation

The principle of the PGD is to decompose the sought solution under the form of a sum of product of functions of the chosen variables. All the modes are orthogonal, and each mode is the solution of a fixed-point problem.

In the case presented in this work, the chosen decomposition is a spacial decomposition, which allows to decompose the 3D problem in a 2D and a 1D problem. This leads to the variables (x, y) and z, the solution $\underline{\hat{v}}$ is therefore sought under the form:

$$\underline{\hat{v}}(x, y, z) = \sum_{i=1}^{+\infty} \underline{\hat{v}}_i(x, y) \circ \underline{\hat{v}}_i(z) \approx \sum_{i=1}^{N} \underline{\hat{v}}_i(x, y) \circ \underline{\hat{v}}_i(z). \tag{4.22}$$

Using this decomposition, the 3D geometry is decomposed such as:

$$\Omega = \Omega_{xy} \circ \Omega_z. \tag{4.23}$$

Figure 4.11 shows a visual representation of the decomposition of the geometry.

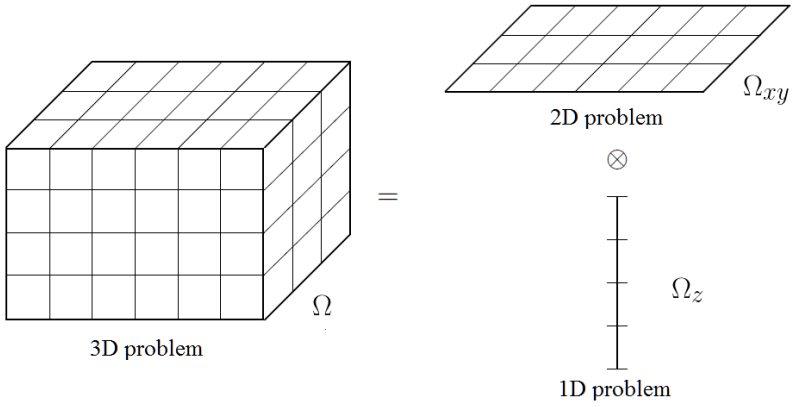

Figure 4.11 – Visual representation of the chosen decomposition.

Using this spatial decomposition, a separated vector is written under the form:

$$\left\{\underline{p}\right\} = \begin{Bmatrix} \underline{p}_{xy}^{m_{xy} \times n} \\ \underline{p}_{z}^{m_z \times n} \end{Bmatrix}, \tag{4.24}$$

with $\underline{p}_{xy}^{m_x \times n}$ and $\underline{p}_{z}^{m_y \times n}$ the (x, y) and z components of the decomposition respectively, $m_x y$ the number of nodes in the (xy) decomposed geometry, m_z the number of nodes in the z decomposed geometry and n the number of modes used to represent the vector.

The decomposition of a vector, such as coordinates, is done using the Singular Value Decomposition method. It can also be done much faster using the Randomized Singular Value Decomposition presented by Halko [43].

The reconstruction of a vector is done using a Hadamard product.

4.6.2 Modified algorithm for computing the Schur complement application

In this section a conjugate gradient solver will be used on the Schur complement formulation, and the PGD will replace the direct solver within the computation of the application of the Schur complement described in Algorithm 4, which will become:
where $\{ \cdot \}$ denotes the decomposed form of a vector using the PGD.

Algorithm 5: Compute the Schur complement application on a vector using the PGD

Input : $\underline{\hat{L}}^n$
Output: $\underline{\underline{S}}\ \underline{\hat{L}}^n$
Compute $\underline{t}_1 = \underline{\underline{K}}^L \underline{\hat{L}}^n$
Decompose $\underline{t}_1$
Solve $\{\underline{t}_2\} = \left(\underline{\underline{K}}^v\right)^{-1} \underline{t}_1$ using the PGD
Recombine $\{\underline{t}_2\}$
Compute $\underline{\underline{S}}\ \underline{\hat{L}}^n = \left(\underline{\underline{K}}^L\right)^T \underline{t}_2$

As described in Algorithm 5 the PGD is only used as a non-linear, separated dimensions solver. The input is separated just before calling the solver and is recombined just after, all the rest of the solving algorithm is conducted using classical Finite Element Analysis. That allows the use of the PGD only where it is known to be efficient. It also avoids the necessity to compute a growing number of modes, keeping the computational cost reasonable.

4.6.3 Results

4.6.3.1 Penalized formulation

To verify that the PGD is able to solve correctly this category of problems, the penalized problem is solved and compared to the penalized solution obtained using the FEM. As the solution is reconstructed in 3D, the Lagrange multipliers will not be reconstructed as the same velocity field will yield the same Lagrange multipliers field. Results are presented in Figures 4.12 and 4.13.

It is seen in Figure 4.13 that the PGD gives different results from the FEM when applied on the penalized formulation. As the PGD is used as an iterative solver, the penalization parameter makes the convergence difficult, and can even stop the solver from converging as the energy added by the penalization can increase the total energy over the convergence criteria of the algorithm.

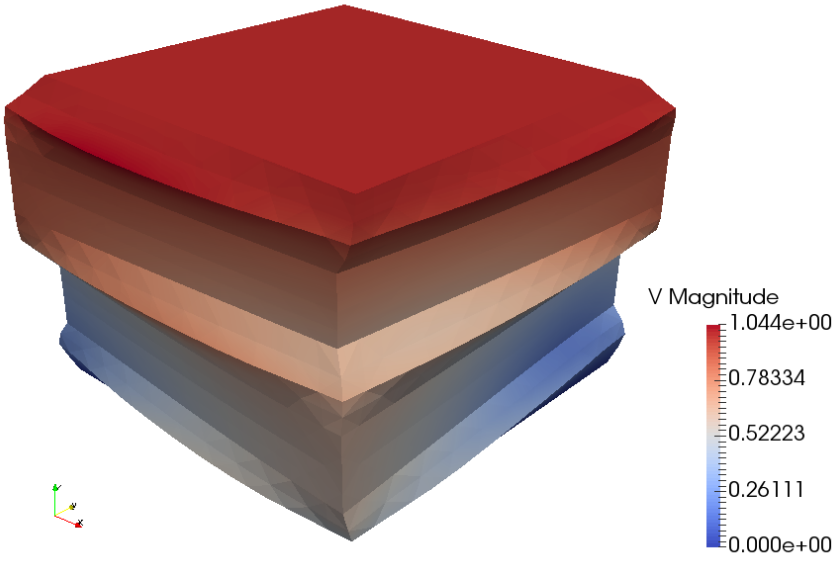

Figure 4.12 – Magnitude of the velocity and warped geometry using the PGD on the penalized formulation. Velocity is expressed in $mm.s^{-1}$

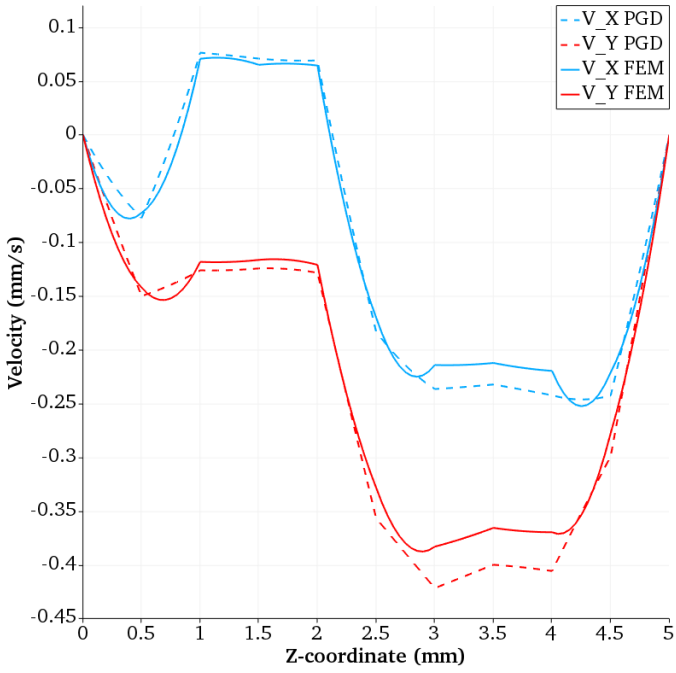

Figure 4.13 – Comparison between the FEM and the PGD approach on the penalized formulation. Values are taken along the line (x = 0.5mm, y=0.5mm). Vertical velocity is not represented.

4.6.3.2 Schur complement formulation

The PGD solver used with a Schur complement formulation was tested, to verify that the velocity and the Lagrange multipliers can be succesfully retrieved, even though the problem is strongly constrained. Only the results obtained with the GMRES solver was used as the Conjugate Gradient solver did not converge. Results are presented in Figure 4.14.

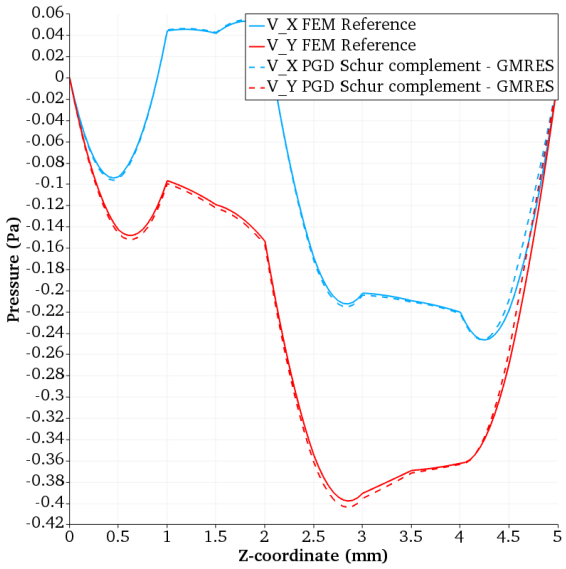

(a) Values of the velocity in $mm.s^{-1}$.

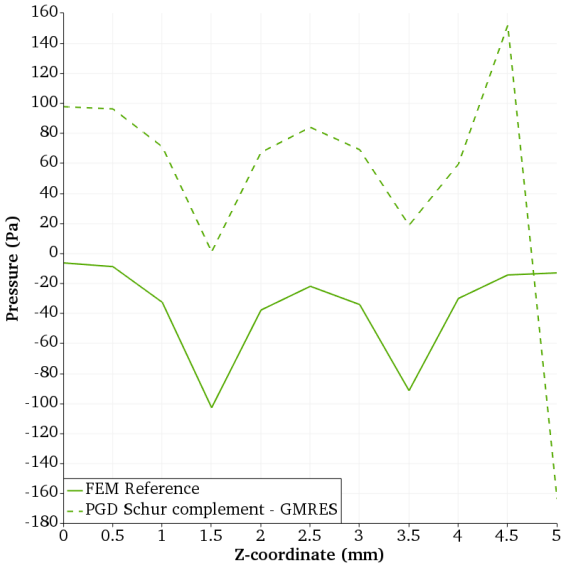

(b) Values of the pressure in Pa.

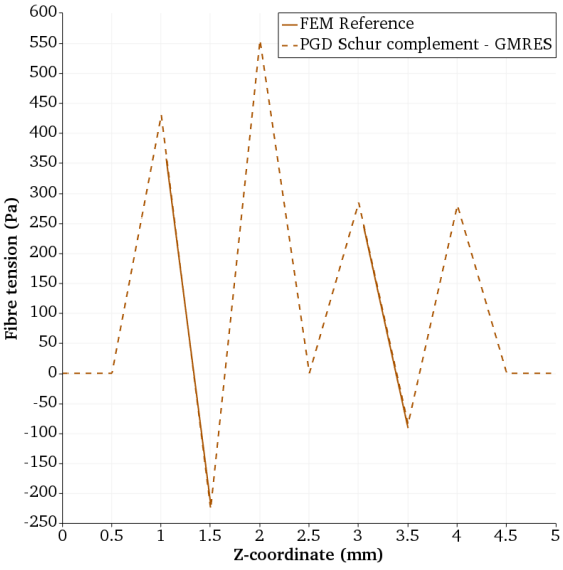

(c) Values of the fibre tension in Pa.

Figure 4.14 – Comparison the results obtained by applying a direct solver to the mixed formulation and the results obtained by a PGD solver coupled with the Schur complement formulation. Values are taken along the line (x = 0.5mm, y=0.5mm).

As can be seen in Figure 4.14 the values are correctly retrieved. The pressure is different as the reference solution is found at a constant. The last value is false because the Lagrange multiplier is computed on a geometry where the velocity is imposed.

In this case also the fibre tension in the Stokes layers is not null (cf. Figure 4.14c), as it is when applying the direct solver to the mixed formulation. This is of not importance since the fibre tension is not defined in the Stokes layer and its values is put to zero.

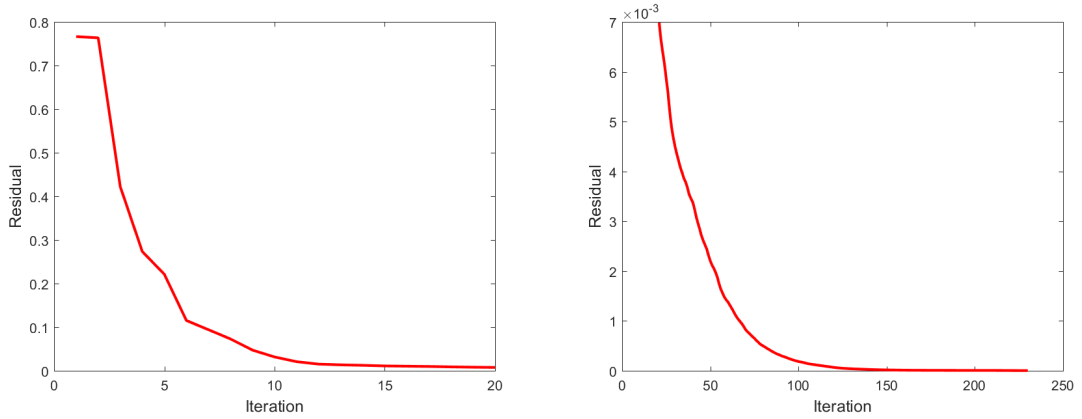

(a) First twenty iterations.

(b) Rest of the iterations.

Figure 4.15 – Residual against number of iterations for the Schur complement formulation within the PGD framework.

Figure 4.15 presents the residual against number of iteration for the Schur complement formulation within the PGD framework. It can be seen that the convergence, although slow, is monotonous.

Total computational time to reach convergence is nearly 35 hours on a single core of an AMD Opteron 6328 @ 3.2 GHz. It can be concluded that the Schur complement used within the PGD framework allows the correct computation of the velocity and the constraints, even with a highly constrained problem, but at a very high cost. For this reason the PGD might not be the solution of choice to reduce the computational cost of the 3D TIF model.

Conclusion

This chapter presented advanced numerical techniques used to reduce the computational cost.

The compression of a [30/-30] stack presented in 3.2.1.3 was chosen as a reference problem, with a fixed discretisation of 10 elements per side. It was shown that the penalisation is not the solution of choice when the fluid pressure and the fibre tension are quantities of interest.

Two methods were therefore presented, the augmented lagrangian and the Schur complement. A classic Uzawa and an orthogonal Uzawa algorithm were applied on the augmented lagrangian method, and a conjugate gradient and two versions of GMRES solver were applied on the Schur complement method. The algorithm/solver couples that converged achieved the same level of accuracy, and the Schur complement/non-restarted GMRES couple was selected for its high convergence speed and low CPU time taken.

The Proper Generalized Decomposition (PGD) framework was then deployed within the non-restarted GMRES solver during the application of the Schur complement step to accelerate computations and reduce the quantity of memory needed. The choice of the step of application was determined by the domain of validity of the PGD solver. The use of

the PGD allowed to reduce the quantity of memory needed while maintaining a very good accuracy, but also caused an increase in CPU time, from 2 minutes when applying a direct solver to the system to 35 hours when applying the PGD within the Schur complement method.

References

[15] C. M. Ó. Brádaigh, "Sheet Forming of Composite Materials", in *Flow and Rheology in Polymer Composites Manufacturing*, Elsevier Science B.V., 1994 (cit. on pp. 37, 114).

[27] C. Ghnatios, E. Abisset-Chavanne, C. Binetruy, F. Chinesta, and S. Advani, "3d modeling of squeeze flow of multiaxial laminates", *Journal of Non-Newtonian Fluid Mechanics*, vol. 234, pp. 188–200, 2016 (cit. on pp. 85, 90, 126).

[31] M. Fortin and R. Glowinski, *Augmented Lagrangian Methods: Applications to the Numerical Solution of Boundary-Value Problems (Studies in Mathematics and its Applications)*. Elsevier Science Ltd, 1983, ISBN: 0444866809 (cit. on pp. 118, 119).

[32] K. Arrow, L. Hurwics, and H. Uzawa, "Programming in linear spaces", in *Studies in linear and nonlinear programming*, K. Arrow, L. Hurwics, and H. Uzawa, Eds., Stanford, California: Stanford University Press, 1958 (cit. on p. 118).

[33] R. Glowinski, J. L. Lions, and R. Trémolières, *Analyse numérique des inéquations variationnelles*, ser. Méthodes mathématiques de l'informatique vol. 1. Dunod, 1976 (cit. on p. 118).

[34] H. C. Elman and G. H. Golub, "Inexact and preconditioned uzawa algorithms for saddle point problems", *SIAM Journal on Numerical Analysis*, vol. 31, no. 6, pp. 1645–1661, Dec. 1994. DOI: 10.1137/0731085 (cit. on p. 118).

[35] Z.-H. Cao, "Fast uzawa algorithm for generalized saddle point problems", *Applied Numerical Mathematics*, vol. 46, no. 2, pp. 157–171, Aug. 2003. DOI: 10.1016/s0168-9274(03)00023-0 (cit. on p. 118).

[36] Y. Lin and Y. Cao, "A new nonlinear uzawa algorithm for generalized saddle point problems", *Applied Mathematics and Computation*, vol. 175, no. 2, pp. 1432–1454, Apr. 2006. DOI: 10.1016/j.amc.2005.08.036 (cit. on p. 118).

[37] E. Polak, *Computational Methods in Optimization: A Unified Approach (Mathematics in Science and Engineering Ser. : Vol 77)*. Academic Press, 1971, ISBN: 0125593503 (cit. on p. 119).

[38] J. W. Daniel, "Convergent step-sizes for gradient-like feasible direction algorithms for constrained optimization", in *Nonlinear Programming*, Elsevier, 1970, pp. 245–274. DOI: 10.1016/b978-0-12-597050-1.50012-9 (cit. on p. 119).

[39] J. Cea and R. Glowinski, "Sur des méthodes d'optimisation par relaxation", *ESAIM: Mathematical Modelling and Numerical Analysis - Modélisation Mathématique et Analyse Numérique*, vol. 7, no. R3, Dunod, Ed., pp. 5–31, 1973 (cit. on p. 119).

[40] L. Pursell and S. Y. Trimble, "Gram-schmidt orthogonalization by gauss elimination", *The American Mathematical Monthly*, vol. 98, no. 6, p. 544, Jun. 1991. DOI: 10.2307/2324877 (cit. on p. 119).

[41] A. Ammar, F. Chinesta, E. Cueto, and M. DoblarÃ©, "Proper generalized decomposition of time-multiscale models", *International Journal for Numerical Methods in Engineering*, vol. 90, no. 5, pp. 569–596, 2012, ISSN: 1097-0207. DOI: 10.1002/nme.3331 (cit. on p. 125).

[42] K. Kergrene, S. Prudhomme, L. Chamoin, and M. Laforest, "Approximation of constrained problems using the PGD method with application to pure neumann problems", *Computer Methods in Applied Mechanics and Engineering*, vol. 317, pp. 507–525, Apr. 2017. DOI: 10.1016/j.cma.2016.12.023 (cit. on p. 126).

[43] N. Halko, P. G. Martinsson, and J. A. Tropp, “Finding structure with randomness: probabilistic algorithms for constructing approximate matrix decompositions”, *SIAM Rev.*, vol. 53, no. 2, pp. 217–288, May 2011, ISSN: 0036-1445. DOI: 10.1137/090771806 (cit. on p. 126).

Conclusion & further work

The forming of a multi-thickness/multi-material blank made of viscous composite patches lead to many complex phenomena, some of them being peculiar to this type of assembly of discontinuous prepregs. The objective of the thesis was to identify them experimentally and propose a realistic numerical model.

Chapter 1 presented experimental characterization of the behaviour of a stack of discontinuous unidirectional prepregs and of a stack of discontinuous woven prepregs when subjected to plane compression, such as can be seen in the phase of consolidation of a stack of plies during forming process. It was shown that discontinuous prepregs rotates, bend and spread when subjected to compression.

The following important conclusions are drawn from the experimental campaign on the unidirectional prepregs:

- There is always a pure resin layer between the plies in prepreg laminates.
- A reaction stress develops in fibres to prevent the flow along their direction.
- There is a complex flow at the plies interface.
- The kinematics of the copper tracers differs from the kinematics of the plies, although the tracers are a good indicator of the movement of the plies.
- The observed phenomena are:
  - Squeeze flow kinematics perpendicular to the fibre direction.
  - Inextensibility in the fibre direction.
  - No bleeding of resin.
  - Rotation and in-plane bending of the plies.

The following important conclusions are drawn from the experimental campaign on the woven prepregs:

- Initial orientation has an influence on the amplitude and the direction of the solid body rotation induced by the flow towards the edges of the sample under compression.
- Specimen size has an influence as larger plies will be subjected to greater viscous forces.
- Structure of the woven fabric has an influence, probably due to the asymmetric flow of polymer in the unbalanced prepreg being the origin of the solid body rotation.

- Fibre fraction has an influence as the excess resin content is responsible for higher displacement of the fibres due to a less constrained fluid.

Chapter 2 presented an existing 2D Transversely Isotropic Fluid model to simulate a stack of unidirectional plies. The existing model was modified to be solved using a mixed formulation to improve the accuracy of the Lagrange multipliers enforcing the incompressibility of the fluid and the inextensibility of fibres. Its stability and accuracy were then tested on the following cases:

- Traction along the fibre direction to verify the ability of the model to respect the inextensibility, even in cases where it was explicitly tried.
- In-plane shearing orthogonal to the fibre direction, where the use of continuous interpolation functions for the pressure and the fibre tension was compared to the use of discontinuous interpolation functions. It was demonstrated that in this case the use of continuous interpolation functions yielded more accurate results.
- Traction with a material discontinuity. It was demonstrated that in this case the use of discontinuous interpolation functions yielded more accurate results, as it could better accomodate the discontinuity.
- Traction with sinusoidal fibres to verify the ability of the model to predict the realignment of the fibres. As the TIF is an homogenized model that considers that the fluid and the fibres cannot be dissociated, the fibres realigned and displaced the fluid with them.
- Discontinuous patch under in-plane shearing, imposed force and imposed solid body motion to verify the numerical stability of the model when subjected to various boundary conditions. As the TIF model is based on a fluid approach, designed to take into account moving bodies, such as unheld discontinuous patches, it was necessary that an unheld discontinuous patch could be simulated without numerical difficulties.
- Traction with randomly oriented fibres to verify the numerical stability. The Quilted Stratum Process (QSP ®), developped by CETIM and its partners, relies on the use of discontinuous patches with different orientations. Thus, the traction on randomly oriented fibres is a necessary step towards an industrial use of the TIF model.
- Pulling of a single layer out of a 0° stack to verify the ability of the model to take into account displacement induced by viscous drag forces.
- 45° tensile tests to verify the possibility of using the TIF model as a numerical testing procedure for obtaining the parameters of the model using a inverse method, and therefore avoiding a costly experimental campaign.

Chapter 3 presented a transformation of the existing TIF model from 2D to 3D. It was first demonstrated, by simulating the compression of a cross-ply stack without resin layer interface, that the TIF model alone is not able to reproduce the experimental observations. A Stokes layer was added and a monolithic model was built from the TIF model in order to take into account the pure resin layer, which existence was experimentally proven. This led to a model that is able to take into account the complex 3D lubrication layer between two composite plies and between a composite ply and the tooling, as was verified on the computation of a cross-ply stack with a resin layer interface which results were compared to

experimental findings. The TIF model was also used to conduct simulations on a stack of woven prepreg. To model the woven ply, two TIF layers were stacked without an interfacial resin layer to introduce the two fibres directions, with a ratio of thickness chosen so as to respect the warp/weft ratio of the woven prepreg. The behaviour of the woven ply was assimilated to the behaviour of the interface between the two TIF layers. Then the stack was modelled with several woven plies, separated with an interfacial resin layer as was done for the stack of unidirectional prepregs. This representation is unable to take into account the direct interaction between the two fibre directions. However, the in-plane shear energy of a dry woven fabric before its locking is very small compared to the energy of the squeeze flow and rotation of viscous prepreg laminate, therefore this assumption is thought to be reasonable.

Computations were compared to experiments:

- On unidirectional prepregs:
  - Cross-ply stack with and without resin layer interface to demonstrate the necessity of the pure reisn layer interface. It also shows the presence of a numerical peak in the fibre tension that is not physical and vanishes with the resin layer interface.
  - $[30, -30]$ stack with resin layer interface to verify that the model is able to retrieve the rotation and the spreading of the composite ply as was seen experimentally.
  - Single ply with thickness variation of the fluid layer to verify that the model is able to compute without numerical instability a moving discontinuous unheld patch. As the thickness of the fluid layer is not homogeneous, when subjected to compression a directional flow takes place and the fluid layer drags the composite ply along due to its viscosity. It was numerically retrieved without the use of a regularization technique.
  - Bending under self-weight of two UD plies. A staircase profile was retrieved as can be expected from the bending of a stack of two inextensible layers.
  - $[30, -30]$ stack with resin layer interface, which size corresponds to a cube extracted from the middle of the specimen used for experimental observations, in order to compare the numerical solution with the experimental measurements. The simulation was conducted on a cube and not on the entire ply for the reason that the Finite Element Method is unable to conduct a simulation of that size at a reasonable cost. It was shown that the TIF model is able to retrieve accurately the experimental measurements, at a fairly good tolerance. The difference can be explained by various reasons:
    * The assumption was made that the pure resin layer represented 6% of the TIF thickness, and that it is of constant thickness. This is not always verified in industrial prepregs, and the thickness might be not constant in the same sample and might change from one sample to another.
    * The resin viscosity was taken from the manufacturer datasheet, and the TIF viscosities calculated using Christensen's semi-empirical model. The actual viscosity can change from one sample to another, and Christensen's model gives accurate results considering the material is homogeneous at the scale of the part, which at the scale of the stack might not be the case.

    * The experimental values are calculated from the displacement of the copper tracers which position in the thickness of the interfacial layer is not perfectly controlled. It is worth to note that they are located in-between the composite layers and not inside them, which could change the results.

- On woven prepregs:
  - $[0, 20, 0]$ stack of unbalanced prepreg with resin layer interface. Measured rotation was 5.6° and computed rotation was 2.303°. While not very precise, the computed value is acceptable given the hypothesis made to model the woven ply with two TIF layers in addition to the considerations made above on the TIF model.
  - $[0, 80, 0]$ stack of unbalanced prepreg with resin layer interface. Measure rotation was -3.14° and computed rotation was -0.926°. Despite the amplitude that is not perfectly predicted, the sign of the rotation is retrieved correctly either the plies are opening or closing.
  - $[0, 20, 0]$ stack of balanced prepreg with resin layer interface. Measure rotation was 0.52° and computed rotation was 7.476°. It can be concluded that the real flow must be actually too complex to be retrieved by the TIF model, and that the interweaving effect must be taken into account for the model to be accurate.

Chapter 4 presented different algorithms that take advantage from the fact that the system to be solved is symmetric definite positive in order to be able to apply the Proper Generalized Decomposition (PGD) framework to accelerate the computations while reducing the memory cost. The mixed formulation was recalled and a reference problem was defined, to then compare the different algorithms in terms of accuracy of the result and in terms of computational efficiency. The penalized formulation was presented, and it was shown that in the case where the Lagrange multipliers are a quantity of interest this formulation does not yield accurate results. The augmented Lagrangian method was presented along with two compatible algorithms, Uzawa's algorithm, although it did not converge, and a conjugate corrections algorithm, similar to the conjugate gradient solver. The Schur complement method was described, and the conjugate gradient and the GMRES solvers were tested. A technique to avoid the explicit construction of the Schur complement and therefore decreasing the computational cost was presented. It appeared that the conjugate gradient and the non-restarted GMRES had very similar performance, whereas the restarted GMRES took longer to converge. Finally the 2D/1D separation of the 3D problem was introduced and the PGD solver was used on the decomposition, within the conjugate gradient and the GMRES solver applied to solve the Schur complement method. It was shown that although the PGD gave accurate results even for the Lagrange multipliers, the CPU time needed to converge was too important to balance the gain of memory usage.

As the computational cost is very important, in terms of memory usage for the FEM or in terms of CPU time for the PGD, further work would be firstly to decrease the computational time. An advanced numerical method was already tried. As the TIF behaviour is mainly in the plane and not in the thickness, a way of decreasing the computational cost would be to reduce the physical model by modelling the TIF layer in 2D, while maintaining the 3D modelling for the Stokes layer which behaviour is entirely 3D.

The TIF model could also be used as an inverse method to identify input parameters for a lighter and faster to solve model. This could provide good parameter values while avoiding the costs and time of an experimental identification campaign. Another use for an inverse method would be to identify the thickness of the Stokes layer to characterize a given prepreg, in order to increase the accuracy of the computations on that specific prepreg when using the TIF model. Such a method would need to rely on simple and yet robust experimental procedures in order to be widely usable.

More comparison with the experimental findings to bring further verifications to the validity of the TIF model is necessary. Moreover, a modification of the TIF model to take into account the interweaving effect of a woven prepreg in order to compute correctly any woven prepreg is of significant importance. This development need to be done in a fluid approach in order to be compatible with the discussed model.

Bibliography

[44] J. S. U. Schell, L. Amory, D. Guillon, F. Chinesta, E. Cueto, and E. Abisset-Chavanne, "Movement of patches during thermoforming: experiment and simulation", in *AIP Conference Proceedings*, AIP Publishing, vol. 1769, 2016, p. 170 032 (cit. on p. 3).

[45] D. Guillon, D. Co, C. Priem, A. Martin, and P. Rozycki, "A biphasic model to predict the compression strength of misaligned thermoplastic composite", in *17th European Conference on Composite Materials - ECCM17*, Munich, Germany, Jun. 2016 (cit. on p. 3).

[46] F. N. Cogswell, *Thermoplastic aromatic polymer composites: a study of the structure, processing and properties of carbon fibre reinforced polyetheretherketone and related materials*. Elsevier, 2013 (cit. on p. 3).

[47] G. B. McGuinness and C. M. Ó. Brádaigh, "Development of rheological models for forming flows and picture-frame shear testing of fabric reinforced thermoplastic sheets", *Journal of Non-Newtonian Fluid Mechanics*, vol. 73, no. 1, pp. 1–28, 1997 (cit. on p. 3).

[1] S. P. McEntee and C. M. Ó. Brádaigh, "Large deformation finite element modelling of single-curvature composite sheet forming with tool contact", *Composites Part A: Applied Science and Manufacturing*, vol. 29, no. 1, pp. 207–213, 1998 (cit. on pp. 3, 32).

[48] R. S. Jones and R. W. Roberts, "Ply re-orientation in compression", *Composites Manufacturing*, vol. 2, no. 3-4, pp. 259–266, 1991 (cit. on pp. 6, 14).

[49] A. B. Wheeler and R. S. Jones, "Numerical simulation of fibre reorientation in the consolidation of a continuous fibre composite material", *Composites Manufacturing*, vol. 6, no. 3-4, pp. 263–268, 1995 (cit. on p. 6).

[50] T.-C. Lim and S. Ramakrishna, "Modelling of composite sheet forming: a review", *Composites Part A: Applied science and manufacturing*, vol. 33, no. 4, pp. 515–537, 2002 (cit. on p. 6).

[51] A. C. Long, *Composites forming technologies*. Elsevier, 2014 (cit. on p. 6).

[52] P. Boisse, *Advances in composites manufacturing and process design*. Woodhead Publishing, 2015 (cit. on p. 6).

[53] O. C. Zienkiewicz and P. N. Godbole, "Flow of plastic and visco-plastic solids with special reference to extrusion and forming processes", *International Journal for Numerical Methods in Engineering*, vol. 8, no. 1, pp. 1–16, 1974 (cit. on p. 6).

[54] E. Onate and O. C. Zienkiewicz, "A viscous shell formulation for the analysis of thin sheet metal forming", *International Journal of Mechanical Sciences*, vol. 25, no. 5, pp. 305–335, 1983 (cit. on p. 6).

[55] O. J. Nixon-Pearson, J. P.-H. Belnoue, D. S. Ivanov, K. D. Potter, and S. R. Hallett, "An experimental investigation of the consolidation behaviour of uncured prepregs under processing conditions", *Journal of Composite Materials*, pp. 1911–1924, 2016. DOI: 10.1177/0021998316665681 (cit. on p. 10).

[2] T. G. Rogers, "Rheological characterization of anisotropic materials", *Composites*, vol. 20, no. 1, pp. 21–27, Jan. 1989, ISSN: 00104361. DOI: 10.1016/0010-4361(89)90677-0 (cit. on pp. 32, 34–36).

[3] A. C. Pipkin and T. G. Rogers, "Plane deformations of incompressible fiber-reinforced materials", *Journal of Applied Mechanics*, vol. 38, no. 3, p. 634, 1971. DOI: 10.1115/1.3408866 (cit. on p. 32).

[4] A. J. M. Spencer, *Deformations of fibre-reinforced materials*, ser. Oxford science research papers. Clarendon Press, 1972 (cit. on p. 32).

[5] C. M. Ó. Brádaigh and R. B. Pipes, "Finite element analysis of composite sheet-forming process", *Composites Manufacturing*, vol. 2, no. 3-4, pp. 161–170, 1991 (cit. on p. 32).

[6] G. B. McGuinness and C. M. Ó. Brádaigh, "Development of rheological models for forming flows and picture-frame shear testing of fabric reinforced thermoplastic sheets", *Journal of Non-Newtonian Fluid Mechanics*, vol. 73, no. 1, pp. 1–28, 1997 (cit. on p. 32).

[7] A. J. M. Spencer, "Theory of fabric-reinforced viscous fluids", *Composites Part A: Applied Science and Manufacturing*, vol. 31, no. 12, pp. 1311–1321, 2000 (cit. on p. 32).

[8] A. J. M. Spencer, "A theory of viscoplasticity for fabric-reinforced composites", *Journal of the Mechanics and Physics of Solids*, vol. 49, no. 11, pp. 2667–2687, 2001 (cit. on p. 32).

[9] A. J. M. Spencer, "Some results in the theory of non-Newtonian transversely isotropic fluids", *Journal of Non-Newtonian Fluid Mechanics*, vol. 119, no. 1-3, pp. 83–90, May 2004, ISSN: 03770257. DOI: 10.1016/j.jnnfm.2002.12.001 (cit. on p. 32).

[10] E. A. D. Lamers, R. Akkerman, and S. Wijskamp, "Fibre orientation modelling for rubber press forming of thermoplastic laminates", *International Journal of Forming Processes*, vol. 6, no. 3-4, pp. 443–463, 2003 (cit. on p. 32).

[11] E. A. D. Lamers, *Shape distortions in fabric reinforced composite products due to processing induced fibre reorientation*. University of Twente, 2004 (cit. on p. 32).

[12] R. H. W. Ten Thije, R. Akkerman, and J. Huétink, "Large deformation simulation of anisotropic material using an updated lagrangian finite element method", *Computer methods in applied mechanics and engineering*, vol. 196, no. 33, pp. 3141–3150, 2007 (cit. on p. 33).

[13] S. P. Haanappel, R. H. W. Ten Thije, U. Sachs, B. Rietman, and R. Akkerman, "Formability analyses of uni-directional and textile reinforced thermoplastics", *Composites Part A: Applied science and manufacturing*, vol. 56, pp. 80–92, 2014 (cit. on p. 33).

[14] E. Gazo Hanna, “Procédé de formage des composites à fibres longues et matrice thermoplastique: analyse expérimentale et numérique du glissement interpli”, PhD thesis, Ecole centrale de Nantes, 2011 (cit. on p. 33).

[15] C. M. Ó. Brádaigh, “Sheet Forming of Composite Materials”, in *Flow and Rheology in Polymer Composites Manufacturing*, Elsevier Science B.V., 1994 (cit. on pp. 37, 114).

[16] T. J. R. Hughes, “Finite element analysis of incompressible viscous flows by the penalty function formulation”, *Journal of Computational Physics*, vol. 30, pp. 1–60, Jul. 1974 (cit. on p. 38).

[17] J. Delmas, *Manuel code_aster - fonctions de forme et points d’intégration des éléments finis, fascicule r03.01.01*, EDF - Code Aster, Sep. 2010 (cit. on p. 38).

[18] A. Fortin and A. Garon, *Les éléments finis : de la théorie à la pratique*, 2011 (cit. on p. 38).

[19] P.-L. George and B. Houman, “Sur les éléments finis quadrilatéraux de degré 1 et 2”, Research Report RR-7909, Mar. 2012, p. 39 (cit. on p. 38).

[20] O. A. Ladyzhenskaya and H. Salkow, *The mathematical theory of viscous incompressible flow*, 2d English ed., rev. and enl. Translated from the Russian by Richard A. Silverman and John Chu. New York : Gordon and Breach, 1969, ISBN: 9780980382914 (cit. on p. 39).

[21] I. Babuška, “The finite element method with lagrangian multipliers”, *Numerische Mathematik*, vol. 20, no. 3, pp. 179–192, 1973, ISSN: 0945-3245. DOI: 10.1007/BF01436561 (cit. on p. 39).

[22] F. Brezzi, “On the existence, uniqueness and approximation of saddle-point problems arising from lagrangian multipliers”, eng, *ESAIM: Mathematical Modelling and Numerical Analysis*, vol. 8, no. R2, pp. 129–151, 1974 (cit. on p. 39).

[23] P. Šimáček, V. N. Kaliakin, and R. B. Pipes, “Pathologies associated with the numerical analysis of hyper-anisotropic materials”, *International Journal for Numerical Methods in Engineering*, vol. 36, no. 20, pp. 3487–3508, 1993, ISSN: 1097-0207. DOI: 10.1002/nme.1620362006 (cit. on p. 39).

[24] J. T. Oden, “Rip-methods for stokesian flows”, The Institute for Computational Engineering and Sciences, The University of Texas at Austin, Research Report 80-11, 1980 (cit. on p. 39).

[25] O. C. Zienkiewicz, R. L. Taylor, and J. Z. Zhu, *The finite element method : its basis and fundamentals*. Amsterdam, Boston, Paris: Elsevier Butterworth-Heinemann, 2005, ISBN: 0-7506-6320-0 (cit. on p. 41).

[26] R. M. Christensen, “Effective viscous flow properties for fiber suspensions under concentrated conditions”, *Journal of Rheology*, vol. 37, no. 1, pp. 103–121, Jan. 1993. DOI: 10.1122/1.550459 (cit. on pp. 41, 100).

[27] C. Ghnatios, E. Abisset-Chavanne, C. Binetruy, F. Chinesta, and S. Advani, “3d modeling of squeeze flow of multiaxial laminates”, *Journal of Non-Newtonian Fluid Mechanics*, vol. 234, pp. 188–200, 2016 (cit. on pp. 85, 90, 126).

[28] W. R. Yu, M. Zampaloni, F. Pourboghrat, K. Chung, and T. J. Kang, "Analysis of flexible bending behavior of woven preform using non-orthogonal constitutive equation", *Composites Part A: Applied Science and Manufacturing*, vol. 36, no. 6, pp. 839–850, 2005, ISSN: 1359-835X. DOI: 10.1016/j.compositesa.2004.10.026 (cit. on p. 92).

[29] R. D. Mindlin, "Influence of rotary inertia and shear on flexural motion of isotropic, elastic plates", *ASME Journal of Applied Mechanics*, vol. 18, pp. 31–38, 1951 (cit. on p. 92).

[30] E. Reissner, "The effect of transverse shear deformation on the bending of elastic plates", *ASME Journal of Applied Mechanics*, vol. 12, pp. 68–77, 1945 (cit. on p. 92).

[31] M. Fortin and R. Glowinski, *Augmented Lagrangian Methods: Applications to the Numerical Solution of Boundary-Value Problems (Studies in Mathematics and its Applications)*. Elsevier Science Ltd, 1983, ISBN: 0444866809 (cit. on pp. 118, 119).

[32] K. Arrow, L. Hurwics, and H. Uzawa, "Programming in linear spaces", in *Studies in linear and nonlinear programming*, K. Arrow, L. Hurwics, and H. Uzawa, Eds., Stanford, California: Stanford University Press, 1958 (cit. on p. 118).

[33] R. Glowinski, J. L. Lions, and R. Trémolières, *Analyse numérique des inéquations variationnelles*, ser. Méthodes mathématiques de l'informatique vol. 1. Dunod, 1976 (cit. on p. 118).

[34] H. C. Elman and G. H. Golub, "Inexact and preconditioned uzawa algorithms for saddle point problems", *SIAM Journal on Numerical Analysis*, vol. 31, no. 6, pp. 1645–1661, Dec. 1994. DOI: 10.1137/0731085 (cit. on p. 118).

[35] Z.-H. Cao, "Fast uzawa algorithm for generalized saddle point problems", *Applied Numerical Mathematics*, vol. 46, no. 2, pp. 157–171, Aug. 2003. DOI: 10.1016/s0168-9274(03)00023-0 (cit. on p. 118).

[36] Y. Lin and Y. Cao, "A new nonlinear uzawa algorithm for generalized saddle point problems", *Applied Mathematics and Computation*, vol. 175, no. 2, pp. 1432–1454, Apr. 2006. DOI: 10.1016/j.amc.2005.08.036 (cit. on p. 118).

[37] E. Polak, *Computational Methods in Optimization: A Unified Approach (Mathematics in Science and Engineering Ser. : Vol 77)*. Academic Press, 1971, ISBN: 0125593503 (cit. on p. 119).

[38] J. W. Daniel, "Convergent step-sizes for gradient-like feasible direction algorithms for constrained optimization", in *Nonlinear Programming*, Elsevier, 1970, pp. 245–274. DOI: 10.1016/b978-0-12-597050-1.50012-9 (cit. on p. 119).

[39] J. Cea and R. Glowinski, "Sur des méthodes d'optimisation par relaxation", *ESAIM: Mathematical Modelling and Numerical Analysis - Modélisation Mathématique et Analyse Numérique*, vol. 7, no. R3, Dunod, Ed., pp. 5–31, 1973 (cit. on p. 119).

[40] L. Pursell and S. Y. Trimble, "Gram-schmidt orthogonalization by gauss elimination", *The American Mathematical Monthly*, vol. 98, no. 6, p. 544, Jun. 1991. DOI: 10.2307/2324877 (cit. on p. 119).

[41] A. Ammar, F. Chinesta, E. Cueto, and M. DoblarÃ©, "Proper generalized decomposition of time-multiscale models", *International Journal for Numerical Methods in Engineering*, vol. 90, no. 5, pp. 569–596, 2012, ISSN: 1097-0207. DOI: 10.1002/nme.3331 (cit. on p. 125).

[42] K. Kergrene, S. Prudhomme, L. Chamoin, and M. Laforest, "Approximation of constrained problems using the PGD method with application to pure neumann problems", *Computer Methods in Applied Mechanics and Engineering*, vol. 317, pp. 507–525, Apr. 2017. DOI: 10.1016/j.cma.2016.12.023 (cit. on p. 126).

[43] N. Halko, P. G. Martinsson, and J. A. Tropp, "Finding structure with randomness: probabilistic algorithms for constructing approximate matrix decompositions", *SIAM Rev.*, vol. 53, no. 2, pp. 217–288, May 2011, ISSN: 0036-1445. DOI: 10.1137/090771806 (cit. on p. 126).

UNIVERSITE BRETAGNE LOIRE

CENTRALE NANTES

Thèse de Doctorat

Grégoire SORBA

Etude expérimentale et modélisation numérique des écoulements de compression dans les composites stratifiés visqueux à plis discontinus

Experimental study and numerical modelling of squeeze flow in laminate viscous discontinuous composites

Résumé

La liberté de conception des composites peut être améliorée par la combinaison de préimprégnés continus et discontinus. Le formage d'un empilement préchauffé constitué de plis discontinus distribués et orientés de manière optimale peut mener à des défauts inacceptables tels que des plissements dans le plan et hors-plan, glissement de plis, rotation de plis adjacents, flexion de fibres induite par un écoulement de compression transverse et finalement une distribution des fibres inappropriée et inefficace. Ces phénomènes naissent de la liberté individuelle de déplacement et de déformation des plis discontinus à l'intérieur du moule pendant la phase de formage. Premièrement ce travail présente des expériences conduites afin d'identifier le comportement sous compression d'un empilement de préimprégnés visqueux discontinus unidirectionnels et tissés. Un modèle basé sur une approche fluide hétérogène visqueux isotrope transverse est ensuite développé en accord avec les observations expérimentales. Il est notamment montré que les différents phénomènes observés sont retrouvés numériquement pour les unidirectionnels et partiellement pour les tissés et que les valeurs prédites sont globalement en bon accord avec les mesures expérimentales. L'obtention de résultats réalistes nécessite une résolution en 3D avec un maillage relativement fin dans l'épaisseur. Finalement des méthodes numériques avancées sont mises en place afin de tenter de réduire le coût des simulations.

Mots clés
Préimprégnés UD, préimprégnés tissés, propriétés rhéologiques, simulation de procédé, écoulement de compression, fluide isotrope transverse (TIF), complément de Schur, décomposition en modes propres généralisée (PGD)

Abstract

The design freedom of composites can be improved by combining continuous and discontinuous prepregs. The forming of a pre-heated blank made of optimally oriented and distributed discontinuous prepreg plies may lead to unacceptable defects such as in-plane and out-of-plane wrinkles, sliding of plies, rotation of adjacent plies, bending of fibres induced by transverse squeeze flow and finally to inappropriate and inefficient fibre distribution. This arises because the individual discontinuous plies are free to move and deform in the mould during the forming step. First, this work presents some experiments conducted to identify the behaviour of a stack of unidirectional and woven discontinuous viscous prepregs subjected to through-thickness compression. Then a model based on a heterogeneous transverse isotropic fluid approach is gradually developped in agreement with the experimental findings. It is shown that the various observed phenomena are retrieved for the unidirectional and partly for the woven prepreg by the numerical model. The predicted values are in good agreement with measurements, when the problem is solved in 3D with a relatively fine mesh in the thickness. Finally an attempt is made to reduce the computational cost by the use of advanced numerical simulation techniques.

Key Words
UD prepreg, woven prepreg, rheological properties, process simulation, squeeze flow, Transversely Isotropic Fluid (TIF), Schur complement, Proper Generalized Decomposition (PGD)